

# The Application of Millimeter Wave Spectroscopy to Ground-Based Remote Sensing of the Atmosphere

by

Niall J Ryan

A thesis submitted in conformity with the requirements  
for the degree of Doctor of Philosophy

Department of Physics  
University of Toronto

© Copyright by Niall J Ryan 2015

# The Application of Millimeter Wave Spectroscopy to Ground-Based Remote Sensing of the Atmosphere

Niall J Ryan

Doctor of Philosophy

Department of Physics  
University of Toronto

2015

## Abstract

A new ground-based millimeter wave radiometer, SPÉIR, was designed as part of an observation system to detect and monitor ozone-related trace gases in the Arctic stratosphere. SPÉIR is designed to operate in the frequency range 265-280 GHz and measure the atmospheric spectra of ozone, nitrous oxide, nitric acid, and chlorine monoxide, from which vertical profiles of the gas concentrations can be retrieved. The observation system was characterised and simulated to determine its capability while operating at its intended location at Eureka, Nunavut (80°N). The altitude ranges and resolution of the retrieved profiles were determined, as well as the most significant sources of error in the profile of each gas. Optimal estimation statistics were compared to inversions of 500 simulated spectra. The results are in good agreement but showed that nonlinearities in the forward model, if not accounted for, can cause errors of 5-10% when constructing climatologies or analyzing trends with the trace gas profiles. A sensitivity study was performed to quantify the effects that uncertainties in the spectral parameters of molecules have on ground-based measurements at 265-280 GHz, and recommendations are made for new laboratory measurements.

An inversion scheme was created to retrieve ozone profiles from measurements made by KIMRA (Kiruna Microwave Radiometer) and MIRA 2 (Millimeter Wave Radiometer 2), two ground-based millimeter wave radiometers in Kiruna, Sweden ( $68^{\circ}\text{N}$ ). The resulting profiles in winter/spring 2012/2013 were compared to each other, and to those from ozonesondes and the satellite instrument Aura MLS (Microwave Limb Sounder). The Kiruna instruments are biased low compared to the ozonesondes and generally agree with MLS. A significant oscillatory bias was found in KIMRA profiles and is attributed to standing wave features in the spectral measurements. Winter-time KIMRA ozone from 2008-2013 was used to investigate the natural variability of ozone above Kiruna. A persistent local minimum at approximately 35 km altitude is observed in winter-time ozone profiles and may be due to an effect of the polar vortex edge.

## Acknowledgments

I am glad to have the opportunity to formally thank my supervisor, Prof. Kaley Walker. I am grateful to have had the opportunity to work in her research group. I wish to say thank you for all of her support over the years, her close cooperative work on projects, her advice and guidance on scientific issues, and her never-ending willingness to help on any matter, all the while maintaining her kind approachability. Aside from the area of science, I have also learned a lot from Prof. Walker in the area of project management and leadership, skills that I am sure will help me in any future career.

I am indebted in one way or another to everybody who has worked in the atmospheric group over the years. From a quick question to an in depth discussion, the breadth of knowledge, and the willingness to share it, of the people in this department is something special. I thank in particular Prof. Walker's and Prof. Kim Strong's research groups. I have learned much about the research of my peers through the weekly meetings and presentations, in the Brewer Seminar series, and on GSU Fridays. Thank you to Felicia Kolonjari, who has listened with patience to me about my research, and always offered some useful insight. Thank you to Prof. Dylan Jones and to Prof. Jennifer Murphy for being on my PhD committee and for their guidance over the course of my work. Thank you to Ana Sousa, Krystyna Biel, Teresa Baptista, and Pierre Savaria for dealing with all of the logistics that accompanied me over the years; you are invaluable to this department.

Thank you to Dr. Richard Wylde of Thomas Keating Ltd. (TK), for his role in the SPÉIR design study. Dr. Wylde's expertise in quasioptical systems has immensely benefitted the design of SPÉIR. Thank you for being part of the long technical discussions, often from halfway across the world, and for showing so much interest in the project. I would also like to thank Stuart Froud at TK for his exceptional work on the technical drawings for SPÉIR, and the Canada Foundation for Innovation and the Ontario Research Fund for funding the instrument design study.

Thank you to Dr. Uwe Raffalski, of the Swedish Institute of Space Physics (IRF), for being the ideal collaborator, for allowing and organising my research stay at IRF, for helping me to understand the microwave instruments and measurements there, for guidance in my work with

the data, and for BBQs, hikes, and Eurovision parties. I hope to have the opportunity to work with you again.

Thank you to the Microwave group at the Institute of Applied Physics in Bern. In particular thank you to Prof. Niklaus Kämpfer, and his students, for allowing me a research stay in his group, and to Dr. Axel Murk for knowing everything there is to know about microwave instrumentation and imparting some of that knowledge onto me, and for providing an expert opinion on the design of SPÉIR on many occasions. Thank you to Mark Whale (now at Chalmers University of Technology), who was a good friend during my time in Bern and helped me with quasioptical design and the naming of SPÉIR.

Thank you to Prof. Patrick Eriksson, Prof. Stefan Bühler, and the ARTS/Qpack team for their work in developing the models, for keeping them open source, and being so available for help to every user. I would also like to thank Profs. Eriksson and Bühler for organising the ARTS Open Workshops. I found them indispensably useful.

Thank you to Dr. Anthony Kerr of NRAO for all the information and help with the SIS mixer and everything ALMA Band 6, and to Jeffrey Hessler at VDI for the useful discussions on millimeter wave components. Thank you to the Environment Canada weather station staff for their work in launching the ozonesondes at Eureka. Thank you to Dr. Rigel Kivi of the Finnish Meteorological Institution for supplying the ozonesonde data, and to the MLS team for supplying the data from the satellite.

For research funding, thank you to the Connaught Research Fund at the University of Toronto, the Natural Sciences and Engineering Research Council of Canada (NSERC), and the NSERC CREATE Training Program in Arctic Atmospheric Science. Thank you to the Centre for Global Change Science at the University of Toronto, for supporting my research stays in Bern and in Kiruna, and to Prof. Kim Strong and the NSERC CREATE Training Program in Arctic Atmospheric Science for supporting a technical meeting with VDI in Virginia and for supporting me in obtaining my PMP certification.

Thank you to Cathal, Catalina, Federico, Ryan, and Phil. I definitely would not be at this point if were not for you. Thanks to the School of Graduate Studies soccer team for five great years, and five titles!

Finally, thank you to my family: my parents, brother, and sister. I have read between lines of all the jokes over the years about me *still* being a student ;), and I know that you have always supported me. I will not forget it. And, as always, thanks to Stue.

# Table of Contents

## Contents

Acknowledgments .....	iv
Table of Contents .....	vii
List of Tables .....	xi
List of Figures .....	xii
Chapter 1 .....	1
1.1 Introduction.....	1
1.2 Thesis outline.....	3
Chapter 2 .....	5
2 Background and methodology .....	5
2.1 Introduction to the stratosphere.....	5
2.1.1 Structure and basic quantities .....	5
2.1.2 Ozone chemistry in the stratosphere .....	7
2.1.3 The polar vortex.....	8
2.1.4 Polar ozone depletion .....	9
2.2 Radiative transfer in the atmosphere.....	10
2.2.1 Rotation spectra of molecules .....	10
2.2.2 Absorption, emission, and transfer of atmospheric radiation .....	11
2.3 Millimeter wave radiometry.....	15
2.3.1 Heterodyne detection .....	15
2.3.2 Sideband separation .....	17
2.3.3 Gaussian beams and quasioptics.....	20

2.3.4	Atmospheric observations.....	23
2.4	Inversion theory.....	26
2.4.1	The ill-posed problem.....	26
2.4.2	Optimal estimation.....	26
2.4.3	Linearity of the observing system .....	29
Chapter 3	.....	31
3	SPÉIR instrument.....	31
3.1	Introduction.....	32
3.2	Front-end .....	34
3.2.1	Ultra-Gaussian horn antenna.....	34
3.2.2	Quasioptical setup and signal propagation .....	36
3.2.3	Calibration loads .....	41
3.2.4	Internal reference beam .....	43
3.3	Back-end.....	45
3.3.1	SIS mixer-preamplifier .....	45
3.3.2	Sideband separation and spectrum analysis .....	46
3.3.3	Cryogenic cooling and cryostat.....	48
3.4	Conclusion .....	51
Chapter 4	.....	53
4	Observation system characterization and simulation experiments .....	53
4.1	Forward and inverse models.....	53
4.2	Instrument and inversion setup .....	54
4.3	Results.....	59
4.3.1	Simulated observations above Eureka .....	59

4.3.2 Detection, and retrieval altitude limits and altitude resolution.....	61
4.3.3 Instrument and model parameter uncertainties .....	65
4.3.4 Repeated simulation statistics (OSSEs) .....	67
4.3.5 Nonlinearity in the inversion.....	70
4.4 Conclusion .....	72
Chapter 5 .....	74
5 The effect of spectroscopic parameters.....	74
5.1 Forward and inversion modelling.....	74
5.2 Spectroscopic parameter setup.....	74
5.3 Instrument and inversion setup .....	76
5.4 Effects on retrieved concentration profiles .....	77
5.4.1 Results .....	77
5.4.2 Discussion of the results.....	83
5.5 Conclusion and recommendations .....	85
Chapter 6 .....	87
6 Ground-based observations of ozone above Kiruna.....	87
6.1 Properties of O <sub>3</sub> Measurements .....	88
6.1.1 Location.....	88
6.1.2 KIMRA instrument.....	88
6.1.3 KIMRA dataset.....	89
6.1.4 MIRA 2 instrument.....	90
6.1.5 MIRA 2 dataset.....	91
6.2 Inversion inputs and characteristics.....	92
6.2.1 Forward and inverse model parameters.....	92

6.2.2	Example fits and properties of the retrieved states .....	93
6.3	Comparison of KIMRA and MIRA 2 .....	95
6.3.1	Coincidence criteria .....	95
6.3.2	Results of KIMRA and MIRA 2 comparison .....	96
6.4	Comparison with ozonesondes and MLS .....	99
6.4.1	Ozonesondes at Sodankylä .....	99
6.4.2	Aura Microwave Limb Sounder .....	100
6.4.3	Coincidence criteria .....	101
6.4.4	Results of comparison with ozonesondes and MLS.....	102
6.5	Daily variability in winter-time ozone above Kiruna .....	111
6.5.1	2012/2013 data .....	112
6.5.2	January to March, 5-year O <sub>3</sub> time series .....	113
6.1	Conclusion .....	118
Chapter 7	.....	120
7	Summary and outlook.....	120
7.1	Summary .....	120
7.2	Outlook.....	122
Bibliography	.....	125

## List of Tables

Table 3.1 Operation modes of the digital correlator using COSPAN firmware.....	47
Table 4.1 The center frequencies of the four 1 GHz bands for the target species, and the retrieved and background interfering species in each band. The frequency resolution in each band is 1 MHz.....	55
Table 5.1 The uncertainties of the spectral lines and parameters identified as having the most significant effects on the retrieval of trace gas concentrations with SPÉIR. The “retrieved gas” column lists is the target gas whose retrieved profile is affected by the “source of uncertainty”. The error, $\sigma$ , is one standard deviation. The errors listed are those which fall within the retrieval altitude range of SPÉIR. Uncertainties with a star denote those which were not listed in the spectral line catalogue, and were estimated from the literature.....	81
Table 6.1 Summary of the KIMRA and MIRA 2 instruments when measuring O3.....	86

## List of Figures

Figure 2.1 Typical vertical structure of the atmospheric temperature in the lowest 100 km of the atmosphere. Based on data from [Fleming et al., 1990]. Figure from [Andrews, 2000] with permission of Cambridge University Press. ....	6
Figure 2.2 Typical block diagram of an instrument for millimeter wave observations of the atmosphere. The RF amplifier (shown in dashed lines) is currently only used in instruments that operate at lower frequencies than SPÉIR. The portion between the antenna and the spectrometer is often referred to as the receiver. Figure is from a lecture series by Thomas Wagner at the Max Planck Institute for Chemistry. ....	16
Figure 2.3 Frequency down-conversion by mixing. Both the upper (USB) and lower sideband (LSB) are down-converted to the intermediate frequency. The slant in the power of the sidebands is used to indicate that the LSB is “flipped” upon down-conversion. Image from Bernard Lazareff at Institut de Radio Astronomie Millimétrique. ....	17
Figure 2.4 Sideband-separating mixer configuration used for Band 6 of the Atacama Large Millimeter Array. Figure adapted from [Kerr et al., 2004].....	18
Figure 2.5 Upper: A Gaussian beam propagating from a horn. Lower: A Gaussian beam being transformed by a focusing lens. Figure from [Goldsmith, 1998] with permission from Wiley.2	21
Figure 2.6 The field distribution of the fundamental Gaussian beam mode in linear units (left), and in logarithmic units (right). The X-axis is the radius expressed in terms of the beam radius, $\omega$ . Figure from [Goldsmith, 1998] with permission from Wiley. ....	22
Figure 3.1 Schematic of the signal propagation through the SPÉIR quasioptics.....	34
Figure 3.2 Left: horn profile showing the profiled section designed to excite the $HE_{12}$ mode and the straight section to bring it into phase with the $HE_{11}$ mode. Right: far field antenna pattern of the horns in SPÉIR. The plots are modified from originals provided by Richard Wylde of Thomas Keating Ltd. ....	35

Figure 3.3 3D CAD drawings showing the elevation, plan, end view, and isometric view of SPÉIR. The calibration system is held beneath the optical bench. The length and width of the optical bench is shown in mm in the isometric view. The beam also is also included, with solid green indicating the $(1/e)$ beamwidth and transparent blue indicating 2.5 times the beamwidth. Refer to Figure 3.1 for a schematic of the plan rotated clockwise by $90^\circ$ . Drawings by Stuart Froud at TK.....	38
Figure 3.4 CAD drawing showing elevation (upper) and plan (lower) with general dimensions and labels for the main elements on the optical bench. Also refer to Figure 3.1 for a schematic of the plan rotated clockwise by $90^\circ$ . Drawings by Stuart Froud at TK. Dimensions are in mm. ....	39
Figure 3.5 CAD drawing showing the parameters of the beam as it propagates through the quasioptical setup of SPÉIR. Drawings by Stuart Froud at TK. Dimensions are in mm. ....	40
Figure 3.6 Left: front view of the periscope design for SPÉIR (Section 3.2.2). Right: rear view. Figures are modified from originals provided by Boris Pavlovic at UofT.....	40
Figure 3.7 Left: 3D CAD drawing of the mechanism for the parabolic mirror, {1} in Figure 3.1, as it moves in and out of the beam. The cross section of 2.5 times the beam radius is shown by the red circle. Middle: cross-sectional view of the mirror, the blackbody targets, and the rotatable grid of the calibration system. The hot target is fixed to the optical bench and the cold target sits in a dewar of liquid nitrogen. Right: CAD drawing showing an end view cross-section of the mirror, calibration targets, and rotatable grid. Drawings by Stuart Froud at TK.....	41
Figure 3.8 Labelled drawing of the ambient conical calibration target. The carbon-loaded polymer absorber is shown in shaded grey. Multiple reflections and absorptions of radiation (orange arrows) give rise to low coherent reflections that are responsible for standing waves between the target and the receiver. Drawings modified from those obtained from TK.....	43

Figure 3.9 Intensity of the internal reference beam used for a balanced measurement with SPÉIR, as a function of the polarizer angle (with respect to the polarization angle of the horn). .... 44

Figure 3.10 Left: An SIS tunnel junction is a diode made of two superconductors separated by a very thin insulator. Right: The electronic density of states for an SIS with a dc bias voltage,  $V_0$ , providing an energy just larger than  $E_{\text{gap}}$ . An electron (quasiparticle) tunnels from left to right, adding to the current through the SIS. Diagram from [Wengler, 1992] © 1992 IEEE. .... 45

Figure 3.11 Upper: 3D CAD drawings of the cryostat setup for SPÉIR showing ordinary, transparent, and cross-sectional views. Lower: rotated close-up of the cross-section. Drawings by Stuart Froud at TK. .... 50

Figure 3.12 CAD drawing showing a cross-section of the cryostat for SPÉIR. Labels indicate the three temperature stages, the components within the 4 K stage, and ribbon/coaxial cable placement. Drawing by Stuart Froud at TK. .... 51

Figure 4.1 Climatological gas concentration profiles for Eureka for  $O_3$ ,  $HNO_3$ ,  $N_2O$ ,  $ClO$ , and  $H_2O$ .  $ClO^*$  represents enhanced  $ClO$  levels that can be observed in polar spring in the presence of PSCs. .... 56

Figure 4.2 Upper: line strengths of the dominant molecular rotation transitions in the frequency range 268 – 280 GHz. Middle: the corresponding emission spectrum simulated above Eureka. A daily temperature profile representative of March, and Eureka VMR climatologies were used in the simulation. The shaded ranges show the 1 GHz frequency bands proposed to be used for atmospheric observations with SPÉIR. Blow-ups of each target line are also shown in the lower panels. .... 61

Figure 4.3 Left: the retrieval altitude and detection altitude ranges for each species including  $ClO^*$  ( $ClO$  when enhanced in polar spring). Right: the altitude resolution of the retrieval of each species derived from the FWHM of the averaging kernels. .... 63

Figure 4.4 The averaging kernels and measurement response (thick blue line) for each target species. The vertical dashed line at 0.8 marks the measurement response cut-off point for retrievable altitudes, as used in this work. The measurement response for an atmosphere with enhanced ClO ( $\text{ClO}^*$ ) is also shown. The degrees of freedom for signal (DOFS) for 0-90 km are listed for each species.....64

Figure 4.5 The error contributions to the retrieval of each target species due to measurement noise and instrument and model uncertainties calculated using the linear optimal estimation method (OEM).  $\text{ClO}^*$  is a scenario for ClO when enhanced in polar spring. Error units are in percentage of the respective a priori.....67

Figure 4.6 A comparison of the OEM characterization and the errors in 500 nonlinear inversions of simulated spectra. The retrieval altitude range, without a polynomial fit to the baseline (see Figure 4.3), for each species is shaded. Red: OEM retrieval error (measurement and smoothing error). Dash/Dot Blue: standard deviation of differences between retrieved and generated true atmospheric states for 500 inversions. Black: mean of differences between retrieved and generated true atmospheric states (bias). Dashed black: optimal bias (zero mean). Note: the spike in the ClO bias at  $\sim$ 13 km is caused by interpolation about a discontinuity in the ClO a priori VMR profile.....69

Figure 4.7 The practical measurement responses ( $w_{pm}$ ) for all retrievable species (target and interfering) in each band, found using linear and nonlinear inversion schemes. The true state for each inversion is larger or smaller than the a priori by a factor of  $(1 \pm c)$ , where  $c = 0.3$ . The theoretical response ( $w_m$ ) and optimal response are also plotted. X/Y given in the title of each plot denotes the response of the retrieval of species X to a change in species Y. Refer to Section 2.4.3 for details.....71

Figure 5.1 Errors in the retrieved profiles of (moving clockwise from top left)  $\text{O}_3$ ,  $\text{HNO}_3$ , ClO, and  $\text{N}_2\text{O}$  from uncertainties in the positions of spectral lines (shown as a percentage of the a priori at each altitude). For clarity, only the nine lines which contribute most to the error are shown in the legend. The lines are listed in the legend in order of largest to smallest error contribution. The format of the legend is: “species” @ “line position” | “uncertainty from

catalogue". The retrieval precision (see Section 2.4.2) is also displayed with its X-axis shown at the top of each plot.....	78
Figure 5.2 The same as Figure 5.1, but for the uncertainties in the line intensity parameter. (Clockwise from top left: O <sub>3</sub> , HNO <sub>3</sub> , ClO, N <sub>2</sub> O) .....	79
Figure 5.3 The same as Figure 5.1, but for the uncertainties in the agam parameter. (Clockwise from top left: O <sub>3</sub> , HNO <sub>3</sub> , ClO, N <sub>2</sub> O) .....	80
Figure 5.4 The same as Figure 5.1, but for the uncertainties in the nair parameter. (Clockwise from top left: O <sub>3</sub> , HNO <sub>3</sub> , ClO, N <sub>2</sub> O) .....	81
Figure 5.5 The same as Figure 5.1, but for the uncertainties in the pshift parameter. (Clockwise from top left: O <sub>3</sub> , HNO <sub>3</sub> , ClO, N <sub>2</sub> O) .....	82
Figure 6.1 Maps showing the location of Kiruna .....	89
Figure 6.2 Example spectra and fits for a KIMRA_O3CO measurement and a MIRA 2 measurement.....	94
Figure 6.3 Left and middle: mean averaging kernels for KIMRA and MIRA 2 O <sub>3</sub> retrieved profiles used for the comparison. The measurement response divided by 2 is also shown as the solid black line. Right: the altitude resolution of the profiles, given by the FWHM of the averaging kernels. The shaded area represents altitudes with a measurement response greater than 0.8.....	94
Figure 6.4 Histogram of the time difference between coincident measurements of KIMRA and MIRA 2 between December 2012 and April 2013.....	95
Figure 6.5 Left: the average of the 177 coincident O <sub>3</sub> profiles for KIMRA and MIRA 2 and the a priori for the inversions. Middle: the mean of the difference (KIMRA – MIRA 2) in coincident profiles (black) with $\pm$ the standard deviation as the error bar. Also shown is the sum of the average KIMRA and MIRA 2 measurement error (dashed blue). Right: the correlation of the coincident pairs at each altitude.....	98

Figure 6.6 Left: same as left plot in Figure 6.5 but with markers showing the altitude separation of the partial columns. Right: scatter plot of the partial columns of coincident KIMRA and MIRA 2 data, including a line of best fit. The correlation for each of the sets of partial columns is also shown.....	98
Figure 6.7 Difference of individual O <sub>3</sub> VMR profiles (KIMRA – MIRA 2, red) showing the persistent oscillatory structure. The mean is also shown in black with ± the standard deviation in dashed black. The sum of the average measurement errors for each instrument is shown in dashed blue.....	99
Figure 6.8 Map showing the location of Sodankylä (67.4° N, 26.6° E) with respect to Kiruna (67.8° N, 20.4° E): ~19 hours by bike. ....	100
Figure 6.9 Upper left: the mean O <sub>3</sub> profiles for 25 coincident KIMRA and smoothed Sodankylä ozonesonde measurements. The mean of the difference (KIMRA - sonde) in the profiles is shown on the right (solid black) with the standard deviation as the error bars. The average measurement error for KIMRA is also plotted (dashed blue). Lower left: a histogram of the time difference between coincident measurements. Upper/Lower right: the same but for MIRA 2 and Sodankylä ozonesondes (14 coincident profiles). .....	103
Figure 6.10 Upper: partial column densities of O <sub>3</sub> from KIMRA and from smoothed Sodankylä ozonesonde measurements, from November 2012 to May 2013. The numbers beside the points show the maximum altitude (in km) of each partial column, determined from the maximum altitude of the ozonesonde measurements. The minimum altitude is 15 km. Lower: scatter plot of the KIMRA columns against the ozonesonde columns. The line of best fit is shown with the accompanying equation and correlation coefficient. The data has not been filtered by position relative to the polar vortex. ....	105
Figure 6.11 The same as Figure 5.9, but for MIRA 2 and Sodankylä ozonesonde measurements. ....	106

Figure 6.12 The sPV value corresponding to the measurement locations of KIMRA (blue cross), MIRA 2 (green cross), and Sodankylä ozonesondes (black dot), at altitudes of 18, 24, and 30 km. Lines of sPV values of $1.2$ and $1.6 \times 10^{-4} \text{ s}^{-1}$ , respectively defining the outer and inner edge of the polar vortex, are also shown.....	106
Figure 6.13 Upper row: the same as for Figure 6.5, but for KIMRA minus MLS. Lower left: histogram of the time difference between coincident measurements. Lower right: map showing the locations of the coincident MLS measurements (magenta circles), Kiruna (yellow triangle), and Sodankylä (cyan triangle).....	108
Figure 6.14 The same as Figure 6.13, but for MIRA 2 minusMLS.....	108
Figure 6.15 Upper: the $\text{O}_3$ partial column densities from KIMRA (blue squares) and MLS (magenta diamonds) measurements plotted against time. Lower: scatter plots of the corresponding coincident data. Lines of best fit and correlation coefficients are shown... .....	109
Figure 6.16 Same as Figure 6.15, but for MIRA 2 (green squares) and MLS (magenta diamonds). .....	110
Figure 6.17 sPV values at 34 km at the location and time of all KIMRA measurements (blue cross), and coincident MLS measurements (magenta square). The same is shown for all MIRA 2 measurements (green cross) and coincident MLS measurements (magenta triangle). .... .....	111
Figure 6.18 Time series of the daily average $\text{O}_3$ profiles for KIMRA (top), MIRA 2 (bottom) measurements. Pressure is plotted on a log scale on the Y-axis. ....	113
Figure 6.19 Retrieved $\text{O}_3$ concentrations above Kiruna from KIMRA, for January to March for the years 2008, 2009, 2010, 2011, and 2013. Pressure is plotted on a log scale on the Y-axis. .....	115
Figure 6.20 Left: monthly averages of daily Kiruna $\text{O}_3$ profiles from KIMRA measurements for January, February, and March by year. A missing year means that there were not enough	

measurements during the month to produce a representative average. Right: mean and standard deviations of the monthly profiles..... 117

# Chapter 1

---

## 1.1 Introduction

Over the last three decades it has become increasingly apparent that the composition of the Earth's atmosphere is sensitive to anthropogenic perturbations and so efforts to understand the underlying physical processes have increased [WMO, 2010; IPCC 2013]. Stratospheric ozone concentrations have declined significantly since about 1980 as a result of increased emissions of chlorofluorocarbons (CFCs). Since the signing of the Montreal Protocol in 1987 and its subsequent amendments to regulate the production of CFCs, ozone is expected to gradually recover. A first signature of ozone recovery was recently detected in the Antarctic [Salby et al., 2011]. The continued and increasing anthropogenic emission of greenhouse gases (GHGs) is one of the major concerns for atmospheric scientists and for the global population in general. GHGs are intimately linked with the radiation budget of the Earth, causing warming close to the surface and cooling higher in the atmosphere. Changes to the climate, and the mechanisms that are causing it, can only be understood through the use of observations of the evolving composition of the atmosphere.

The Arctic is known to represent an “early warning system” for global climate change, as it shows a relatively rapid response to compositional changes in the atmosphere that affect the radiative budget of the planet. The extent and causes of the natural variability of the Arctic stratosphere ( $\sim$ 10-50 km altitude) are still uncertain, as can be seen from recent extreme events such as the unprecedented ozone loss in 2011 [Manney et al., 2011]. Satellite measurements over the Arctic between 1978 and 2000 have shown a total ozone column trend of  $-1.04 \pm 0.39\%$  per year in March [Bodeker et al., 2001]. Ozone depletion in the Arctic has been shown to be mainly caused by halogen catalyzed reactions [Rex et al., 2002], denitrification processes in polar stratospheric clouds (PSCs) [Flentie et al, 2002], and dynamical processes [Randel et al., 2002]. Severe Arctic ozone losses reported for some winters during the 1990s [WMO, 2003] have been shown to be not only the result of increased halogen loading since the introduction of CFCs, but also from a long term change in the climate of the Arctic stratosphere.

The evolution of the volume of PSCs ( $V_{\text{PSC}}$ ) over the last 37 years was shown to have a linear increase that correlates with the column loss of ozone from 1992-2003 [Rex et al., 2004]. While cooling of the stratosphere is qualitatively consistent with the radiative impact of increased levels of GHGs [WMO, 2003], results from chemical transport models predict a broad range of temperature changes for increasing GHG forcing: from a slight increase in temperature to severe cooling. In contrast to the idea that recent ozone losses may be caused by increasing  $V_{\text{PSC}}$  due to GHG emissions, a recent study found no statistically significant increase in  $V_{\text{PSC}}$  over the period 1979-2000 and, using a chemistry climate model, found no significant changes in  $V_{\text{PSC}}$  over the entire 21<sup>st</sup> century [Rieder and Polvani, 2013]. The column ozone loss in the Arctic has exhibited significant year to year variability, even though the total halogen abundances hardly varied [WMO, 2010], and the underlying processes are still unclear. This illustrates the need for continuous observations in the Arctic throughout the expected recovery of ozone during the coming decades. The 2004 International Global Observing Strategy Atmospheric Chemistry Theme Report directly states that “... *the frequency of measurements deep in the Arctic vortex remains low. The situation is unsatisfactory given the highly non-linear sensitivity of Arctic stratospheric ozone to cold winters.* ...” [IGOS, 2004].

Remote sensing, using ground-based and satellite-borne instruments, is the predominant method of observing the middle atmosphere. While satellites can offer near global coverage, ground-based instruments provide datasets with high temporal resolution for a particular location. These ground-based datasets are essential for determining short-term (e.g., day-to-day) and longer-term (e.g., seasonal, yearly) variations in the atmospheric composition as well as for providing validation for satellite data. In addition, with the very likely upcoming gap in profiling satellite instruments, calibration with respect to ground-based instruments is needed in order to combine datasets from current and new satellites. This thesis focuses on ground-based remote sensing using millimeter wave spectroscopy. Millimeter wave spectroscopy offers the advantage of high frequency resolution in measured spectra, and low Doppler broadening in the atmosphere, relative to pressure broadening, so that altitude profiles of the atmospheric composition can be obtained from ground-based observations using pressure broadened spectra. In particular, the highly sensitive receivers employed for these observations have enabled measurement of trace gases with weak spectral lines, such as chlorine

monoxide, ClO, from ground-based instruments [Parrish et al., 1981]. A history and description of millimeter wave remote sensing of the stratosphere can be found in [Parrish, 1994].

The research project presented here has three main goals. The first is to design a state-of-the-art instrument capable of measuring concentration profiles of ozone and related trace gases in the Arctic, year-round and providing the first year-round measurements of ClO in Canada. The second goal is to assess the ability and limitations of designed the observation system operating in a High-Arctic environment, and to identify ways in which to improve the sensitivity of ground-based millimeter wave remote sensing in general. The third goal is to develop new Arctic O<sub>3</sub> datasets using existing ground-based instruments.

## 1.2 Thesis outline

The work in this thesis can be divided into two main sections. The first deals with the design, characterization, and simulation of a new, highly sensitive millimeter wave radiometer, SPÉIR. The instrument is to be housed at the Polar Environment Atmospheric Research Laboratory (PEARL) at Eureka, Nunavut, Canada (80.05°N, 86.42°W) [Fogal et al., 2013]. PEARL is a high-Arctic station housing numerous instruments for characterizing atmospheric composition and dynamics from the ground to about 100 km. The location of PEARL makes it an ideal location for a ground-based instrument to observe the composition of the Arctic atmosphere, particularly during the winter.

SPÉIR is designed to measure ozone (O<sub>3</sub>), nitric acid (HNO<sub>3</sub>), nitrous oxide (N<sub>2</sub>O), and ClO in the atmosphere and provide year-round information on the altitude distribution of each gas. ClO is involved in all of the reaction sequences in which Cl, originally released from species such as CFCs, catalytically destroys ozone in the stratosphere [Solomon, 1999]. HNO<sub>3</sub> is a key constituent in PSCs and plays a role in converting radicals into less reactive forms. N<sub>2</sub>O is a greenhouse gas and is a precursor for nitrogen oxide species that catalytically destroy stratospheric ozone [Crutzen, 1970]. N<sub>2</sub>O has also been identified as a significant threat to the ozone layer of the 21st century [Ravishankara et al., 2009]. Instruments currently installed at PEARL to make trace gas measurements either rely on the Sun to take measurements, which means that they cannot operate in the long period of 24-hour darkness during polar winter, or they observe in spectral regions in which ClO signatures are too weak or nonexistent.

The second part of the thesis focusses on observations of O<sub>3</sub> from the Swedish Institute for Space Physics (IRF), Kiruna (67.8° N, 20.4° E). The measurements are from two ground-based instruments: the Kiruna Microwave Radiometer (KIMRA), and the Millimeter Wave Radiometer (MIRA 2). An inversion scheme was developed to retrieve O<sub>3</sub> concentrations from the measured spectra from each instrument. The retrieved atmospheric O<sub>3</sub> profiles were compared to each other and to O<sub>3</sub> concentrations measured from other instruments in an effort to validate the data. The instruments used for the comparison were ozonesondes launched from Sodankylä, Finland (67.37° N, 26.63° E), and the Microwave Limb Sounder (MLS) aboard NASA's Aura satellite. The measurements from KIMRA were used to retrieve winter-time O<sub>3</sub> profiles from 2008 onwards, and the natural variation of O<sub>3</sub> above Kiruna was assessed for that period of the year.

The layout of the thesis is as follows. Chapter 2 reviews the key aspects of the stratosphere, millimeter wave spectroscopy, design and measurement techniques of microwave radiometry, and inversion theory. The design and operation of SPÉIR is outlined in Chapter 3. The characterization and simulation of SPÉIR is covered in Chapter 4, with some implications for ground-based remote sensing in general. Chapter 5 describes a study performed to determine the sensitivity of ground-based observations, in SPÉIR's frequency range, to uncertainties in the spectral parameters of molecules, and recommendations are made for new laboratory measurements. The inversion and comparison of KIMRA and MIRA 2 O<sub>3</sub> profiles is discussed in Chapter 6, with the analysis of winter-time O<sub>3</sub> above Kiruna. A summary of the thesis is given in Chapter 7.

# Chapter 2

---

## 2 Background and methodology

The aim of this chapter is to provide a background in the science and methodology that follows in Chapters 3-6. Any aspect that is not discussed in this chapter will be explicitly described in the chapter to which it pertains. This is in an effort to maintain a logical flow of information, and to avoid repetition.

### 2.1 Introduction to the stratosphere

#### 2.1.1 Structure and basic quantities

The middle atmosphere is a general term that is used to describe two of the layers of the atmosphere: the stratosphere and the mesosphere. The general structure of the atmosphere below 100 km is pictured in Figure 2.1, showing the three lowermost layers, roughly defined by local minima or maxima in the temperature profile. The stratosphere is defined by an increasing temperature profile with altitude and bounded by the tropopause and the stratopause and contains a little under 10% of the entire atmospheric mass. A notable feature of the stratosphere is that it contains the majority of the ozone in the atmosphere (see Section 2.1.2), referred to as the ozone layer.

To a good approximation, the atmosphere behaves as an ideal gas and obeys the law

$$pV = Nk_bT, \quad (2.1)$$

where  $p$  is the pressure,  $V$  is the volume,  $N$  is the number of molecules,  $k_b$  is Boltzmann's constant, and  $T$  is the temperature. The number density,  $n$ , is defined as the number of molecules

of a gas per unit volume,  $N/V$ . A good measure for the abundance of a trace gas in the atmosphere is the volume mixing ratio (VMR). For trace gases which have number densities much smaller than that of air, the VMR is the ratio of the number density of the trace gas and the total number density of the air:

$$VMR = \frac{n}{n_{air}}. \quad (2.2)$$

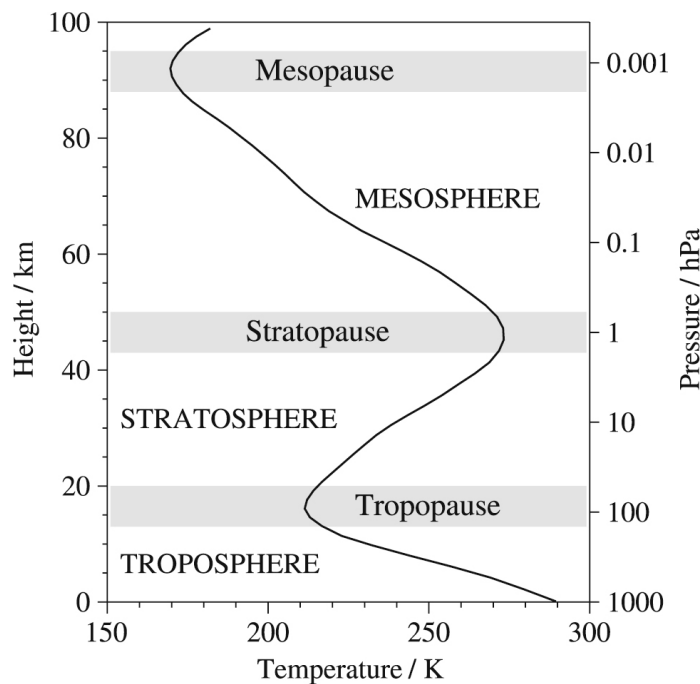


**Figure 2.1** Typical vertical structure of the atmospheric temperature in the lowest 100 km of the atmosphere. Based on data from [Fleming et al., 1990]. Figure from [Andrews, 2000] with permission of Cambridge University Press.

The VMR is a convenient unit as it is conserved following the motion of an air parcel and is changed only by sources or sinks of the gas. In this work, the most frequently used vertical coordinate for the atmosphere is the geometric altitude,  $z$ . The pressure and altitude of the atmosphere can be related through hydrostatic balance. For an atmosphere that is at rest and in static equilibrium, the force of gravity on a parcel of air must equal the difference in pressure forces above and below the parcel. The resulting equation for hydrostatic balance is

$$p = p_0 \exp\left(-\frac{g}{R} \int_0^z \frac{dz'}{T(z')}\right), \quad (2.3)$$

where  $p_0$  is the ground-level pressure,  $R$  is the specific gas constant for air, and  $g$  is the acceleration due to gravity.

### 2.1.2 Ozone chemistry in the stratosphere

The first explanation of the existence of the stratospheric ozone layer was given by Sydney Chapman in 1930 and has accordingly been named the Chapman cycle [Chapman, 1930]. First, oxygen molecules ( $O_2$ ), are split (photolyzed) by ultra-violet radiation with a wavelength smaller than about 240 nm:



The inter-conversion of ozone and molecular oxygen then is then governed by two reactions



where  $M$  is any inert molecule in the atmosphere. Ozone is then lost through the relatively slower reaction



The resulting concentration of  $O_3$  is governed by the production and loss through the reactions above and their respective rates of reaction. The ratio of  $O_3$  to  $O$  is determined by the relatively fast Reactions (2.5) and (2.6), and is found to be very high in the lower and middle stratosphere and so ozone is much more abundant than atomic oxygen there [Jacob, 1999]. The case is reversed in the upper mesosphere. The chemical energy released in Reaction (2.5) is converted into thermal energy in the form of the motion of  $M$ . This has the overall effect of converting the energy from ultra-violet radiation into heat. This and the photolysis of  $O_2$  are the two major sources of heat in the stratosphere.

Considered alone, the Chapman cycle predicts abundances of  $O_3$  in the atmosphere that are higher than observed values. The discrepancy is resolved by considering ozone-destroying catalytic cycles. A common catalytic cycle of reactions take the following form



with the net effect being



The molecule X is a catalyst and can take part in thousands of cycles before being removed. Examples of catalyst molecules include HO, NO, and Cl, and Br, among others [Brasseur and Solomon, 2005]. Inclusion of these reactions brings the observed equilibrium state of  $O_3$  closer to observation but their effects cannot be added linearly as some reactions are not independent of each other. Chemical models used to calculate atmospheric concentrations can include hundreds of reactions.

### 2.1.3 The polar vortex

During winter night at the polar regions, the temperature and pressure drop due to the lack of sunlight. There is a pressure gradient set up that creates a force pointing from equator to pole. A near balance between this pressure force and the Coriolis force, produced by the rotation of the Earth, causes a strong circumpolar westerly wind that acts as a barrier to transport between lower latitudes and the high latitudes. A similar situation arises in the summer due to the 24-hour sunlight being received at the poles. The heating of the lower stratosphere due to the sunlit  $O_3$  causes a pressure gradient in the opposite direction to, and of less magnitude than, that of polar winter. The effect is a circumpolar easterly wind.

In this work, the use of the term polar vortex will be restricted to the winter/spring period. Under conditions where an “automated” vortex definition is robust [Manney et al., 2007], the location of the edge of the vortex has been found to coincide with contours of scaled potential vorticity (sPV), and describes the edge as a bounded region in space. Potential vorticity (PV) is a measure of the angular momentum of air parcels. It is calculated using wind speed and temperature and is conserved for adiabatic frictionless motion. sPV is the potential vorticity scaled by the hemispheric average, and gives a similar range of values at different altitudes. An sPV value of  $1.4 \times 10^{-4} \text{ s}^{-1}$ , or nearby values, have been used extensively in previous works [e.g. Manney et al., 1994, 2007; 2011; Jin et al., 2006] to define the vortex edge centre. The inner- and outer-vortex edges are defined as where the vortex definition function changes curvature

[e.g. Nash et al., 1996], and values of 1.6 and  $1.2 \times 10^{-4} \text{ s}^{-1}$  have been used in the cited works to define the inner and outer edges, respectively. In this work, sPV values are used as a coincidence criterion for the location of an atmospheric measurement with respect to the Arctic polar vortex edge (inside vortex, outside vortex, within the edge), to aid in comparison of measurements from instruments that are not co-located. Two distinct airmasses are identifiable, the vortex air and extra-vortex (or mid-latitude) air. Many properties of the airmasses are very different and steep gradients of atmospheric parameters, temperature and O<sub>3</sub> concentrations for example, can be seen between the two.

### 2.1.4 Polar ozone depletion

Ice particles rarely form in the stratosphere because of the very low water vapour concentrations there. The frost point of water is 185 – 190 K and such temperatures are rarely reached except in Antarctic winter, when PSCs can form. The presence of nitric acid (HNO<sub>3</sub>) in the stratosphere means that solid HNO<sub>3</sub>-H<sub>2</sub>O phases can form at temperatures higher than that of pure water. Nitric acid trihydrate (NAT) can condense at temperatures as high as 197 K, and represents the main form of PSCs. Temperatures within the polar vortex are much lower than outside due to the lack of sunlight and the radiative cooling of the air, making it sufficiently cold to allow the formation of PSCs. The surfaces of the PSCs act as sites for heterogeneous reactions to occur. These heterogeneous reactions are the key component to polar ozone depletion as they convert relatively inactive chemical species (reservoirs) into more labile forms that enter into catalytic cycles with O<sub>3</sub>: Reactions (2.8) and (2.9). Particularly high concentrations of chlorine radicals, ClO<sub>x</sub> (Cl and ClO), are responsible for large losses of O<sub>3</sub> during polar spring. PSC particles provide a surface for the conversion of ClO<sub>x</sub> reservoirs, HCl and ClNO<sub>3</sub>, to Cl<sub>2</sub> which rapidly photolyzes to produce chlorine radicals:



Research indicates that Reaction (2.11) occurs not only on the surface of PSCs but also in aqueous sulphuric acid, H<sub>2</sub>SO<sub>4</sub>, aerosols present in the stratosphere when temperature fall to low values in the polar winter (below 200 K) [Jacob, 1999]. As well as Cl taking the place of X in

Reactions (2.8) and (2.9), the self-reaction of ClO plays a large role in the depletion of O<sub>3</sub> through the following cycle:



The key reaction in this sequence is Reaction (2.14). If the photolysis of the ClO dimer would occur at the weaker O-O bond, instead of the O-Cl bond, this would give a null reaction sequence. Cl also forms another catalytic cycle involving the bromine radical, BrO<sub>x</sub>:



with the same net reaction as before. The two catalytic cycles outlined here lead to most of the polar ozone loss with the ClO self-reaction accounting for about 75% of the total polar loss [McConnell and Jin, 2008].

## 2.2 Radiative transfer in the atmosphere

### 2.2.1 Rotation spectra of molecules

The energy emitted by the atmosphere in the millimeter wave region of the electromagnetic spectrum, is due to the transitions between rotational states of molecules. The energy of a rotational state is derived by solving the time-independent Schrödinger equation for the wavefunction,  $\Psi$ , of the molecule:  $H\Psi = E\Psi$ , where  $H$  is the Hamiltonian operator and  $E$  is the energy level of the state. The energy levels of electronic and vibrational states are generally more widely spaced than those of the rotational states and so, following the Born-Oppenheimer approximation, the rotational eigenvalue (energy,  $E$ ) problem can be solved independently. The rotational Hamiltonian is expressed as [Bernath, 2005],

$$H_{rot} = \frac{P_x^2}{2I_x} + \frac{P_y^2}{2I_y} + \frac{P_z^2}{2I_z}, \quad (2.21)$$

where  $I_x$ ,  $I_y$ , and  $I_z$  are the moments of inertia along the directions of the principal axes of the body, and  $P_x$ ,  $P_y$ , and  $P_z$  are the respective components of the angular momentum operator. For molecules that are symmetric about their principle axis ( $I_x = I_y$ ), the eigenvalues of the rotational Hamiltonian are given by

$$E_{rot} = BJ(J + 1) + (A - B)K^2, \quad (2.22)$$

where  $h$  is Planck's constant,  $A = \frac{h^2}{8\pi^2 I_z}$ , and  $B = \frac{h^2}{8\pi^2 I_x}$ .  $J$  is the total angular momentum quantum number that is a positive integer, and  $K$  is a rotational quantum number,  $-J < K < J$ , that describes the projection of the total angular momentum on the molecular z-axis. The selection rules for allowable transitions between rotational states of these molecules are  $\Delta J = \pm 1$  and  $\Delta K = 0$ . For a diatomic molecule,  $K = 0$  and the solution simplifies to

$$E_{rot} = BJ(J + 1), \quad (2.23)$$

so the energy difference between rotational states for an emission is

$$\nu_{J,J+1} = 2B(J + 1). \quad (2.24)$$

The emissions of the rotational transitions described above are at defined energies and frequencies. Their signatures, known as spectral lines, are quantities of interest in millimeter wave spectroscopy.

### 2.2.2 Absorption, emission, and transfer of atmospheric radiation

#### 2.2.2.1 Radiative transfer equation

When detecting emitted radiation from atmospheric gases, the path of the radiation through the atmosphere must be taken into account, as some fraction of the radiation will be absorbed or scattered by the other molecules or particles in the atmosphere. In the case of millimeter wave radiation, scattering can be neglected and only absorption and emission be considered. The scattering of radiation depends on the frequency and on the properties of the scattering body, and so the errors introduced by neglecting scattering will also vary accordingly. Scattering due to clouds can be neglected up to frequencies of approximately 300 GHz, and by hydro-

meteors up to approximately 100 GHz [Janssen, 1999]. For the frequency range considered in this work (265 – 280 GHz), measurements cannot be performed in rainy or wet conditions.

The absorption of radiation as it travels through the atmosphere can be expressed by Schwarzschild's equation. For a given frequency, the change in the intensity of radiation,  $dI$ , as it travels a distance  $ds$  through a gas is given by

$$dI = (-\alpha I_0 + \alpha B_\nu(T))ds, \quad (2.25)$$

where  $I_0$  is the initial intensity of the radiation,  $B_\nu$  is the Planck function for the radiation emitted from a body at a temperature  $T$ , and  $\alpha$  is the absorption coefficient. The absorption coefficient describes the ability of a body to absorb (and subsequently emit) radiation and is described in Section 2.2.2.2. The first and second terms on the right of Equation (2.25) are the loss and source terms for the radiation, respectively. The basic unit for  $I$  is W/m<sup>2</sup>/sr/Hz. For millimeter wave measurements, a common practice is to express the radiance on a temperature scale: the brightness temperature,  $T_b$ . This is the temperature at which a body would need to be to give a radiance equal to what is measured. In the Rayleigh-Jeans approximation to the Planck function ( $hv \ll k_B T$ ), the intensity of the emission from a blackbody is directly proportional to the temperature of the blackbody. The inverted form gives the brightness temperature:

$$T_b = \frac{c^2}{2\nu^2 k_B} I, \quad (2.26)$$

where  $\nu$  is the frequency, and  $c$  is the speed of light in a vacuum. The brightness temperature is not used as the unit for the calculations in solving the radiative transfer equation (the resulting intensity is usually converted, only), but it is often stated in place of  $I$ . The deviation between the Planck and Rayleigh-Jeans brightness temperatures is less than 8 K at 300 GHz. The solution to the radiative transfer equation in the atmosphere, in brightness temperature units and for a given frequency is

$$T_b = T_{b0} e^{-\tau(z)} + \int_0^z T_b(s) \alpha(s) e^{-\tau(s)} ds, \quad (2.27)$$

where  $s$  is the path length through the atmosphere. The location of the measurement is  $z = 0$  and the light path is integrated from a height  $z$  in the atmosphere. The optical depth,  $\tau$ , is defined as

$$\tau(z) = \int_0^z \alpha(s) ds. \quad (2.28)$$

### 2.2.2.2 The absorption coefficient

The absorption coefficient must be calculated in order to solve Equation (2.27) and involves summing contributions from individual spectral lines and also from non-resonant terms of water vapour, oxygen, nitrogen, and carbon dioxide, known as continua absorption. The atmosphere contains a mixture of gases and the absorption coefficient is calculated by summing over all species and the additional terms,  $C$ , representing the continuum absorptions [Buehler et al., 2005]:

$$\alpha = \sum_{species} \alpha_{species} + \sum_{cont.species} C_{cont.species}. \quad (2.29)$$

The subject of continua is not discussed in depth here but details can be found in several studies [Buehler, 1999; Rosenkranz, 1993; Kuhn, 2003]. The absorption coefficient for a particular molecular species is defined by three quantities:

$$\alpha_{species} = n S_{ij}(T) f(v, v_{ij}), \quad (2.30)$$

where  $n$  is the number density of the species and  $S_{ij}$  is the intensity of a particular rotational transition at a certain temperature. The line shape  $f(v, v_{ij})$  reflects the fact that the emissions from rotational transitions in the atmosphere are not delta functions at the frequency corresponding to the energy gap of the transition,  $v_{ij}$ , but rather broad features. The centre-frequency (position),  $v_{ij}$ , of a spectral line and the line strength,  $S_{ij}$ , are both parameters which are obtained from catalogues of information on spectral lines.

There are two main forms of broadening which account for the lineshape of spectral lines: pressure broadening due to the collision of the emitting molecule with other molecules in the atmosphere, and Doppler broadening due to the motion of molecules at a certain temperature. In the millimeter wave region of the electromagnetic spectrum, a good approximation of line shapes due to pressure broadening is given by the Van Vleck-Weisskopf profile [Van Vleck and Weisskopf, 1945]:

$$f_{vw}(v, v_{ij}) = \left(\frac{v}{v_{ij}}\right)^2 \frac{\gamma_L}{\pi} \left[ \frac{1}{(v - v_{ij} - \delta v_{ij})^2 + \gamma_L^2} + \frac{1}{(v + v_{ij} - \delta v_{ij})^2 + \gamma_L^2} \right], \quad (2.31)$$

where  $\delta v_{ij}$  is the shift in the position of the line centre due to pressure (pshift).  $\gamma_L$  is the Lorentz half-width at half-maximum (HWHM) given by

$$\gamma_L(p, p_s) = \mathbf{agam}(p - p_s) \left(\frac{T_0}{T}\right)^{\mathbf{nair}} + \mathbf{sgam}(p_s) \left(\frac{T_0}{T}\right)^{\mathbf{nself}}, \quad (2.32)$$

where  $p$  is the pressure of the air sample,  $p_s$  is the partial pressure of the species in question,  $T_0$  is a known reference temperature, agam and nair are the air-broadening parameter and its temperature dependence, respectively, and sgam and nself are the self-broadening parameter and its temperature dependence. All of the parameters besides temperature and pressure are found in spectral parameter catalogues. The right-hand side of Equation (2.32) is split into two parts: broadening caused by foreign, or air, molecules (left), and self-broadening caused by the partial pressure of the trace gas (right).

Doppler broadening is caused by the relative translational motion of the emitting molecules. The result is a Doppler shift in the frequency of the emitted radiation. Doppler broadening of lines is described by, [Janssen, 1993],

$$f_D(v, v_{ij}) = \pi^{-1/2} \beta_D^{-1} e^{-\left(\frac{v-v_{ij}}{\beta_D}\right)^2}. \quad (2.33)$$

The Doppler broadening parameter  $\beta_D$  is

$$\beta_D = \sqrt{\frac{2k_B T}{mc^2} v_{ij}}, \quad (2.34)$$

where  $m$  is the mass of the molecule. The Doppler HWHM,  $\gamma_D$ , is given by

$$\gamma_D = \sqrt{2\ln 2}\beta_D. \quad (2.35)$$

Pressure broadening generally dominates in the stratosphere and lower atmosphere. In the mid- to upper-mesosphere the Doppler broadening begins to dominate. To avoid having to switch lineshapes, and to cover the region where broadening effects are of the same order, the best option is to use a convolution of both of these lineshapes.

## 2.3 Millimeter wave radiometry

The aim in using a millimeter wave radiometer is to detect emissions of radiation from molecules in the atmosphere, and to decompose that radiation to give the intensity (Equation (2.27)) as a function of frequency: the spectrum. This spectrum is then used to infer the concentrations of the emitting gases in the atmosphere (Section 2.4). Radiometers are usually specific to a particular spectral range as the components of an instrument are limited by the frequency ranges of their operation.

### 2.3.1 Heterodyne detection

Because the absolute power of millimeter wave radiation from the atmosphere is low, the signal must be amplified before it can be used to generate a spectrum. The basic make-up of a radiometer is given in Figure 2.2. Low frequency signals can be amplified more efficiently than higher frequency signals, so the atmospheric signal (commonly referred to as the Radio Frequency signal, or RF signal) is down-converted to a lower frequency using a technique called heterodyning. In this technique, the RF signal is combined with another signal, generated by a local oscillator (LO), to produce an output signal that is at a much lower, “intermediate”, frequency (IF) and is directly proportional to the RF signal.

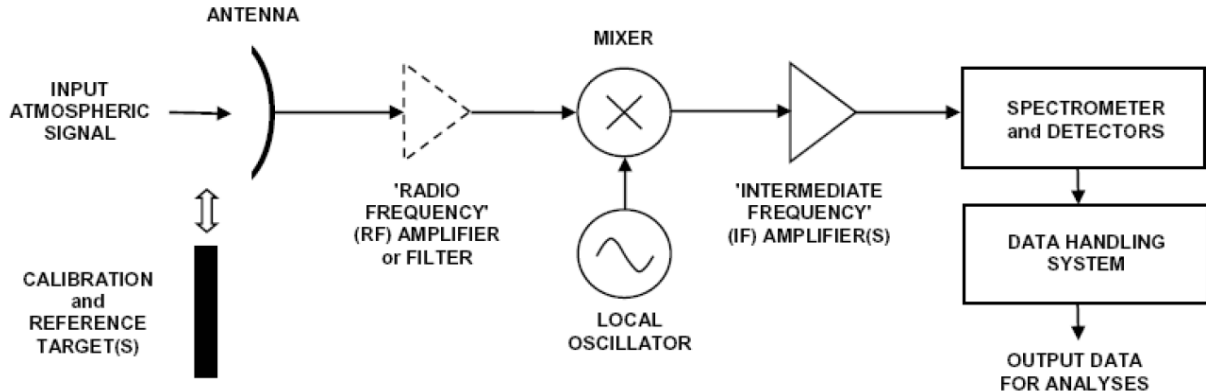


**Figure 2.2** Typical block diagram of an instrument for millimeter wave observations of the atmosphere. The RF amplifier (shown in dashed lines) is currently only used in instruments that operate at lower frequencies than SPÉIR. The portion between the antenna and the spectrometer is often referred to as the receiver. Figure is from a lecture series by Thomas Wagner at the Max Planck Institute for Chemistry.

The RF, LO, and IF are related through

$$IF = |RF \pm LO|. \quad (2.36)$$

So to produce a signal at a desired IF, the LO is tuned to be a fixed distance, in frequency, from the RF. One can see from Equation (2.36) that a consequence of heterodyning is that an additional high frequency signal is also down-converted to the same IF as the frequency of the desired signal. The frequency of this other signal is the mirror image, about the LO frequency, of the desired signal. Figure 2.3 illustrates this pictorially. The signal at a frequency lower than the LO is called the lower sideband (LSB), and the signal at a higher frequency than the LO is called the upper sideband (USB).

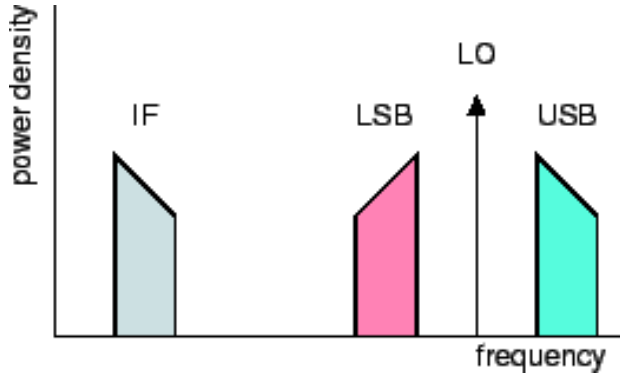


**Figure 2.3** Frequency down-conversion by mixing. Both the upper (USB) and lower sideband (LSB) are down-converted to the intermediate frequency. The slant in the power of the sidebands is used to indicate that the LSB is “flipped” upon down-conversion. Image from Bernard Lazareff at Institut de Radio Astronomie Millimétrique.

The component at which the RF and LO are combined is called the mixer. It is a device that is used to multiply two input signals. In order to be able to multiply together the RF and LO signals, the mixer must be a component that has a nonlinear response to the input. This element is typically a diode that operates in its  $I = V^2$  range, where  $I$  and  $V$  are the current and voltage, respectively. The sensitivity of the mixer and amplifier is quite important as any noise generated internally by those components will also be amplified (see Figure 2.2). The mixers and amplifiers are often cooled to temperatures lower than ambient to reduce the random thermally generated noise in each. After amplification, the IF signal is digitized and analyzed by a spectrometer to produce a spectrum. In practical systems, the IF signal is often filtered and down-converted again to a secondary IF frequency before being digitized.

### 2.3.2 Sideband separation

It is often the case, for a millimeter wave measurement, that it is desirable to remove the unwanted sideband in a measurement (usually called the image band). The reason is that the features of spectral lines in the image band can interfere with the measurement of the signal band. A common way to do this is by using a frequency selective interferometer, such as a Martin-Puplett interferometer [Goldsmith, 1998a], which transmits the signal band to the antenna while redirecting the image band. A disadvantage of such a device is that it has the potential to

set up standing wave cavities within the device, or to cause deformation of the signal beam (see Section 2.3.3).

Another way to separate the upper and lower sidebands is to use a sideband-separating mixer. A typical sideband-separating mixer configuration is shown in Figure 2.4. This is also the configuration of the mixer in SPÉIR's design. In this figure, the mixer block describes the element before the amplifiers, which contains the mixer chips, waveguides to direct the signals, and what is known as an RF quadrature hybrid. A quadrature hybrid (or just "hybrid") sums the signals from two inputs after applying a phase shift to each. The signal at one output of a hybrid is the first input plus the second input shifted in phase by  $90^\circ$ . The signal at the second output is the same situation except the phase shift is applied to the first input instead of the second. The configuration in Figure 2.4 shows two hybrids: one at the RF side of the mixers and one at the IF side. The general idea behind the sideband separation is that a shift is applied to the atmospheric signal (containing the USB and LSB) at the RF hybrid, the two outputs of the RF hybrid are combined with equal LO signals at two different mixers, and the two IF outputs of the respective mixers are combined in an IF hybrid. One output of the IF hybrid then contains the USB, while the other output contains the LSB.

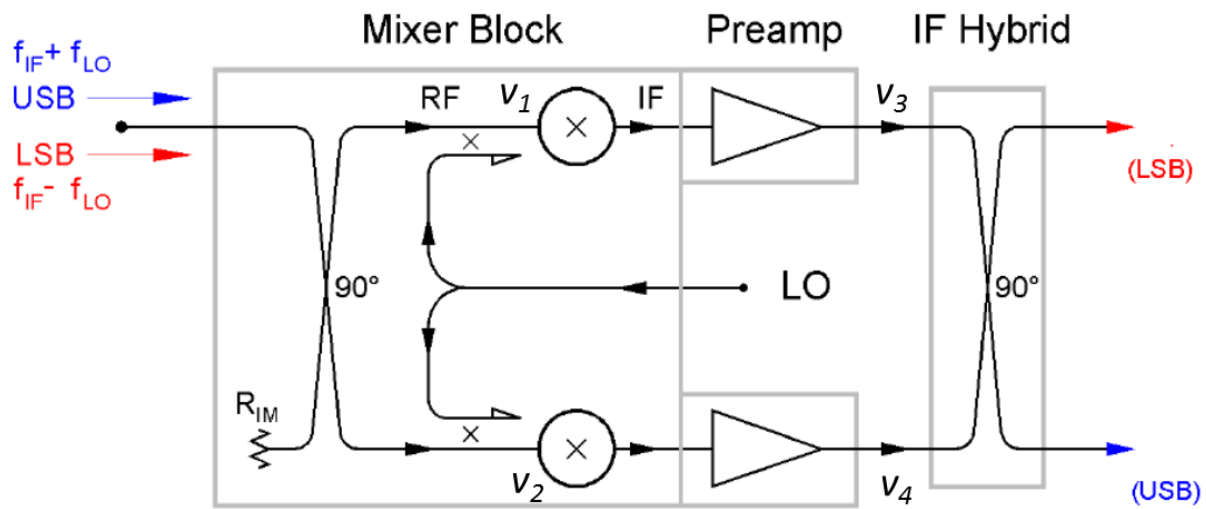


**Figure 2.4** Sideband-separating mixer configuration used for Band 6 of the Atacama Large Millimeter Array. Figure adapted from [Kerr et al., 2004]

The operation of the sideband-separating mixer is most easily understood by looking at the phase relationship of the USB and LSB. The inputs at the mixers as a function of time,  $t$ , are

$$v_1(t) = V_{rf} [\mu_{rf} e^{i(\omega_{rf} t)} + \mu'_{rf} e^{-i(\omega_{rf} t)}] \cdot V_{lo} e^{-i(\omega_{lo} t)} \quad (2.37)$$

and

$$v_2(t) = V_{rf} [\sigma_{rf} e^{i(\omega_{rf} t) - \pi/2} + \sigma'_{rf} e^{-i(\omega_{rf} t) - \pi/2}] \cdot V_{lo} e^{-i(\omega_{lo} t)}. \quad (2.38)$$

The unprimed quantities are from the USB and the primed quantities are from the LSB.  $\mu$  and  $\sigma$  are parameters that define the paths taken through the mixer block,  $\omega$  is angular frequency, and  $V$  denotes the power of a signal. The subscripts refer to the RF, IF, and LO signals. After down-conversion to the IF frequency we have

$$v_3(t) = aV_{if} [\mu_{rf} e^{i(\omega_{if} t - \phi)} + \mu'_{rf} e^{-i(\omega_{if} t - \phi)}] \quad (2.39)$$

and

$$v_4(t) = bV_{if} [\sigma_{rf} e^{i(\omega_{if} t - \pi/2)} + \sigma'_{rf} e^{-i(\omega_{if} t - \pi/2)}] \quad (2.40)$$

where  $a$  and  $b$  represent the respective gains of the mixers, and  $\phi$  is the phase error due chip misalignment and the IF path. In an ideal mixer  $a = b$  and  $\mu = \sigma$ , giving

$$v_3(t) = aV_{if} [\mu_{rf} e^{i(\omega_{if} t)} + \mu'_{rf} e^{-i(\omega_{if} t)}] \quad (2.41)$$

and

$$v_4(t) = aV_{if} [\mu_{rf} e^{i(\omega_{if} t - \pi/2)} + \mu'_{rf} e^{-i(\omega_{if} t - \frac{\pi}{2})}]. \quad (2.42)$$

These are the inputs to the IF hybrid. Propagating  $v_3$  through the hybrid with  $0^\circ$  phase delay and  $v_4$  with  $90^\circ$  phase delay, the sum at the output of the IF hybrid is only the LSB

$$\text{LSB} = aV_{if}e^{-i(\omega_{if}t)}. \quad (2.43)$$

Similarly, propagating the  $v_4$  with a  $0^\circ$  phase delay and  $v_3$  with a  $90^\circ$  delay gives only the USB at the other output

$$\text{USB} = -aV_{if}e^{i(\omega_{if}t)}. \quad (2.44)$$

### 2.3.3 Gaussian beams and quasioptics

The block diagram of Figure 2.2 shows the signal from the atmosphere directly entering the antenna. Antenna is often used ambiguously and can refer to a simple system comprising a reflector of some kind and a horn at which the radiation is focussed by the reflector, or may refer to a system containing more than one reflector. In this work, the word antenna will be used to refer to the horn that couples radiation from free space to a waveguide, and a parabolic reflector.

Quasioptics deals with the propagation of a beam of radiation that is reasonably well collimated but has relatively small dimensions when measured in wavelengths, transverse to the axis of propagation [Goldsmith, 1998]. Geometrical optics deals with radiation in the limit  $\lambda \rightarrow 0$  and optical elements many times this size, and diffraction effects dominate in the regime where  $\lambda \approx$  system dimensions. Quasioptics spans the middle-ground between these limits and the theory of Gaussian beam modes and Gaussian beam propagation is used. A Gaussian beam is the simplest solution to the paraxial wave equation [Goldsmith, 1998] and is one in which the amplitude of the electric field follows the form of a Gaussian distribution as you move radially from the beam axis. This is the fundamental Gaussian beam mode and horns radiate beams that are very nearly this shape, with some contribution from higher order modes. The beam can be considered as emanating from a beam waist in the horn. Focussing elements, such as lenses and mirrors, transform beams and produce different waist sizes (see Figure 2.5).

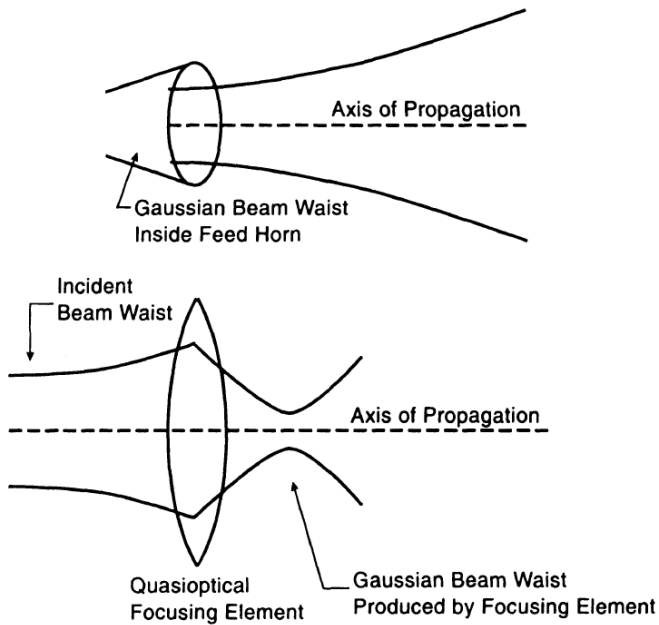


**Figure 2.5** Upper: A Gaussian beam propagating from a horn. Lower: A Gaussian beam being transformed by a focusing lens. Figure from [Goldsmith, 1998] with permission from Wiley.

The distribution of power density,  $P$ , in the beam at a radius,  $r$ , from the beam axis is given by

$$\frac{P(r)}{P(0)} = \exp \left[ -\left( \frac{r}{\omega} \right)^2 \right], \quad (2.45)$$

where  $\omega^1$  is the beam radius, defined as the point from the axis of propagation at which the amplitude of the electric field falls to  $1/e$  or its maximum value. The beam waist at distance  $z$  from the beam waist, along the axis of propagation, is calculated as

$$\omega = \omega_0 \left[ 1 + \left( \frac{\lambda z}{\pi \omega_0^2} \right)^2 \right]^{0.5}, \quad (2.46)$$

where  $\lambda$  is the wavelength of the radiation and  $\omega_0$  is the beam waist radius. When  $z$  is many times  $\omega_0$ , we are considered to be in the “far-field limit” of the beam propagation. In this limit,

---

<sup>1</sup>  $\omega$  is almost universally used as the symbol for angular frequency, and this is also the case for Gaussian beam radii. The symbol is used in this work with varying subscripts, and the difference between Gaussian beam propagation and the angular frequency of signals can easily be seen from the context in which it is used.

the beam radius grows linearly with distance. The power distribution of a Gaussian beam (Equation (2.45)) is plotted in Figure 2.6.

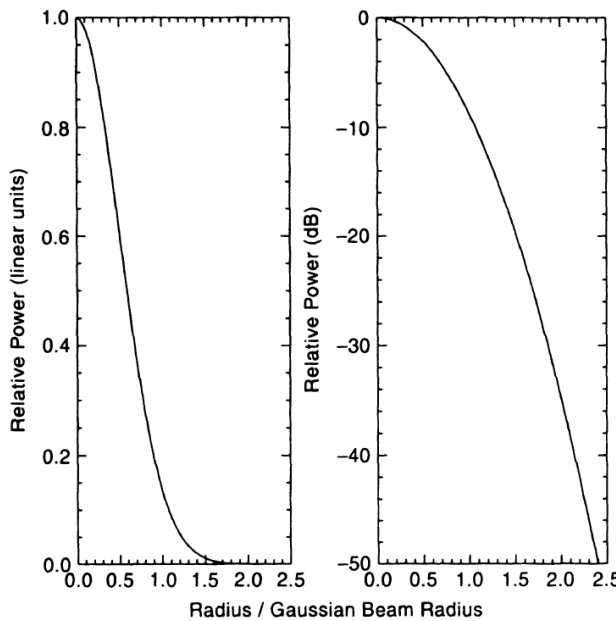


**Figure 2.6** The field distribution of the fundamental Gaussian beam mode in linear units (left), and in logarithmic units (right). The X-axis is the radius expressed in terms of the beam radius,  $\omega$ . Figure from [Goldsmith, 1998] with permission from Wiley.

The simple form of the radiation pattern emitted from a horn is that of an untruncated Gaussian beam. In reality, however, horns/antennas are finite apertures, and so must truncate the beam abruptly at some point, causing diffraction effects. In this case the beam no longer has a perfectly Gaussian form, but contains secondary maxima, called sidelobes. The electric field distribution in this case must be calculated numerically and resembles a *sinc* function. An edge taper of 20 dB can give sidelobes at approximately the -20 dB level. The radiation pattern for a horn/antenna describes the angular distribution of the beam power in the far field as a function of angle.

A useful quantity to describe how well an antenna detects radiation from a certain direction is the gain of the antenna system. For parabolic reflector and a horn, a good approximation for the antenna gain,  $G$ , is given by, [Minoli, 2009],

$$G = \frac{4\pi\eta A}{\lambda^2}, \quad (2.47)$$

where  $\eta$  is the antenna efficiency (typical ranges are 0.5 - 0.6), and  $A$  is the area of the physical aperture (the area of the reflector). The half-power beamwidth (HPBW) is the angular separation of the two points on the antenna radiation pattern at which the power has decreased by a factor of two (at -3 dB on the radiation pattern). For a parabolic antenna, the HPBW can be calculated as, [Minoli, 2009],

$$\theta_{HPBW} = 70 \frac{\lambda}{D}, \quad (2.48)$$

where  $D$  is the diameter of the reflector. The HPBW describes the spread of the beam in the far field. It can be seen through Equations (2.47) and (2.48) that the antenna gain and the HPBW are inversely related to each other.

The optics described in this work were intentionally kept relatively simple, in that the beam transformations only involve focussing a beam waist at infinity with a parabolic mirror. There is no need for detail on beam transformations as this situation is analogous to the geometric case, and the beam waist radius at the mirror can be found using Equation (2.46). To minimize any distortion to the beam, the optics have been designed as “slow”, meaning that focussing elements have long focal lengths by comparison to the wavelength, and the maximum bending angle is 45° [Murphy, 1987].

### 2.3.4 Atmospheric observations

When pointing the antenna to the atmosphere, the brightness temperature that the radiometer measures will be the sum of the brightness temperature of the atmosphere (and the cosmic background) and the brightness temperature radiated/generated by the instrument itself. The measured quantity is called the system temperature  $T_{sys}$

$$T_{sys} = T_A + T_{rec}. \quad (2.49)$$

$T_A$  is called the antenna temperature and, neglecting the cosmic background, is basically equal to the atmospheric spectrum  $T_{atm}$  (Equation (2.27)).  $T_{rec}$  is the power coming from the instru-

ment and is the temperature that a blackbody would have to have in order to generate the same power in the spectrometer if it completely illuminated the antenna.

The signal from the atmosphere is amplified by orders of magnitude, and so small variations in the total system gain of the radiometer over time (due to changes in the power supply, or the temperature of the lab, for example) can affect the measurement. For this reason, and because the radiometer measures in absolute units, the radiometer must be calibrated often. The response of a radiometer is assumed to be linear, meaning that the atmospheric spectrum can be calibrated by the measurement of the signal from two blackbody calibration targets (loads). The blackbody targets are both kept at known “hot” and “cold” temperatures ( $T_h$  and  $T_c$ , respectively) relative to the brightness temperature of the atmosphere and are used to determine the linear function of the radiometer. The uncalibrated spectral intensity of the atmospheric measurement,  $M_{atm}$ , is related to the brightness temperature of the atmosphere through the relation

$$T_{atm} = \frac{M_{atm} - M_c}{M_h - M_c} (T_h - T_c) + T_c, \quad (2.50)$$

where  $M_c$  and  $M_h$  are the signals measured from the cold and hot targets respectively. This measurement is known as a “total power measurement”. The receiver temperature can also be calculated from

$$T_{rec} = \frac{T_h - YT_c}{Y - 1}, \quad (2.51)$$

where  $Y = M_h/M_c$ .

In the case of measuring a weak atmospheric spectral line, such as H<sub>2</sub>O or ClO, nonlinearities in system gain of the radiometer (nonlinear differences in the gain of individual spectrometer channels, for example) are on the order of the intensity of the spectral line and can interfere with the measurement. In this case, a balanced calibration can be performed [Parrish et al., 1988; Straub et al., 2011]. This method uses the difference between the atmospheric signal and a quasi-frequency independent signal (e.g., from a blackbody) in order to remove the effects of the system gain differences. The difference spectrum is calculated as

$$T_{balance} = T_{atm} - T_{ref} = \frac{M_{atm} - M_{ref}}{M_h - M_c} (T_h - T_c), \quad (2.52)$$

where  $T_{ref}$  and  $M_{ref}$  are the brightness temperature and uncalibrated spectral intensity of the reference target, respectively. The resulting spectrum is barely influenced by nonlinearities in the gain of the system. In the case of a balanced measurement, 50% of the measurement time is devoted to observing the reference beam. The hot-cold calibration is also still used, but can be made less frequently [Krupa et al., 1998].

In both cases, the attenuation of the spectral line signal by the atmosphere must be taken into account. For the total power measurements, this is done during the inversion (see Section 2.4.2). For balanced measurements, the difference spectrum is corrected using knowledge of the optical depth of the atmosphere. The optical depth of the atmosphere can be found using tipping measurements. This technique uses brightness temperature measurements of the atmosphere at one or more observation angles to determine the zenith optical depth,  $\tau_z$  [Han and Westwater, 2000]. With this and the air mass factor,  $A$ , for the signal path through the atmosphere, the correction factor for the spectrum is  $\exp(-A\tau_z)$  [Krupa et al., 1998].

The level of noise on a spectrum is directly proportional to the system temperature in Equation (2.49). The component from the atmosphere (antenna temperature) is unavoidable as it is the measured quantity, and it is desirable to have a receiver temperature (usually defined by the mixer and first IF amplifier) as low as possible (see Section 2.3.1). The noise on a spectrum,  $\Delta T$ , is given by the radiometer formula [Kraus, 1986]

$$\Delta T = \frac{aT_{sys}}{\sqrt{\Delta v t}}, \quad (2.53)$$

where  $\Delta v$  is the frequency resolution of the spectrometer (spacing between spectrometer channels) and  $t$  is the integration time for a spectrum, and  $a$  is a factor that depends on the observation technique.  $a$  is 1 for a total power measurement, and 2 for a balanced measurement. The resolution of the spectrometer is fixed for a measurement and so a reduction in the noise on the spectrum is achieved through longer integration times.

## 2.4 Inversion theory

### 2.4.1 The ill-posed problem

The measured quantity with a millimeter wave detector is the intensity of the atmospheric radiation. The desired quantity is the vertical concentration profile of a species in the atmosphere, which is found through the absorption coefficient. This requires that we calculate the inverse of the radiative transfer equation (Equation (2.27)). This is difficult to solve because it is an inherently ill-posed problem [Hansen, 1992]. Such problems are characterised by the fact that arbitrarily small perturbations on the right-hand side of Equation (2.27) can lead to arbitrarily large perturbations of the solution (often colloquially referred to in atmospheric remote sounding as oscillations). In other words, the solution is very sensitive to perturbations (noise on the spectrum in the case here). In the case of an atmospheric measurement of many intensities at many different frequencies, the problem has already been discretized and we have a matrix problem  $\mathbf{Ax} = \mathbf{b}$ , in which the ill-conditioning of the linear system is closely connected to the ill-posedness mentioned above. To compute a reasonable, and unique, solution to the problem, the components associated with small perturbations must be somehow filtered out. This is usually done by applying some form of regularization to the problem. In this work the optimal estimation method (OEM) is used, in which an a priori estimate of the solution is used to impose stability and determine a solution.

### 2.4.2 Optimal estimation

To infer atmospheric concentrations  $\mathbf{x}$  from a measurement  $\mathbf{y}$ , one needs a forward model  $\mathbf{F}(\mathbf{x})$  to describe the radiative transfer through the atmosphere, and an inverse model  $\mathbf{L}(\mathbf{y})$ . The complete forward model can be divided into two parts: one part,  $\mathbf{F}_r$ , which deals with the radiative transfer through the atmosphere and the intensity of the radiation arriving at the instrument receiver,  $\mathbf{i}$ ,

$$\mathbf{i} = \mathbf{F}_r(\mathbf{x}_r), \quad (2.54)$$

and another,  $\mathbf{F}_s$ , which deals with the instrument characteristics and data reduction

$$\mathbf{y} = \mathbf{F}_s(\mathbf{i}) + \boldsymbol{\varepsilon}. \quad (2.55)$$

$\mathbf{F}_s$  is implemented through a series of response matrices,  $\mathbf{H}_j$ , the multiplication of which constitute the combination of all of the sensor characteristics [Eriksson, 2005]. The full forward model is written as

$$\mathbf{y} = \mathbf{F}(\mathbf{x}) + \boldsymbol{\varepsilon}. \quad (2.56)$$

Using the Rodgers formalism [Rodgers, 2000] for a linear forward model, the measurement of the atmosphere can be expressed as  $\mathbf{y} = \mathbf{K}\mathbf{x} + \boldsymbol{\varepsilon}$ , where  $\mathbf{K}$  is the Jacobian of the forward model with respect to  $\mathbf{x}$  and  $\boldsymbol{\varepsilon}$  is the noise on the spectrum ( $\mathbf{K} = \delta\mathbf{y}/\delta\mathbf{x}$  is also referred to as the weighting function matrix).

Optimal estimation gives the most probable estimate of the true state,  $\mathbf{x}$ , on the basis of the measurement,  $\mathbf{y}$ , the a priori,  $\mathbf{x}_a$ , and the Jacobian,  $\mathbf{K}$ . Using Gaussian statistics, the a priori knowledge of the atmosphere, the probability of a certain true state,  $P(\mathbf{x})$ , can be described as

$$-2\ln(P(\mathbf{x})) = (\mathbf{x} - \mathbf{x}_a)^T \mathbf{S}_a^{-1} (\mathbf{x} - \mathbf{x}_a) + \mathbf{c}_1, \quad (2.57)$$

and the probability of a true state, given a measurement,  $P(\mathbf{x}|\mathbf{y})$ , is

$$-2\ln(P(\mathbf{y}|\mathbf{x})) = (\mathbf{y} - \mathbf{K}\mathbf{x})^T \mathbf{S}_e^{-1} (\mathbf{y} - \mathbf{K}\mathbf{x}) + \mathbf{c}_2, \quad (2.58)$$

where  $\mathbf{S}_a$  and  $\mathbf{S}_e$  are error covariance matrices (ECMs) for the a priori and the measurement noise, respectively, and  $\mathbf{c}_1$  and  $\mathbf{c}_2$  are constants. Climatological information is often used to construct  $\mathbf{S}_a$  and the measured spectrum and instrument parameters are used to construct  $\mathbf{S}_e$ . From Bayes theorem, the probability of the true state, given a measurement, is

$$-2\ln(P(\mathbf{x}|\mathbf{y})) = (\mathbf{x} - \mathbf{x}_a)^T \mathbf{S}_a^{-1} (\mathbf{x} - \mathbf{x}_a) + (\mathbf{y} - \mathbf{K}\mathbf{x})^T \mathbf{S}_e^{-1} (\mathbf{y} - \mathbf{K}\mathbf{x}) + \mathbf{c}_3, \quad (2.59)$$

where  $\mathbf{c}_3$  is a constant. The solution of the most probabilistic state,  $\hat{\mathbf{x}}$ , is found by minimising the right-hand side of Equation (2.59), known as the cost function ( $J_c$ ), with respect to  $\mathbf{x}$ . The compact form of the solution is

$$\hat{\mathbf{x}} = \mathbf{x}_a + \mathbf{G}(\mathbf{y} - \mathbf{K}\mathbf{x}), \quad (2.60)$$

where  $\mathbf{G} = \mathbf{S}_a \mathbf{K}^T (\mathbf{K} \mathbf{S}_a \mathbf{K}^T + \mathbf{S}_e)^{-1}$ .  $\mathbf{G}$  describes the sensitivity of the retrieved state to the measurement:  $\mathbf{G} = \delta \hat{\mathbf{x}} / \delta \mathbf{y}$ . By inserting  $\mathbf{y} = \mathbf{Kx} + \boldsymbol{\varepsilon}$  in Equation (2.60) we obtain an alternative form of the solution that expresses the relative contributions of the a priori and measurement information:

$$\hat{\mathbf{x}} = \mathbf{Ax} + (\mathbf{I} - \mathbf{A})\mathbf{x}_a + \mathbf{Ge}. \quad (2.61)$$

$\mathbf{A} = \mathbf{GK}$  is referred to as the averaging kernel matrix and is a measure of the sensitivity of the retrieval to the true atmospheric state:  $\mathbf{A} = \delta \hat{\mathbf{x}} / \delta \mathbf{x}$ .

$\mathbf{K}$  and  $\mathbf{A}$  can be used to determine the range of the atmosphere over which gases can be detected or the retrieval of gas concentrations can be made; the measurement response,  $\mathbf{w}_m$ , is used to define the altitude limits of a retrieval and is defined as the sum of the rows of  $\mathbf{A}$ .  $\mathbf{A}$  also gives an estimate of the altitude resolution of the retrieved atmospheric profiles. The estimated total error in the retrieved state can be expressed as

$$\mathbf{S}_{tot} = (\mathbf{A} - \mathbf{I})\mathbf{S}_a(\mathbf{A} - \mathbf{I})^T + \mathbf{GS}_e\mathbf{G}^T + \mathbf{GK}_b\mathbf{S}_b\mathbf{K}_b^T\mathbf{G}^T, \quad (2.62)$$

where  $\mathbf{K}_b$  and  $\mathbf{S}_b$  are the Jacobian and error covariance for the forward model (or background) parameters, respectively. The first term on the right is the “smoothing error” arising from the limited vertical resolution of the measured profile. The second term is the “measurement error” due to noise on the measurement and the third term is the “background error” due to uncertainties in the background parameters in the forward model. The sum of the smoothing error and the measurement error is referred to as the retrieval precision,  $\mathbf{S}$ . Whether a variable is considered part of the state vector,  $\mathbf{x}$ , or part of the background parameters is defined when choosing what will be retrieved in the inversion.

For the calculation of the errors due to uncertainties in the forward model parameters,  $\mathbf{GK}_b$  can be considered as an averaging kernel matrix for the parameters:  $\mathbf{GK}_b = \mathbf{A}_b = \delta \hat{\mathbf{x}} / \delta \mathbf{b}$ . The covariance matrix for the background parameters,  $\mathbf{S}_b$ , is constructed based on estimates of the uncertainties in instrument, atmospheric, or spectroscopic parameters, for example. In Chapter 5, systematic errors due to uncertainties in the spectroscopic parameters of molecules in SPÉIR’s frequency range are included as part of  $\mathbf{S}_b$ .

### 2.4.3 Linearity of the observing system

The OEM described here assumes a forward model that is linear, however, this may not be the case for radiative transfer through the atmosphere under certain conditions (e.g., high opacity). For a nonlinear case there is no general explicit expression to find the optimal solution, as there is for a linear case [Rodgers, 2000], and the solution must be found numerically and iteratively. The reason is that in the nonlinear case,  $\mathbf{K}$  depends on the atmospheric state. Linearization is adequate for error analysis and characterization of a moderately nonlinear problem [Tarantola and Valette, 1982], but the result of an inversion will vary for each measurement and so it is important to use the weighting functions for each individual retrieval rather than representative ones.

A simple test based on measurement response can be performed to assess the nonlinearity of an inversion scheme. The test identifies retrieval altitudes that display a nonlinear response to changes in the atmospheric VMRs. While giving information about the relative degree of nonlinearity, the test is of a qualitative nature and far from complete for accurately quantifying the degree of nonlinearity. It can be used, however, to determine whether a linear inversion scheme is sufficient to retrieve gas VMRs from a spectrum, which greatly decreases computing time.

Using Eriksson's formalism in [Eriksson and Jiménez, 1998; Eriksson, 1999], the theoretical response,  $\mathbf{w}_m$ , should be equal to the practical response,  $\mathbf{w}_{pm}$ , for a perfectly linear inversion that retrieves gas concentrations in units of fractions of the a priori. The practical measurement response for target species  $i$  is given by  $\mathbf{w}_{pm} = (\hat{\mathbf{a}} - \mathbf{x}_{ai})/c$ , where  $\hat{\mathbf{a}}$  is the retrieved profile from an inversion using a true state for the target gas given by  $\mathbf{x}_{ai}(1 \pm c)$ .  $c$  is a real number in the range  $(0,1)$ . This true state is the a priori profile for the target gas increased/decreased (corresponding to the  $+$ / $-$  in the expression respectively) by the same factor at each altitude, and the true states of all other gases are given by their own a priori. The procedure is done here using both a linear and a nonlinear inversion scheme (Section 4.3.5), and is as follows: The a priori is increased uniformly by a factor of 1.3 ( $c = 0.3$ ) for a given target gas and fifty identical spectra are created using this as the true state, each with different measurement noise. These spectra are inverted and the fifty retrieved profiles are averaged in order to reduce effects specific to a

## 2. Background and methodology

---

single measurement noise spectrum. This process is repeated for a uniform decrease of the a priori ( $c = -0.3$ ) and the practical measurement response,  $\mathbf{w}_{\text{pm}}$ , is calculated for the target species each case ( $c = \pm 0.3$ ) using the average retrieved profile. The practical measurement response of a target species to a retrieved interfering species is calculated in a similar way, but by increasing/decreasing the interfering species' a priori to create its true state, while keeping the target gas true state as its own a priori.

# Chapter 3

---

## 3 SPÉIR instrument

This chapter describes the design of SPÉIR, a millimeter-wave instrument upon which a lot of the work in this thesis is based. The instrument is currently in the post-design phase. The main goal is to have an instrument in the Canadian Arctic capable of making year-round measurements of ClO and other gases related to stratospheric ozone. The main aims when designing SPÉIR were: to have an instrument with high sensitivity that enables the detection of the weak atmospheric ClO signature on a timescale of hours; to minimize the occurrence of standing waves in a measurements due to coherent reflections in the instrument; to have a high horizontal measurement resolution in the stratosphere; to have a quasioptical system with few moving parts; and to have a setup that can be made to work autonomously and withstand the High-Arctic environment. The design and construction of a new instrument is accompanied by inherent challenges, but also some benefits, e.g., the instrument can be tailored specifically to the scientific goals, and the individual parts can be sourced from different industrial partners and academic institutions, as was done here. The details of the instrument that are presented here are mainly those which are directly related to its characteristics as part of the whole observation system, and so Chapter 4, which describes the simulation of the observation system, is closely related.

The design of SPÉIR has received input from many sources. In particular, a design study was performed in partnership with Thomas Keating Ltd (TK). TK provided input on the design of SPÉIR, and the choice of components to best meet our needs. Dr. Richard Wylde headed the TK partnership and Stuart Froud produced all of the technical Computer-Aided Design (CAD) drawings for SPÉIR in this work, unless otherwise stated. Dr. Anthony Kerr of the National Radio Astronomy Observatory (NRAO) provided input on mixer/preamplifier related issues for

SPÉIR. Dr. Axel Murk at the Institute of Applied Physics (IAP), University of Bern, provided input on aspects of the design choices for SPÉIR. Boris Pavlovic worked on the development of the computer interface for the instrument and collaborated on the periscope design. Bradley Kloostera continued the development of the computer interface and the instrument data management.

### 3.1 Introduction

SPÉIR (meaning “SKY” in Irish) is a millimeter-wave radiometer that has been designed to measure electromagnetic radiation emitted from the atmosphere between 265 – 280 GHz. This spectral range was chosen as it contains signatures from rotational transitions of O<sub>3</sub>, HNO<sub>3</sub>, N<sub>2</sub>O, and ClO: the target species. This spectral region has been utilized for several ground-based instruments, including MIRA 2 (Millimetre-wave Radiometer 2) [Berg et al., 1998] and RAMAS (Radiometer for Atmospheric Measurements At Summit) [Golchert et al., 2005], as well as those used for the first published measurements of the diurnal variation of stratospheric ClO [Solomon et al., 1984], and for the first observation of enhanced lower stratospheric ClO in the Antarctic ozone hole [de Zafra et al., 1987; Solomon et al., 1987].

An effort was made to employ as few optical elements in the design as possible. The advantages of this are of course cost, size, and weight, and also that there are fewer elements which have the potential to cause unwanted effects in the measured radiation beams, or occupy space in the cryostat<sup>2</sup>. The reasons behind the various design choices are explained in each section.

Figure 3.1 shows a labelled schematic of the quasioptical setup, that will be used to refer to specific components labeled in curly brackets “{}”. More detailed drawings will be introduced where needed. It is often convenient, when talking about beam propagation, to consider the beam originating at the feedhorn (or just “horn”) and propagating through the other optical

---

<sup>2</sup> The word “cryostat” refers here to the passive device used to maintain the mixer and some other components at cryogenic temperatures. “Cryocooler” is used to describe the device that actively cools the inside of the cryostat down to cryogenic temperatures. “Dewar” (often a synonym for cryostat) is used here to describe a cryostat that is used solely to store cryogenic liquids such as liquid nitrogen.

components, towards the atmosphere or calibration targets. The propagation is completely reversible in time [Kraus, 1988] and so the optical system will be interchangeably referred to as a transmitter (time-reversed view) as well as a receiver, whenever one is more convenient.

SPÉIR will be housed indoors at PEARL (Section 1.1), with access to the outside provided by an aperture in the wall of the laboratory building. For an atmospheric measurement, the signal from the sky enters the building via a periscope system (Section 3.2.2). The signal enters the optical bench setup (see Figure 3.1) and is reflected through  $90^\circ$  by a polarising wire grid, {2}, passed through a path length modulator (PLM), {3}, and is focussed by a parabolic mirror, {4}, into the cryostat, {5}, where it is coupled to one of the horn antennae, {6}. The horn couples the radiation to the mixer block, {C}, where it is mixed with the local oscillator signal, {E}, signal that enters the opposite side of the mixer block through an identical horn, {6}. The resulting downconverted signal (see Section 2.3.1) is amplified by a cooled low noise amplifier (LNA), {D}, before exiting the cryostat for some post-processing, and spectrum analysis. For a reference beam or calibration measurement, mirror {1} is rotated so that it blocks the signal from the atmosphere and directs the radiation from the calibration targets, {7} and {8}, towards the mixer.

In the description here, the instrument is divided into two main parts. The front-end refers to all of the components, mainly optical, that are involved in guiding radiation to the SIS mixer block. The horns and the optical bench {10} are also considered here as part of the front-end. The back-end refers to all of the other components, “after” the signals have been sent to the mixer block.

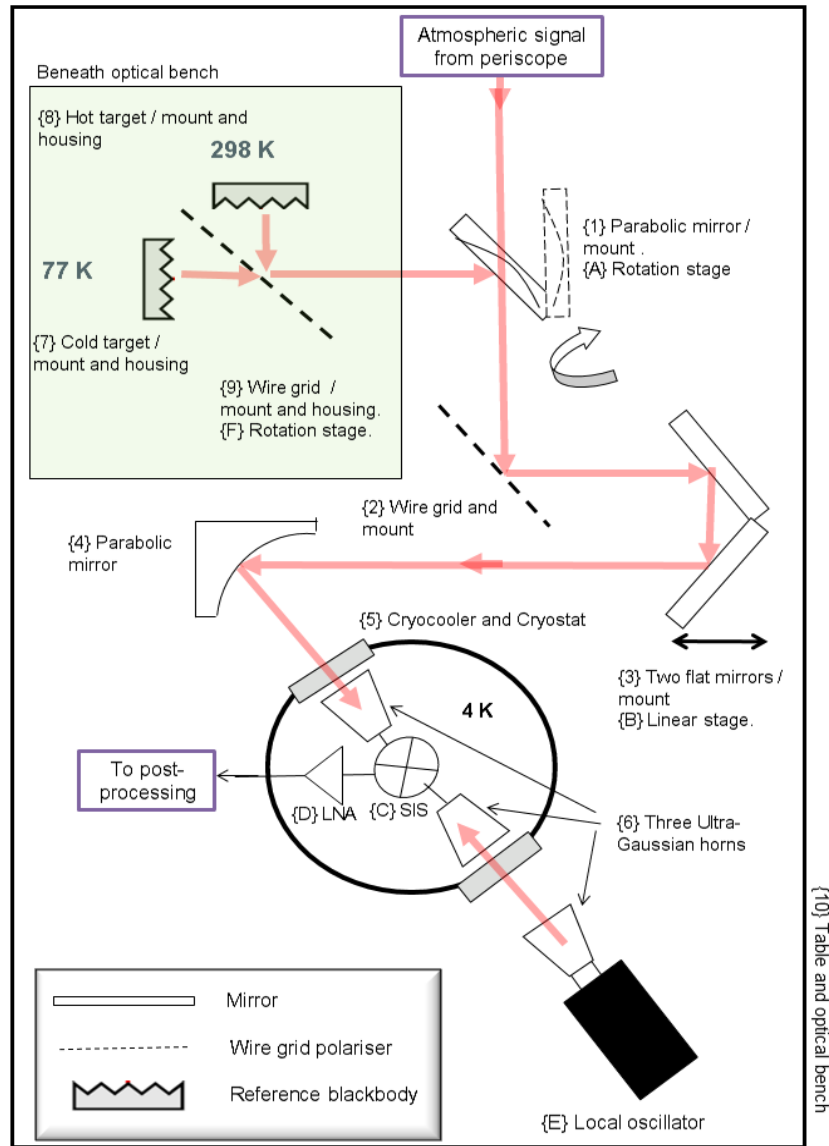


**Figure 3.1** Schematic of the signal propagation through the SPÉIR quasioptics.

## 3.2 Front-end

### 3.2.1 Ultra-Gaussian horn antenna

There are three horns included in the design of SPÉIR: two which receive radiation from the atmosphere/reference and local oscillator respectively, and one which transmits the local oscillator signal into free space. The horns are spherical corrugated feeds which couple the TE<sub>10</sub> mode (no E-field in the direction of the wave) in the rectangular waveguide of the mixer block,

via the HE<sub>11</sub> mode (no E-field or B-field in the direction of the wave), to the fundamental Gaussian beam mode at the horn aperture. Corrugated horns have excellent polarisation purity, meaning that the horn is only sensitive to a fixed polarisation of the Gaussian beam [Clarri-coats and Oliver, 1983].

The design of the corrugated spherical horns in SPÉIR provide very low sidelobes and reduce standing wave signatures in optical systems by maximising coupling to the fundamental Gaussian beam mode [Cruickshank, 2007]. The novel design works by introducing a straight section of the corrugated guide in addition to the usual profiled section. It is known that profiled horns can excite the higher order modes in addition to the dominant HE<sub>11</sub> mode, and the straight section is designed to be such a length that the HE<sub>11</sub> mode and the higher order HE<sub>12</sub> mode are brought into phase at the horn aperture. The two modes then combine to produce a highly pure fundamental Gaussian mode beam with very low sidelobes in the far field (see Section 2.3.3): coupling efficiencies as high as 99.8% can be achieved, compared to  $\sim 98\%$  with other designs [Goldsmith, 1997]. The far field antenna pattern for the ultra-Gaussian horn for SPÉIR is shown in Figure 3.2. The gain of the antenna is 27.7 dB and the sidelobes have a low relative intensity at <-35 dB.

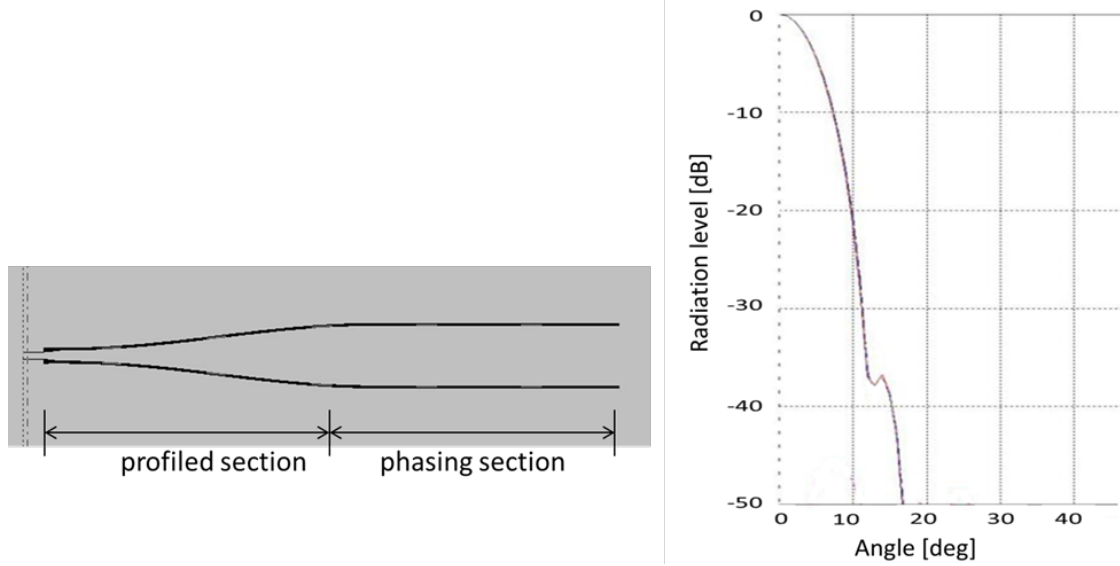


**Figure 3.2** Left: horn profile showing the profiled section designed to excite the HE<sub>12</sub> mode and the straight section to bring it into phase with the HE<sub>11</sub> mode. Right: far field antenna pattern of the horns in SPÉIR. The plots are modified from originals provided by Richard Wylde of Thomas Keating Ltd.

### 3.2.2 Quasioptical setup and signal propagation

The system was designed to have few focussing elements, and where needed, it was preferred to have long focal lengths (slow optics) to minimize distortions in the beam [Murphy, 1987]. The beam transmitted from the horn has a waist radius of 3 mm and propagates to a parabolic mirror, {4}, with a focal length of 150 mm. From this mirror the beam is transformed to be focussed at infinity and all other optics encountered before the atmosphere have no curvature so this is the beam that propagates into the atmosphere. CAD drawings in Figure 3.3 and Figure 3.4 illustrate the components and beam. The gain of the simple parabolic mirror and horn combination is 43.01 dB and this corresponds to an approximate HPBW of 0.9°. Considering the beam in the atmosphere, this gives a horizontal resolution of approximately 2.5 km at an altitude of 30 km (25° elevation angle. See Section 4.2). The two plane mirrors, {3}, form a roof mirror that is mounted on a motorised linear stage and act as a PLM, included to suppress standing waves set up between optical elements. The polarising wire grid, {2}, is used predominantly as a plane reflector to direct the beam toward the PLM and will have absorbing material held in the housing at the back of the grid. Each of the optical elements has a minimum cross-sectional radius (or clear aperture radius) that is 2.5 times the beam radius at the beam/element interface. This means that >99.99% of the power in the fundamental beam falls within this area, and minimizes diffraction effects at the edges of the elements. The parameters of the beam as it passes through the quasioptical setup are given alongside a CAD drawing of the beam propagation in Figure 3.5.

When the parabolic mirror, {1}, is not in the beam path, the beam leaves the optical bench and is passed through an opening in the side of the laboratory wall to the outside. In order to direct the beam skyward, a periscope mirror was designed that can direct the beam through 180° from one horizon to another. The design (Figure 3.6) consists of two concentric cylinders: a fixed outer casing and an inner casing moveable through 360°. The inner cylinder contains a plane mirror at 45° to the beam path and an aperture with a cross-sectional radius of 2.5 times the beamwidth. The outer cylinder has a cut section that allows the beam to exit when the mirror points at  $\geq 0^\circ$  elevation. When turned to  $-90^\circ$  elevation, the aperture is completely closed off by the outer cylinder to protect it from bad weather conditions. Warm air from inside will be continuously blown though the opening in the wall to prevent frost build up at the hot-cold in-

terface and a slight gradient in the radius of the outer cylinder allows any captured precipitation to flow away from the mirror and be released.

When the parabolic mirror, {1}, is moved into the beam path, the signal from the horn is directed down towards the hot and cold calibration targets beneath the optical bench (see Figure 3.7). The beam first reaches a rotatable polarising grid {9} which, depending on its angle of rotation, transmits the beam towards the cold calibration target, or reflects the beam towards the hot target (see Section 3.2.4). Mirror {1}, was made parabolic instead of plane in order to focus the beam through the polarising grid's clear aperture with the required radial cut-off of 2.5 times the beam radius. This is achieved with a relatively long focal length of 500 mm, as shown in a cross-section view of the calibration targets in Figure 3.7. A 90° rotation of the beam is not ideal but the focal length of the mirror is many times its diameter so the effects on the beam are minimal [Murphy, 1987].

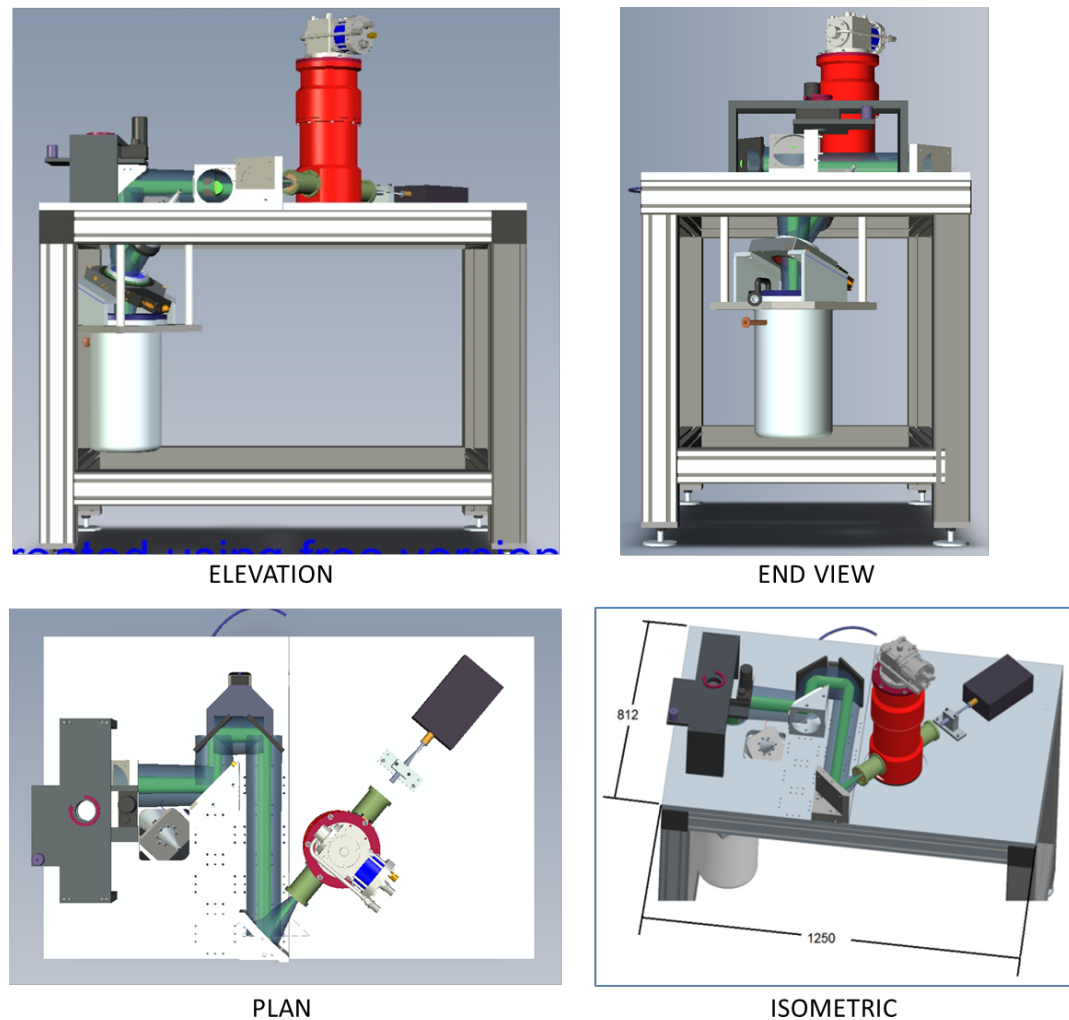


**Figure 3.3** 3D CAD drawings showing the elevation, plan, end view, and isometric view of SPÉIR. The calibration system is held beneath the optical bench. The length and width of the optical bench is shown in mm in the isometric view. The beam also is also included, with solid green indicating the  $(1/e)$  beamwidth and transparent blue indicating 2.5 times the beamwidth. Refer to Figure 3.1 for a schematic of the plan rotated clockwise by  $90^\circ$ . Drawings by Stuart Froud at TK.

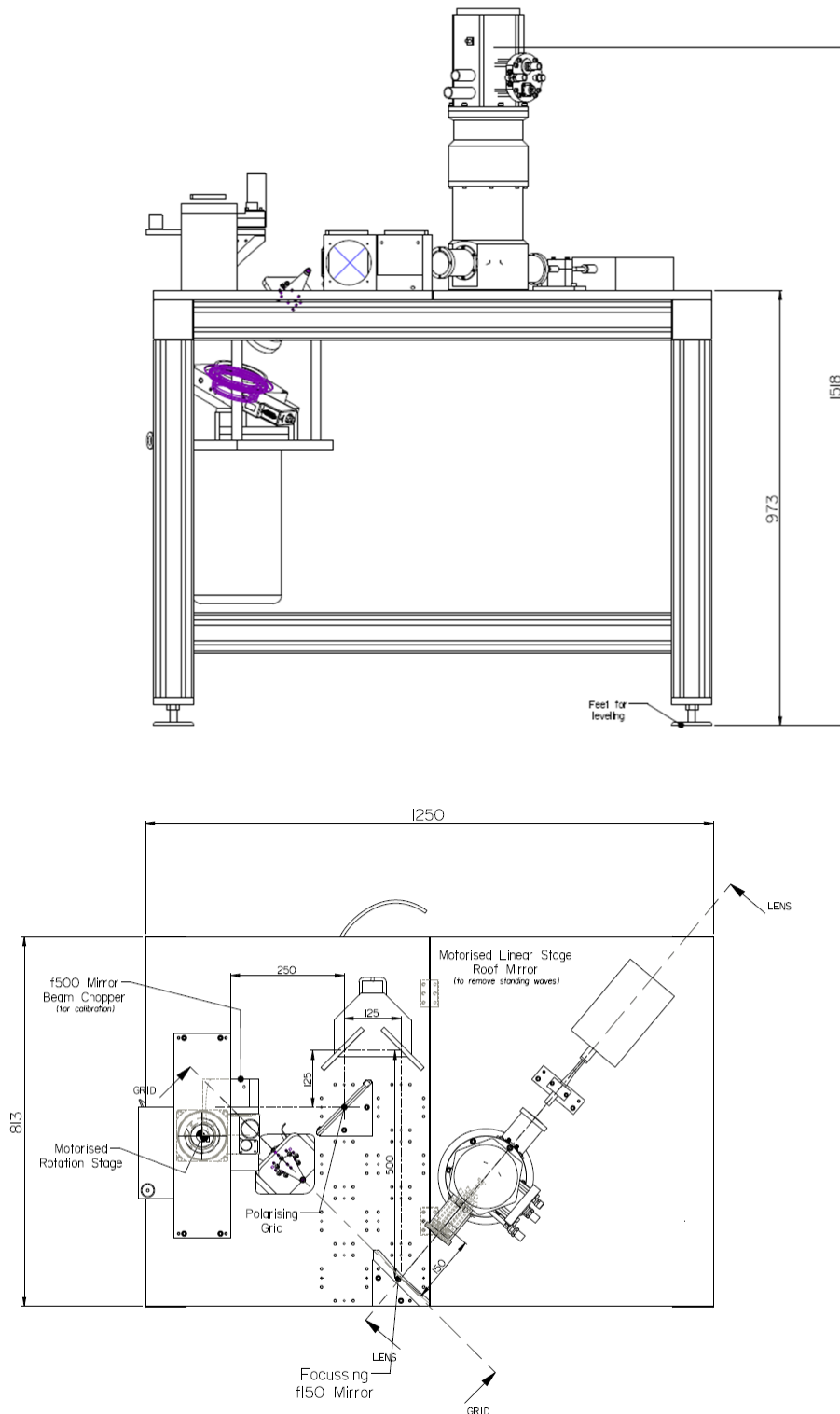


**Figure 3.4** CAD drawing showing elevation (upper) and plan (lower) with general dimensions and labels for the main elements on the optical bench. Also refer to Figure 3.1 for a schematic of the plan rotated clockwise by 90°. Drawings by Stuart Froud at TK. Dimensions are in mm.

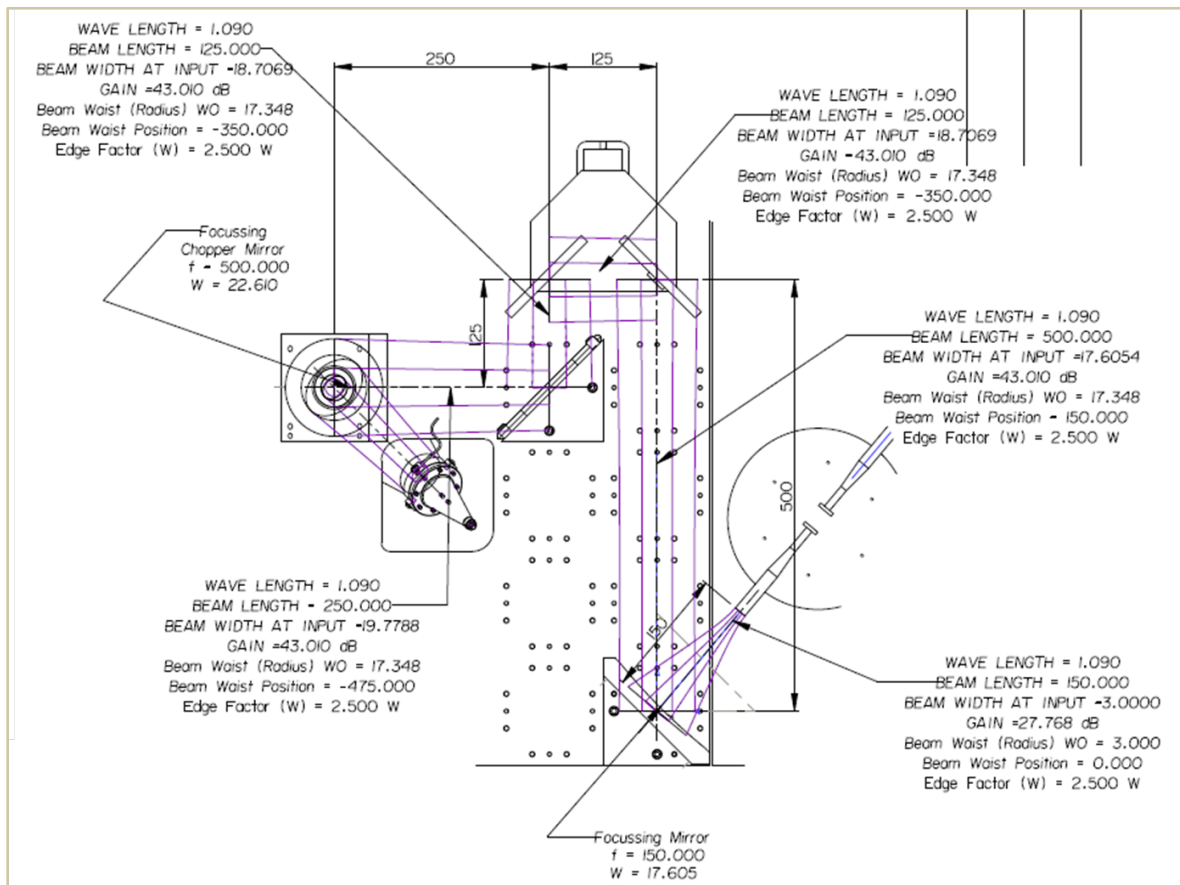


**Figure 3.5** CAD drawing showing the parameters of the beam as it propagates through the quasi-optical setup of SPÉIR. Drawings by Stuart Froud at TK. Dimensions are in mm.

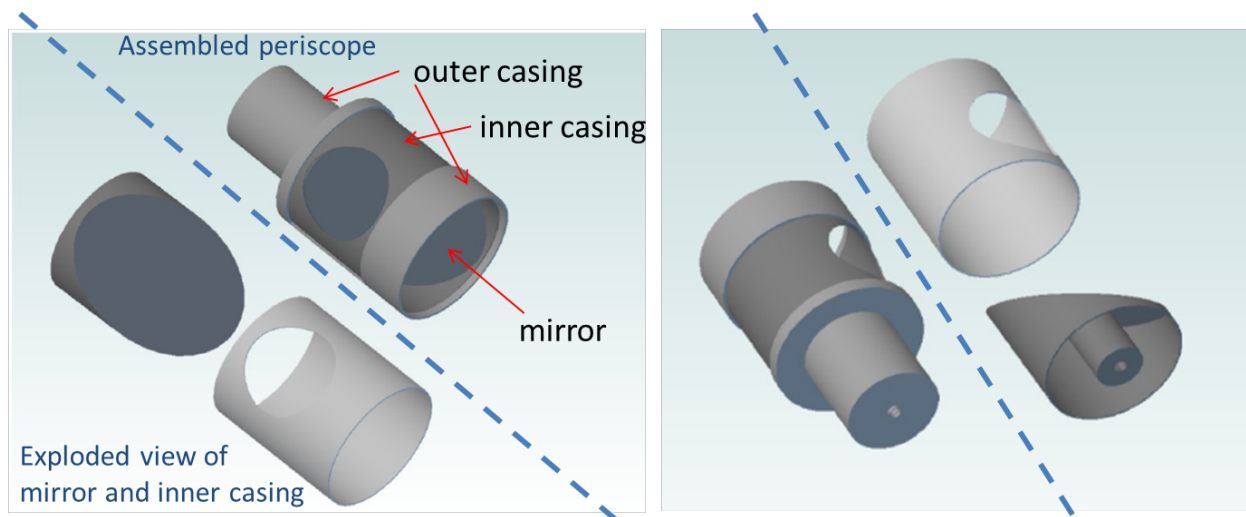


**Figure 3.6** Left: front view of the periscope design for SPÉIR (Section 3.2.2). Right: rear view. Figures are modified from originals provided by Boris Pavlovic at UofT.

### 3.2.3 Calibration loads

Requirements for millimeter wave calibration targets are high emissivity, low temperature gradients, high coupling efficiency, and low coherent return loss (low coherent reflection/backscatter that can cause standing waves). Coherent backscatter ( $S_{11}$ ) from a calibration target results in standing waves being set up between the target and the receiver. These should be kept as small as possible for spectroscopic measurements as the standing wave signal can greatly degrade the signal-to-noise ratio of the system. The calibration targets in SPÉIR are conical shaped targets made of a carbon loaded polypropylene absorber, developed by TK. The conical shape provides very low  $S_{11}$  due to multiple reflections and absorptions within the cone (see Figure 3.8).  $S_{11} < -65$  dB has been observed for active backscatter measurements at 300 GHz, compared to  $\sim -55$  dB for other designs [Murk et al., 2012].

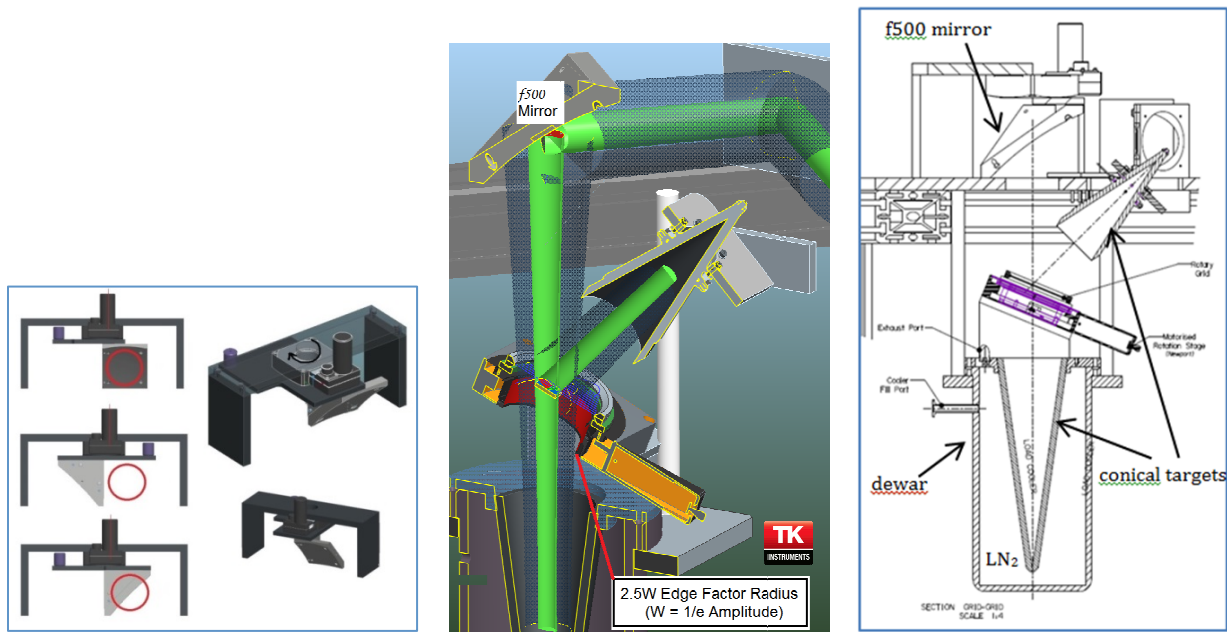


**Figure 3.7** Left: 3D CAD drawing of the mechanism for the parabolic mirror, {1} in Figure 3.1, as it moves in and out of the beam. The cross section of 2.5 times the beam radius is shown by the red circle. Middle: cross-sectional view of the mirror, the blackbody targets, and the rotatable grid of the calibration system. The hot target is fixed to the optical bench and the cold target sits in a dewar of liquid nitrogen. Right: CAD drawing showing an end view cross-section of the mirror, calibration targets, and rotatable grid. Drawings by Stuart Froud at TK.

Thermal gradients within the target lead to a difference between its effective temperature and the temperature reading made using sensors on the target. This causes an error in the calibration of the power received from the atmosphere. The polymer absorber of the cone has a low thermal conductivity which is problematic for the hot (at ambient temperature) target. This hot target for SPÉIR consists of a thin layer of the polymer on a thermally conducting metal backing. The backing is also kept thermally isolated to reduce error from sudden temperature changes in the lab. The cold target consists of a polymer cone submerged in a dewar of liquid nitrogen ( $\text{LN}_2$ ) and is not expected to have significant thermal gradients except near the aperture of the cone. The orientation of the cones is also important for thermal stability and so the cold and hot cones are situated such that their apertures are facing up and down, respectively, to reduce convection effects (see Figure 3.7). Platinum thermal resistors provide temperature measurements of the cone surface. The thermal gradients will be highest at the aperture and so the beam radii at the targets were made such that the beams intersect the polymer at a point farther into the cone, away from the aperture (see Figure 3.7). This is accomplished with the f500 parabolic mirror, {1}. The smaller beam also means that the cones can be angled slightly away from having the aperture plane at  $90^\circ$  to the beam, to reduce S11 from the inner apex of the cone (the one point on the inner surface which may be parallel to the aperture plane).

Preliminary radiation measurements of the cold target design were performed by Dr. Axel Murk at the Institute of Applied Physics, Bern, and indicated a flaw in the design: It was quite explosive. A combination of maintaining the cone at 77 K and the aperture-up orientation caused some oxygen gas (boiling point = 90 K) in the air to condense and pool inside of the cone. Liquid oxygen is highly explosive in the presence of organic material and so the design was modified: the dewar design now has fittings to seal a transparent (at mm-wave frequencies) lid on top of the cone aperture, and exhaust from the evaporating  $\text{LN}_2$  will be directed inside the cone to maintain a pressure higher than that of the lab so that air will not enter the cone. Preliminary tests of the modified design will have to be made to verify performance.

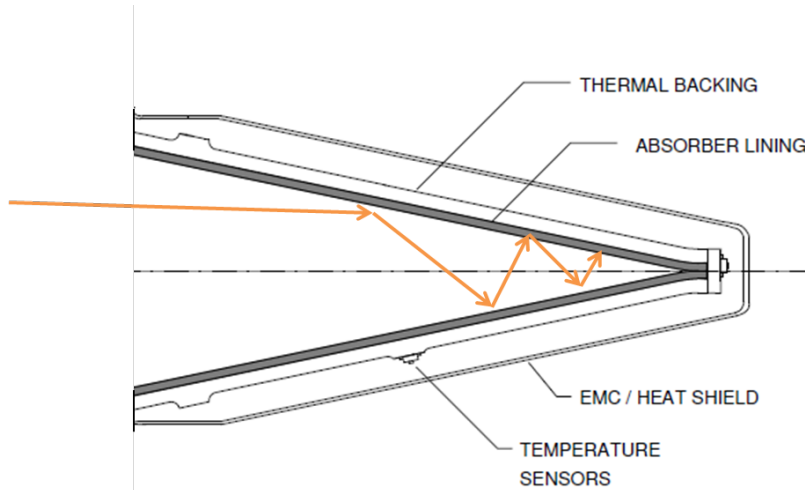


**Figure 3.8** Labelled drawing of the ambient conical calibration target. The carbon-loaded polymer absorber is shown in shaded grey. Multiple reflections and absorptions of radiation (orange arrows) give rise to low coherent reflections that are responsible for standing waves between the target and the receiver. Drawings modified from those obtained from TK.

### 3.2.4 Internal reference beam

In order to make the balanced measurements described in Section 2.3.4, a reference beam is needed as well as the signal beam from the atmosphere. An often-used technique involves another beam in the sky as the reference, usually aimed close to zenith and with a lossy absorber in the beam path to match the brightness temperature to that of the signal, [e.g. Parrish et al., 1988; Straub et al., 2010] for example. This technique has the unwanted effect that some of the spectral line signature from the target gas is contained in the reference beam measurement. This effect must then be accounted for in the calibration of the balanced spectrum. SPÉIR makes use of an internal reference beam created by blending together the signals from the hot and cold calibration targets using the rotatable polarising wire grid [Berg, 1998]. The advantage of this technique is that the reference beam does not contain any spectral line features, resulting in a higher contrast in the balanced spectra compared to using a reference beam from the atmosphere [Krupa et al., 1998].

With radiation from the cold target,  $T_c$ , being transmitted through the grid, and radiation from the hot,  $T_h$ , being reflected, the intensity of the polarised radiation that is coupled to the horn,  $T_{ref}$ , is given by Malus' law as

$$T_{ref} = T_h \cos^2 \beta + T_c \sin^2 \beta, \quad (3.1)$$

where  $\beta$  is the angle of the grid wires with respect to the horns polarization angle. The grid is not oriented parallel to the cross-section of the beams and so  $\beta$  is the angle that the beams “see”. The hot target in SPÉIR is oriented so that it sees the same  $\beta$  as the cold. For a grid oriented at an angle  $\theta$  with respect to the cross-section of the beam,  $\beta$  is related to the actual rotation of the wires,  $\varphi$ , by

$$\tan \varphi = \frac{\tan \beta}{\cos \theta}. \quad (3.2)$$

Solving for the power reaching the horn gives

$$T_{ref} = (1 + \cos^2 \theta \tan^2 \varphi)^{-1} (T_c + T_h \tan^2 \varphi \cos^2 \theta). \quad (3.3)$$

The function (3.3), plotted in Figure 3.9 for  $\theta = 20^\circ$ , is used to determine the polarizer angle,  $\varphi$ , needed to produce a reference beam with a brightness temperature equal to a signal beam.

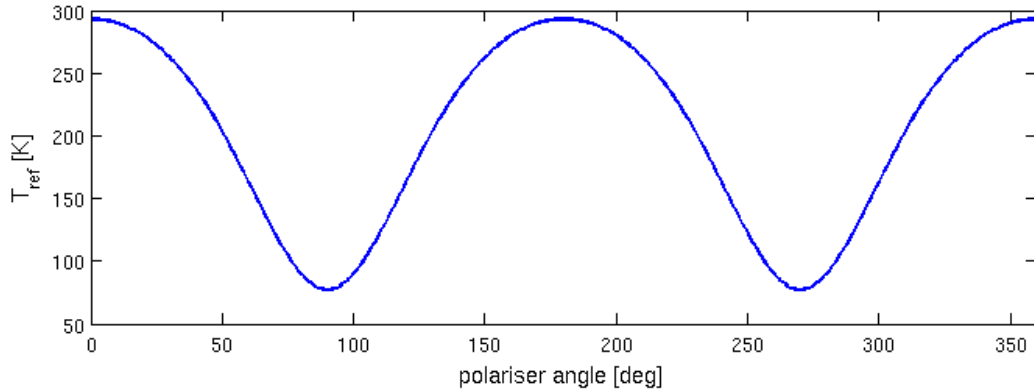


**Figure 3.9** Intensity of the internal reference beam used for a balanced measurement with SPÉIR, as a function of the polarizer angle (with respect to the polarization angle of the horn).

### 3.3 Back-end

#### 3.3.1 SIS mixer-preamplifier

The detector in SPÉIR is a superconductor-insulator-superconductor (SIS) mixer. In a cooled superconductor, a gap in energy,  $E_{\text{gap}}$ , is formed in the electronic density of states (there is an energy level about the Fermi energy in which there are no electrons (or quasiparticles)). For a ground-state superconductor, this sets up upper and lower bands which behave respectively like the conduction and valence bands in an intrinsic semiconductor [Wengler, 1992]. An SIS junction consists of two superconducting plates separated by a thin layer of insulating material. When operating as a detector, electrons can tunnel across the junction when one plate is struck by a photon with energy greater than  $E_{\text{gap}}$ , in a process known as photon-assisted quantum tunneling. A DC bias voltage,  $V_0$ , is applied across the junction so that the required energy of the photon is less than  $E_{\text{gap}}$  and corresponds to the frequency of radiation being observed. An illustration of an SIS tunnel junction is shown in Figure 3.10. The SIS displays strong non-linearity in its IV (current and voltage, respectively) characteristics when operated like this and so can be used as a highly sensitive mixer (see Section 2.3.1) with a theoretical noise as low as the quantum limit.

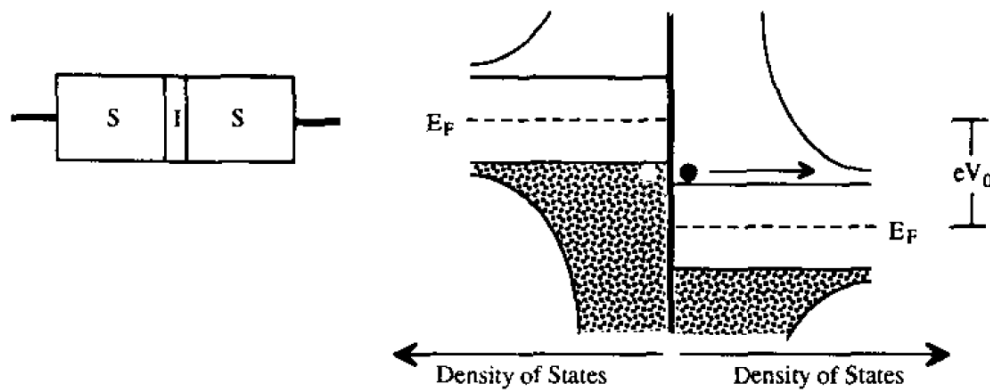


**Figure 3.10** Left: An SIS tunnel junction is a diode made of two superconductors separated by a very thin insulator. Right: The electronic density of states for an SIS with a dc bias voltage,  $V_0$ , providing an energy just larger than  $E_{\text{gap}}$ . An electron (quasiparticle) tunnels from left to right, adding to the current through the SIS. Diagram from [Wengler, 1992] © 1992 IEEE.

The sideband-separating (see Section 2.3.2) SIS mixer for SPÉIR was developed by the National Radio Astronomy Observatory and is already in use for the Atacama Large Millimeter Array (ALMA), an international astronomical project underway in Atacama, Chile. The detector junction is Nb/Al-AlOx/Nb and is designed for operation between 211 and 275 GHz, but measurements show good operation as high as 282 GHz [Kerr et al., 2004], which is needed by SPÉIR to measure ClO at 278.63 GHz. A schematic of the mixer block is shown in Figure 2.4, including the IF preamps and IF hybrid. The preamps, which are cooled to 4 K, cover an IF range of 4 – 12 GHz, with a noise temperature of 4 – 8 K and 30 dB of gain. Single sideband (SSB) noise temperatures below 60 K have been measured over the operating frequency range of SPÉIR (265 – 280 GHz) [Kerr et al., 2004].

### 3.3.2 Sideband separation and spectrum analysis

After the atmospheric (RF) signal is down-converted and amplified by the SIS mixer-preamp, the IF signal is put through a bandpass filter and is downconverted again to a second IF centred on  $\sim 1$  GHz, before being analyzed by a Fast Fourier Transform Spectrometer (FFTS). When removing the unwanted sideband in a signal, either the suppression should be so good that the effect of the sideband can be neglected, or the level of suppression should be accurately known so that it can be accounted for (in the inversion process, for example). For the former, this is commonly done using a quasioptical device such as a Martin-Pupplett interferometer which effectively filters out the unwanted sideband. This method has its problems as the interferometer can set up optical cavities within the system. The latter situation is common when using a sideband separating mixer, as in SPÉIR, and an accurate knowledge of the suppression requires that periodic measurements be made of it, because it may change over time. It was decided, in the design of SPÉIR, to have the option of including a Martin-Pupplett interferometer in the quasioptical setup (with some rearrangement of the optics), and to make use of recent advancements in technology that allow the enhancement of the sideband separation from the SIS mixer.

Section 2.3.2 describes how sideband separation is achieved in the mixer. The IF hybrid combines the two IF outputs of the mixer block with relative  $90^\circ$  degree phase shifts to achieve isolation of the upper and lower sidebands. The solution assumes that the mixer is symmetric and

that there are no phase or amplitude errors i.e. perfect sideband separation. In practice the mixer is not perfectly symmetric (errors in the RF side), and the IF hybrid introduces imperfect phase difference (errors on the IF side), and so there will be a limited suppression of the unwanted sideband. The sideband suppression of the SIS mixer-preamp for SPÉIR has been measured at approximately 20 dB [Kerr, 2004], and between 10 and 20 dB when integrated into the ALMA Band 6 instrument [Ediss, 2004].

Improvement on the sideband suppression mentioned above can be achieved by combining the SIS mixer-preamp with an In-Phase Quadrature-correlator (IQ-correlator) spectrometer: The Correlation and Spectrum Analysis Core (COSPAN) firmware has been developed at the University of Bern and the University of Applied Sciences Northwestern Switzerland, and it runs on commercially available hardware [Murk et al., 2009]. The system analyses the power spectrum of the signal just as a conventional FFTS, and also allows separation of the two sidebands by digital signal processing instead of using the IF hybrid: Equation (2.41) and (2.42) give the IF output at the two preamplifiers for an ideal mixer, rewritten here as  $x(t)$  and  $y(t)$  respectively:

$$x(t) = aV_{if} \left[ \mu_{rf}\mu_{if}e^{i(\omega_{if}t)} + \mu'_{rf}\mu'_{if}e^{-i(\omega_{if}t)} \right], \quad (3.4)$$

$$y(t) = aV_{if} \left[ \mu_{rf}\mu_{if}e^{i(\omega_{if}t-\pi/2)} + \mu'_{rf}\mu'_{if}e^{-i(\omega_{if}t-\frac{\pi}{2})} \right], \quad (3.5)$$

With COSPAN the two complex FFT spectra of these outputs,  $X(t)$  and  $Y(t)$ , are combined with a virtual  $\pm 90^\circ$  phase shift that corresponds to a digital version of the IF hybrid in Figure 2.4. The corresponding outputs of the upper and lower sidebands in the time domain are:

$$LSB = 2aV_{if}e^{-i\omega_{if}t}, \quad (3.6)$$

$$USB = 2aV_{if}e^{i\omega_{if}t}. \quad (3.7)$$

The operation mode is referred to IQ90. This and the other operation modes, Total Power and Correlation, are listed in Table 3.1 along with their outputs,  $C1$  and  $C2$ . Phase matched cables are used to transfer the IF output from the mixer block to the spectrometer. The advantage of using the IQ-correlator spectrometer is that the balance of the phase difference, which limits

the image suppression, can be determined as  $\phi = \arctan(C1/C2)$  using the Correlation mode. In an ideal system  $\phi = \pm 90^\circ$ . A phase shift introduced at the second down-conversion stage can be used to optimize the image suppression. Similarly, amplitude balance can be calculated as  $C1/C2$  for Total Power mode, which is ideally 0 dB for a balanced system, and the amplitude balance can be adjusted by changing the reference voltage of the Analogue to Digital Converters (ADCs) that are part of the system [Murk et al., 2009]. An electronic automation of these procedures to optimize the sideband suppression on the fly is an advantage for SPÉIR as it will be operating in a remote Arctic location.

	<i>c1</i>	<i>c2</i>
<b>Total power</b>	$ X ^2$	$ Y ^2$
<b>Correlation</b>	$\text{Re}(X^* \cdot Y)$	$\text{Im}(X^* \cdot Y)$
<b>IQ90</b>	$ X + jY ^2$	$ X - jY ^2$

**Table 3.1** Operation modes of the digital correlator using COSPAN firmware

### 3.3.3 Cryogenic cooling and cryostat

Cooling a mixer generally reduces the thermal noise that is produced by it, and so reduces the system temperature (see Equation (2.49)). In the case of an SIS mixer, cooling is also needed in order to reach a temperature below which the metal begins superconducting. In the case of niobium this is 9.3 K. The Nb/AlO<sub>x</sub>/Nb SIS mixer is designed to operate at 4.2 K for ALMA and will be cooled to  $\sim 4$  K for SPÉIR. Figure 3.11 and Figure 3.12 show CAD drawings of the cryocooler and the cryostat designed for SPÉIR. There are three temperature stages: ambient, 60 K, and 4K. The SIS mixer block and the magnet for suppressing Josephson current are contained within the 4 K stage along with the ultra-Gaussian horns for the atmosphere/reference signal and LO signal. The figures also show the IF hybrid fixed to the 4 K plate. The stage is designed to hold it in case the want should arise. The SIS mixer block is also fixed to the 4 K plate. There are windows at each stage of the cryostat, as it is under vacuum, to allow the signals to reach

the 4 K stage. They are angled at 5° with respect to the horn aperture to minimize coherent reflections. At the LO entrance, the first window is a lens which focuses the LO beam at the horn. The lens is not angled and so is blazed to minimize coherent reflections. A connector on the outer vacuum chamber (OVC) provides wiring access to the interior of the cryostat. Two ribbon cables, each consisting of 24 pairs of phosphor-bronze wires, twisted in pairs, travel from the OVC to the SIS mixer-preamp and magnet in the 4 K stage. The bias wires to the mixer and preamplifier pass through a protection circuit attached to the inside of the OVC to reduce the risk of electrostatic discharge reaching and damaging the mixer-preamps. The whole optical bench is placed on an electrostatic discharge mat for the same reason, and any interaction with the table should be only be made while wearing a grounded bracelet. Phase-matched coaxial cables lead the two IF outputs from the mixer-preamps to the connection on the OVC. These connections transfers the IF signal that will be processed and analysed via the FFTS to produce an atmospheric spectrum, as described in previous sections.

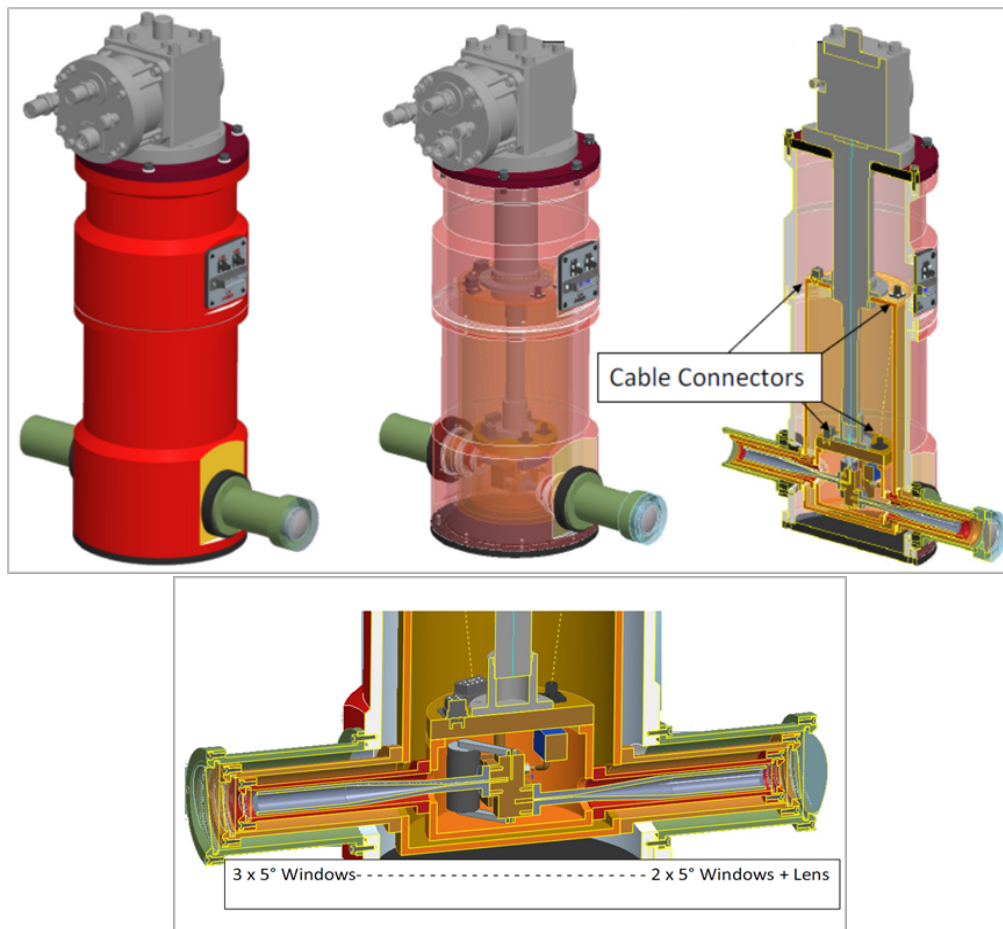


**Figure 3.11** Upper: 3D CAD drawings of the cryostat setup for SPÉIR showing ordinary, transparent, and cross-sectional views. Lower: rotated close-up of the cross-section. Drawings by Stuart Froud at TK.

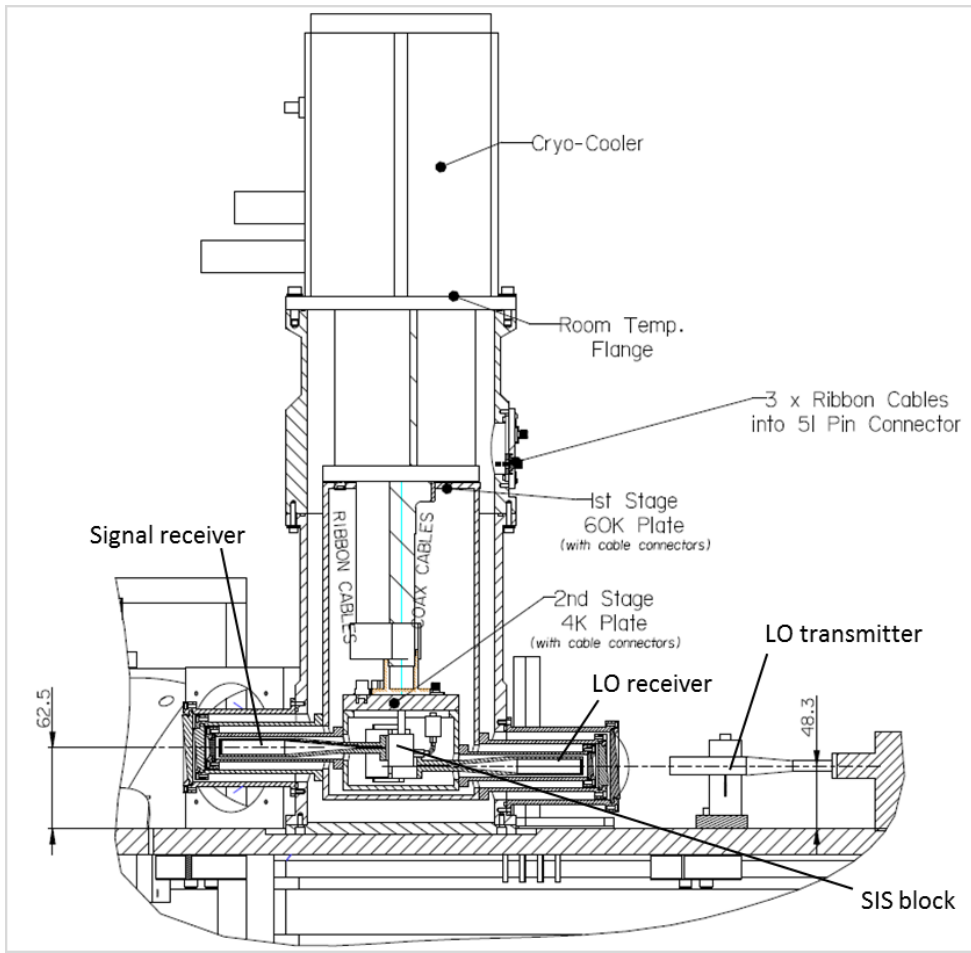


**Figure 3.12** CAD drawing showing a cross-section of the cryostat for SPÉIR. Labels indicate the three temperature stages, the components within the 4 K stage, and ribbon/coaxial cable placement. Drawing by Stuart Froud at TK.

### 3.4 Conclusion

A new ground-based instrument has been designed for the goal of observing trace gases related to ozone chemistry in the High-Arctic stratosphere. In particular, the aim is to have the first instrument that is capable of making continuous measurements of ClO in the Canadian Arctic. SPÉIR is designed for optimal operation in the frequency range of 265 – 280 GHz, which contains signatures from rotational transitions of O<sub>3</sub>, N<sub>2</sub>O, HNO<sub>3</sub>, and ClO. A relatively simple quasioptical setup provides minimal deformation of the fundamental Gaussian beam, and a high gain system (41.07 dB) corresponding to a half-power beamwidth of 0.9° giving a horizontal resolution on the sky of approximately 2.5 km at 30 km altitude. Ultra-Gaussian horns, blackbody reference loads with low coherent reflections, a path length modulator, tilted cryostat windows, and the omission of quasioptical sideband suppression are used to minimize poten-

tial standing waves in the system. A very low noise (<60 K), sideband separating SIS mixer is used as the detector. An IQ-correlator spectrometer is used to analyse and transform the signal into the spectral domain, as an FFTS, and also provides enhanced suppression of the unwanted sideband, which can be made autonomous.

# Chapter 4

---

## 4 Observation system characterization and simulation experiments

Much of the work described in this chapter was done concurrently with the design of SPÉIR. The goal was to determine the feasibility of the measurement technique, to guide the instrument design, and to set requirements on the knowledge of forward model parameters. The results of the study show the capability and limitations of the observation system, and also that the retrieved data from instruments operating in this frequency range must be treated carefully when they are used for generating climatologies or trends of gas concentration. Despite the motivation for the work and the drive to show the capability of this type of observation system operating in the Arctic, the discussion is kept general where possible, as the techniques and some of the results are applicable to other ground-based instruments. A large portion of this chapter has been published in [Ryan and Walker, 2015].

### 4.1 Forward and inverse models

The forward model used for calculations of the radiative transfer through the atmosphere, is the Atmospheric Radiative Transfer Simulator (ARTS) [Buehler et al., 2004], developed jointly by the University of Bremen and Chalmers University of Technology. ARTS is a publically available radiative transfer model designed for the millimeter and sub-millimeter spectral range. The model has a modular design and emphasis is placed on extendibility and generality. The model assumes a one-dimensional spherical atmosphere: the atmospheric parameters vary as a function of altitude only. The model can be used to simulate measurements in any viewing geometry: upward, downward, or limb viewing, and for any position of the sensor: on the ground, and above or inside the atmosphere. The calculations work with arbitrary frequency grids so it can be used to model broad ranges of the spectrum or high-resolution sensors. ARTS explicitly calculates the absorption coefficients (Section 2.2.2) at each frequency by determin-

ing the contribution from each spectral line entered as input, and performs line-by-line calculations and integration of the radiative transfer equation (Equation (2.27)). ARTS also calculates the necessary Jacobians either analytically or by perturbation.

The inversion is done using package Qpack [Eriksson et al., 2005] which uses the Optimal Estimation Method (see Section 2.4.2). Qpack is designed specifically to work with ARTS and acts as a shell around it, so one can perform forward modelling and retrieval work. Qpack allows modelling of the instrument characteristics through sensor response matrices (see Section 2.4.2) of the antenna, mixer and sideband treatment, and spectrometer.

### 4.2 Instrument and inversion setup

The generality of ARTS and Qpack means that they can be used as part of a wide variety of observation systems. This means that an inversion scheme must be created and optimized for the particular system of which it will be a part. Information about SPÉIR, the Eureka observation site, the observation technique, and forward model parameters, must be developed in order to be used as input to the ARTS and Qpack models. Inversion schemes were created and optimized to retrieve information about the four target species for SPÉIR. Each scheme varied according to the characteristics of the species and the choices of observation technique. The main points of the inversion setup are detailed here.

A nonlinear inversion scheme is used for the retrievals in all of the simulation experiments in this chapter, except for some linear inversions included in Section 4.3.5. It is assumed that a nonlinear inversion is required to retrieve atmospheric concentrations using SPÉIR, and this assumption is validated in Section 4.3.5. For a nonlinear inversion, a Marquardt-Levenberg iterative minimization method [Marquardt, 1963] is used with Qpack. This method included the same convergence criteria for each target species: convergence is achieved when a change in the state vector, from one iteration to the next, is less than 1% of the retrieval precision. The parameters used for the Marquardt-Levenberg method, which describe the interpolation between fitting via Gauss-Newton and the method of gradient descent, were chosen on a trial and error basis for each species to give a maximum in the number of converged profiles.

## 4. Observation system characterization and simulation experiments

---

For inversions of total power measurements, an offset in the absorption coefficients is retrieved to account for attenuation of the signal by the troposphere. This is done by including the H<sub>2</sub>O continuum in the state vector. The retrieved water vapor VMR serves as a parameterization for the offset in absorption coefficient [Buehler, 2002]. It was found that many iterations of the minimization method were needed to achieve convergence when retrieving the H<sub>2</sub>O continuum. A polynomial is also included in the state vector. A polynomial is fitted to the baseline to remove artifacts in the spectra that are not part of the atmospheric signal, e.g., standing wave signals. In this work, a polynomial fit is included here in the inversions of spectra made with the reference beam technique, in order to correct for a difference in the reference beam and continuum [Straub et al., 2011].

The a priori VMRs used for inversions are based on climatological gas concentration profiles developed for Eureka [Lindenmaier, 2012]. The VMRs for each of the target gases and for H<sub>2</sub>O are shown in Figure 4.1. The uncertainty in the a priori VMRs is fixed to 50% at each altitude. The natural variability of each species changes depending on the time of the day and season and the uncertainties in the a priori state will change accordingly. An uncertainty (one standard deviation) of 50% is representative of natural variability of each gas at Eureka. The climatologies for Eureka have the same uncertainty at each altitude for a given gas, with the exception of O<sub>3</sub>. For O<sub>3</sub>, the uncertainty varies between ~ 40-60 % in the stratosphere and has a maximum of 75% around the tropopause. It was decided to use a fixed uncertainty of 50% at each altitude for O<sub>3</sub>. This is a reasonable assumption for the stratosphere, as a seasonally varying a priori will be used for operational retrievals, and it simplifies the analysis of the observation system simulations. The correlation length for each gas describes the correlations between gas concentrations at different altitudes of the atmosphere and describes the off-diagonal entries of  $\mathbf{S}_a$  (Section 2.4.2). A Gaussian correlation between layers is used for each retrieved species with a correlation length of 4.5 km. The correlation length for each gas will also vary diurnally/seasonally and the value chosen here is within those based on the Eureka climatologies for each gas.

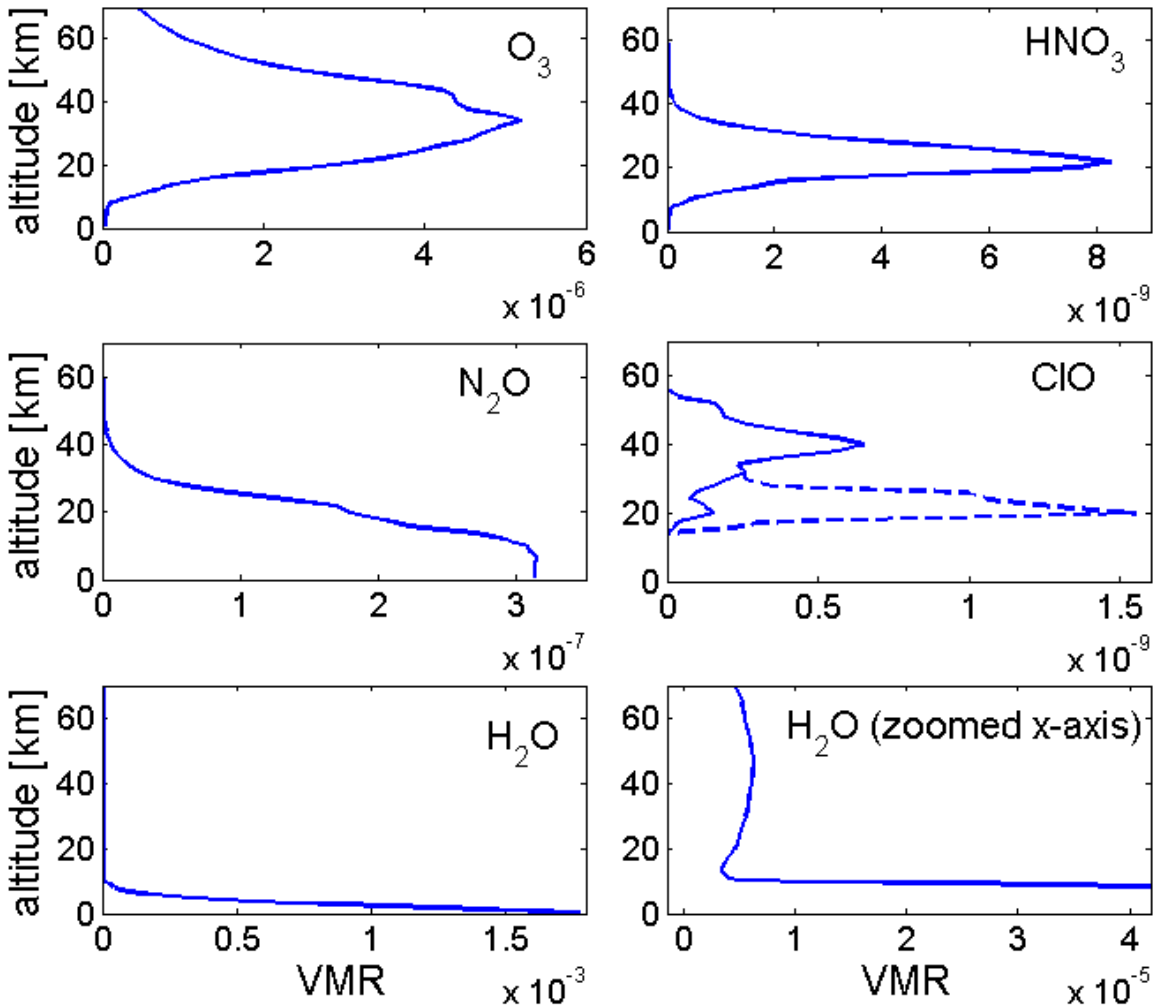


**Figure 4.1** Climatological gas concentration profiles for Eureka for O<sub>3</sub>, HNO<sub>3</sub>, N<sub>2</sub>O, ClO, and H<sub>2</sub>O. ClO\* represents enhanced ClO levels that can be observed in polar spring in the presence of PSCs.

Table 4.1 lists the center frequencies of the 1 GHz observation bands for each target species as well as the retrieved and background interfering species in each window. Background interfering species are species which are included in the forward model calculations but are not retrieved in the inversion because of low signal-to-noise ratios (SNRs). They are included in the forward model calculations to improve the fit to the spectrum. Retrieved background species are those which have a high enough SNR to be retrieved alongside the target gas. The spectroscopic parameters used in the forward model are taken from the High Resolution Transmission (HITRAN) molecular absorption database 2008 [Rothman et al., 2009] and the Jet Propul-

## 4. Observation system characterization and simulation experiments

---

sion Laboratory (JPL) catalogue [Pickett et al., 2001], and the continuum model used is the Millimeter-wave Propagation Model, MPM93 [Liebe et al., 1993]. In previous assessments, MPM93 has been shown to describe physical reality very well [Buehler, 2002].

For some simulations, a concentration profile for ClO was used which represents enhanced ClO concentrations (denoted as ClO\*). This concentration profile corresponds to situations when polar stratospheric clouds, which alter the chemistry in the atmosphere, are present in the lower stratosphere inside the polar vortex [Peter, 1997]. The peak VMR in the a priori ClO\* profile, at approximately 19 km, is  $\sim 1360$  ppt compared to  $\sim 136$  ppt for the non-enhanced ClO VMR profile. This increase is consistent with satellite observations of Arctic ClO by the Microwave Limb Sounder (MLS) on the Aura satellite [Manney et al, 2011].

The temperature and pressure profiles used in the inversions are from radiosonde measurements made at Eureka supplemented with the National Centers for Environmental Prediction (NCEP) profiles above the maximum altitudes of the radiosondes, and with the 1976 U.S Standard Atmosphere profile above 50 km [Batchelor et al., 2009]. Uncertainties in the temperature profiles are determined from uncertainties quoted in the NCEP profiles: 2 K below 30 km, 5 K between 30 and 35 km, 6 K between 35 and 40 km, 7 K between 40 and 50 km, and 9 K above. No correlation is assumed between altitude layers. The radiosonde instruments quote an uncertainty of 0.5 K [Luers, 1997] but this is an underestimation as the temperature/pressure measurements are only made twice-daily. The pressure grid used for forward model calculations is a 61-layer pressure grid covering altitudes between 0 and 100 km in altitude. The retrieval grid used is a 49-layer pressure grid between 0 and 90 km in altitude and corresponds to an approximately equal spacing in altitude between retrieval grid-points. The integration time needed to achieve a desired SNR can be calculated with the radiometric equation (Equation (2.53)). The integration time required is dependent on the atmospheric conditions which govern the opacity of the atmosphere during a measurement. The values taken to be the measurement noise on the spectrum,  $\Delta T$ , used for the target species are listed in Table 4.1. There is no correlation assumed between each frequency channel and so  $\mathbf{S}_e$  is a diagonal matrix with the non-zero entries given by  $(\Delta T)^2$ . Using the climatology for Eureka, the estimated values for the measurement noise here correspond to an average integration time on the order of minutes for O<sub>3</sub> and up to hours for ClO, assuming clear sky conditions. No binning was

## 4. Observation system characterization and simulation experiments

---

applied to any part of the spectra that were inverted. An uncertainty of 0.5 K was used for the physical temperature of the calibration targets [Murk et al., 2008] and a 0.5° uncertainty in the observation angle was estimated based on the selected motor specifications. For HNO<sub>3</sub> and ClO spectra, an uncertainty of 7% in the tropospheric correction factor (Section 2.3.4) is assumed. This uncertainty is quoted for an operating ground-based instrument using a similar technique [Straub et al., 2010]. Errors due to uncertainties in the intensity, air broadening parameter, and air broadening temperature coefficient, of molecules of all species listed in the spectral line catalogues are considered. A detailed description of the uncertainties in spectral lines between 250 and 300 GHz, and their associated errors on O<sub>3</sub>, N<sub>2</sub>O, HNO<sub>3</sub>, and ClO is discussed in Chapter 5. A third order polynomial was used in inversions including a polynomial fit. This should be sufficient to fit standing wave signatures originating from reflections from the cryostat windows as they will have a relatively long baseline pattern. While it is possible to remove standing waves caused by optical cavities in the beam's path through changes to the quasioptical setup or other instrument hardware, it is expected to be the most difficult/expensive/annoying to do this for reflections from the windows as they are a fixture of the cryostat.

Section 3.3.2 describes the optimal setup of SPÉIR operating in Sideband Separating mode (2SB). The studies are done here by inverting a single sideband at a time with a known suppression of the unwanted sideband of 20dB. The presented results apply similarly to the different operation modes except that the observation of two target gases can potentially be done simultaneously using a 2SB.

## 4. Observation system characterization and simulation experiments

---

Center frequency	Target species	Retrieved interfering species	Background interfering species	$\Delta T$	Measurement method
269.400 GHz	$\text{HNO}_3$	$\text{O}_3$	$\text{H}_2\text{O}, \text{N}_2\text{O}, \text{OCS}, \text{SO}_2, \text{NO}_2$	0.01 K	Balanced
273.015 GHz	$\text{O}_3$	$\text{H}_2\text{O}$ continuum	$\text{H}_2\text{O}, \text{N}_2\text{O}, \text{HNO}_3$	0.02 K	Total power
276.301 GHz	$\text{N}_2\text{O}$	$\text{O}_3, \text{H}_2\text{O}$ continuum	$\text{H}_2\text{O}, \text{HNO}_3, \text{OCS}, \text{SO}_2, \text{NO}_2, \text{H}_2\text{CO}$	0.01 K	Total power
278.630 GHz	$\text{ClO}$	$\text{O}_3$	$\text{H}_2\text{O}, \text{N}_2\text{O}, \text{HNO}_3, \text{OCS}, \text{SO}_2, \text{NO}_2$	0.005 K	Balanced

**Table 4.1** The center frequencies of the four 1 GHz bands for the target species, and the retrieved and background interfering species in each band. The frequency resolution in each band is 1 MHz. The measurement noise on the spectrum,  $\Delta T$ , taken for each species is also given. A description of the measurement methods is given in Section 2.3.4.

## 4.3 Results

This section outlines the main results of the observation system characterization and the observation system simulation experiments (OSSEs). Section 4.3.1 shows an example of the forward modeling of the radiative transfer through the atmosphere and discusses the choice of the  $\text{O}_3$ ,  $\text{N}_2\text{O}$ ,  $\text{HNO}_3$ , and  $\text{ClO}$  spectral lines to observe in the 265 – 280 GHz region. Section 4.3.2 defines the altitude ranges over which each target species can be detected, the altitude ranges over which concentration retrievals can be made, and the altitude resolution of those retrievals. Section 4.3.3 discusses the error contributions to the retrieved state from instrument and model parameters (found using the OEM). Section 4.3.4 compares the OEM characterization to results of multiple inversions of simulated data. Section 4.3.5 looks at nonlinearity in the system and explains some biases in the retrieved concentration profiles found in Section 4.3.4 that are relevant to using data for a climatology or trend analysis.

### 4.3.1 Simulated observations above Eureka

In a first step, ARTS was used to model the atmosphere above Eureka in the spectral region targeted with SPÉIR. The inputs are those outlined in Section 4.2 but without any instrumental effects or measurement noise added to the calculated spectra. Figure 4.2 shows the intensities

## 4. Observation system characterization and simulation experiments

---

of the dominant molecular transitions within each chosen frequency range and the corresponding simulated spectrum (in units of brightness temperature) that would be observed from PEARL. One can see that while the strength of the ozone transition at 273 GHz is not as great, per molecule, as that from other gases, the intensity of the spectral line is much larger ( $\sim 20$  K) by comparison due the abundance of  $O_3$  in the stratosphere. In a similar way, despite the strength and number of ClO transitions at 278.6 GHz, the spectral line intensity is small ( $\sim 0.1$  K) because of the low atmospheric concentration of ClO. The low concentration of ClO makes it difficult to measure from the ground. The  $HNO_3$  and  $N_2O$  spectral lines have intensities on the order of 1 K. It was decided to use the balanced technique for  $HNO_3$  as the number of rotational transitions gives rise to a spectral feature that will more be difficult to differentiate from baseline artifacts.

These spectral windows were chosen because of the clear signals from each target species: the windows are close together in frequency space (all within the optimal operating frequency range of SPÉIR) and contain few interfering signals from other gases in the atmosphere. The quasi frequency-independent baseline of the spectrum at approximately 80 K is the signal from the continuum (see Section 2.2.2.2).

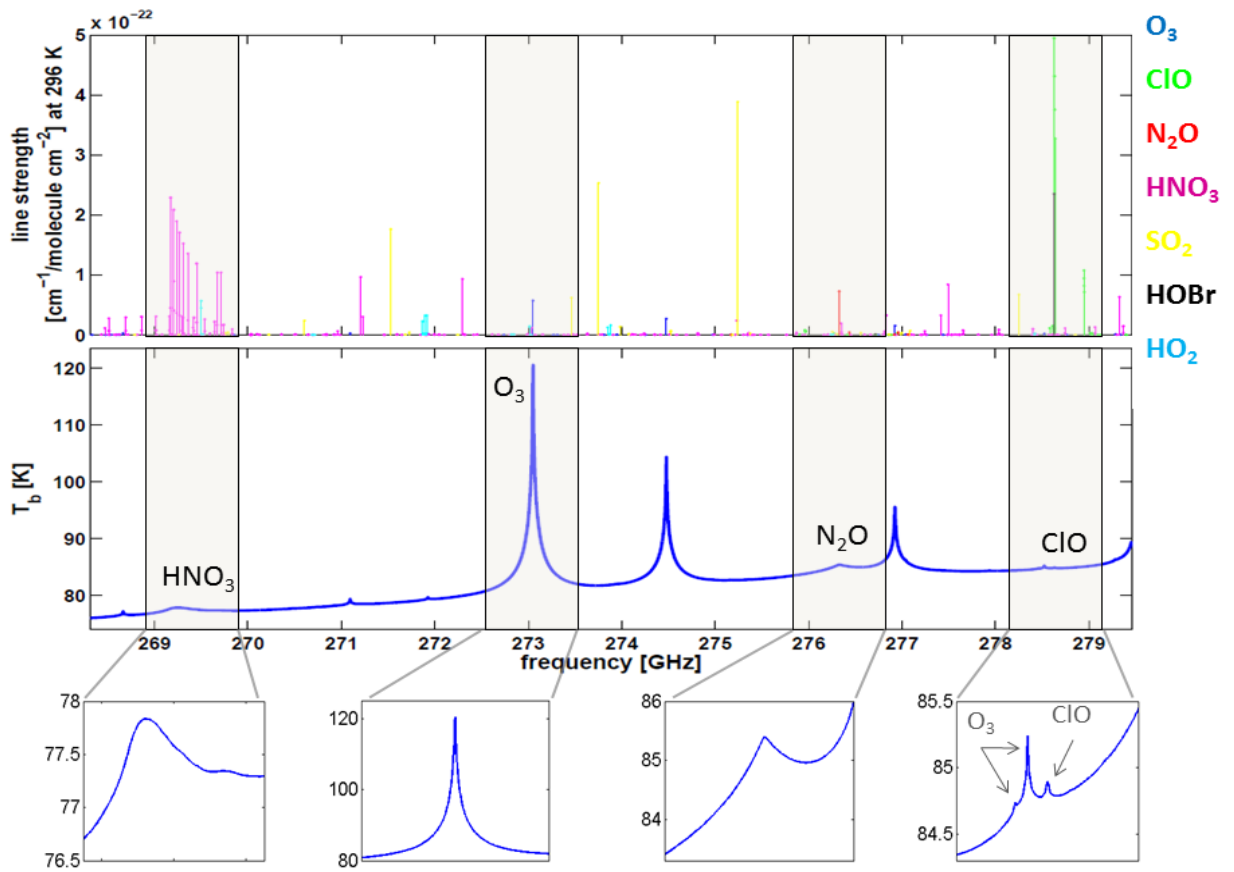


**Figure 4.2** Upper: line strengths of the dominant molecular rotation transitions in the frequency range 268 – 280 GHz. Middle: the corresponding emission spectrum simulated above Eureka. A daily temperature profile representative of March, and Eureka VMR climatologies were used in the simulation. The shaded ranges show the 1 GHz frequency bands proposed to be used for atmospheric observations with SPÉIR. Blow-ups of each target line are also shown in the lower panels.

### 4.3.2 Detection, and retrieval altitude limits and altitude resolution

A measure of the detectability of a trace species in the atmosphere that depends on the atmospheric conditions and capability of the instrument, but does not depend on the inversion approach, was used to evaluate the detection limits for each gas. The noise-equivalent volume mixing ratio (NVMR) describes the minimum variation in the VMR of a gas that would cause a brightness temperature difference in the measured spectrum that is larger than the noise on the measurement [Buehler, 1999]. The calculation of the NVMR uses the matrix  $\mathbf{K}$ , defined in Section 2.4.2, to find the change in the intensity of the spectral line caused by a change in the VMR of a gas at each retrieval altitude grid-point. If the a priori VMR at a grid-point gives a spectral signal larger than the noise on the spectrum, the gas is considered detectable at that

## 4. Observation system characterization and simulation experiments

---

altitude. The NVMR was calculated accounting for the fact that an optimal number of spectrometer channels may be binned to achieve the best SNR at each retrieval grid-point. The upper and lower altitude detection limits for each gas are shown in Figure 4.3. It is interesting to note that O<sub>3</sub>, N<sub>2</sub>O, and HNO<sub>3</sub> are detectable down to 610 m (the elevation of the measurement site) but this result is misleading: At these low altitudes, the optimal binning of spectrometer channels required the full 1-GHz band, leaving only a single brightness temperature value for the measurement. One cannot separate the contribution from the target gas and the continuum, and the NVMR gives an unrealistic estimate of the lower detection limit.

The retrieval is considered not to contain enough information from the measurement when the measurement response decreases below a certain value. This value is subjective as a definition of the retrieval limit and a retrieved VMR profile should always be accompanied with the averaging kernel matrix. Nonetheless it is useful to define a retrieval limit for the capability of an observing system and here a cut-off of 0.8 for the measurement response has been used to define the retrieval ranges for species observable by SPÉIR. The measurement responses are plotted in Figure 4.4 along with the columns of the averaging kernel matrix for each species. The altitudes where the measurement response decreases below 0.8 define the upper and lower retrieval limits for a gas. The resulting altitude range is that within which a retrieval is expected, defined by the relative contribution of the measurement and the a priori to the retrieved state. The choice of measurement response cut-off is somewhat arbitrary. 0.8 is used here as it limits a reasonable amount of a priori contribution and has been used for several similar ground-based instruments e.g. [Hoffmann et al., 2011; Straub et al., 2011; Struder et al., 2013].

The retrieval of ClO and HNO<sub>3</sub> includes a polynomial fit to the baseline of the spectrum because of the balanced measurement method described in Section 2.3.4. Some of the atmospheric signal in the spectrum that is associated with emissions from lower altitudes can be then attributed to the baseline by the polynomial fit. This means that some of the lowest altitude information is lost in an inversion when a fit to the baseline is included. It was found that applying a polynomial baseline fit to O<sub>3</sub> and N<sub>2</sub>O spectra meant that the lowest retrieved altitudes for O<sub>3</sub> and N<sub>2</sub>O were ~7 km higher than the corresponding lowest retrieved altitudes for an inversion that did not include a polynomial baseline fit. It is assumed that a fit to the baseline will be

## 4. Observation system characterization and simulation experiments

---

needed for all measured spectra and so the estimated retrieval ranges for SPÉIR are those for the inversion that includes a polynomial in the state vector. The results are comparable with the ranges determined for the SIS instrument, RAMAS, for operation at Summit, Greenland [Golchert et al., 2005]. The retrieval ranges for each species are shown in Figure 4.3. The lowest retrieved altitude for ClO shifts from  $\sim 18.0$  km to  $\sim 16.2$  km for the enhanced ClO scenario, ClO\*. Similarly, the lowest detection altitude decreases from approximately 13.5 km to 9.5 km. Both the highest retrieved and highest detection altitude are slightly decreased for a ClO\* scenario. This is because the enhanced concentration of ClO at  $\sim 19$  km attenuates the emission signal from ClO situated higher in the atmosphere.

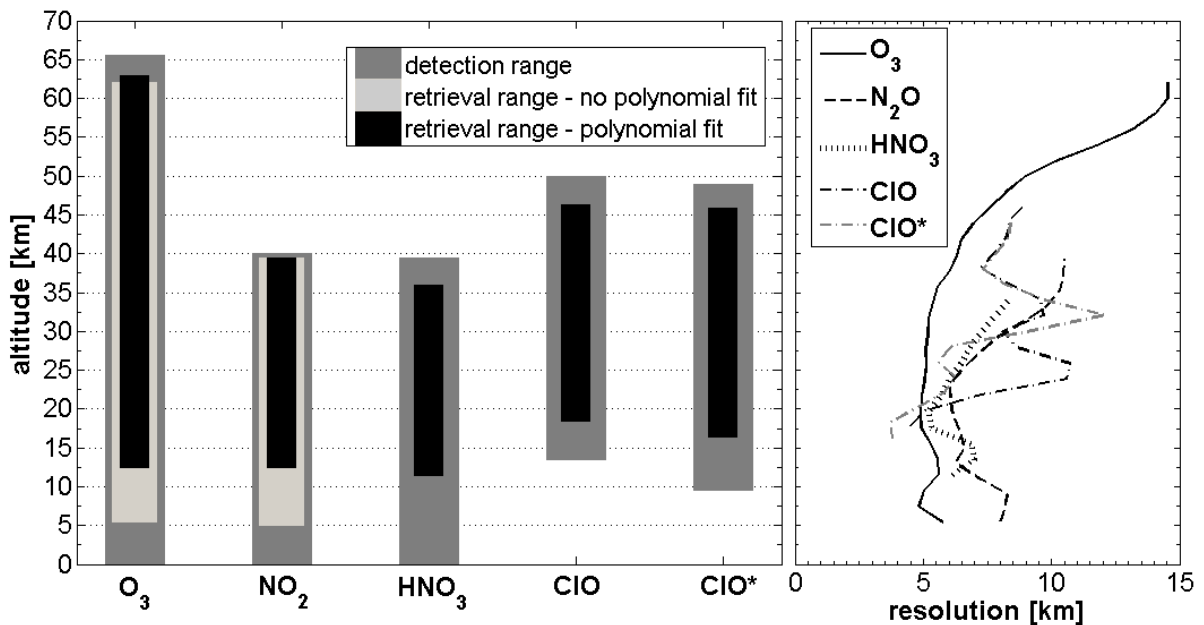


**Figure 4.3** Left: the retrieval altitude and detection altitude ranges for each species including ClO\* (ClO when enhanced in polar spring). Right: the altitude resolution of the retrieval of each species derived from the FWHM of the averaging kernels.

There are several ways to define the altitude resolution of a retrieval. The most accurate representation is obtained from the singular vectors of the averaging kernel matrix,  $\mathbf{A}$ , which describe the scales of the VMR vs. altitude features that are best resolved by the inversion [Rodgers, 1990; Hansen, 1992], given in order of decreasing singular value. As the singular vector representation is not very intuitive, other less exact representations of the altitude resolution are more commonly used: one method uses the full-width-at-half-maximum (FWHM) of  $\mathbf{A}$ , (shown in Figure 4.4 for the SPÉIR target species). Drawbacks of this method are that the nega-

## 4. Observation system characterization and simulation experiments

---

tive values of  $\mathbf{A}$  are not accounted for and that the resolutions found are misleadingly small at low altitudes where the spectral line signal is low. Another method is to use the degrees of freedom for signal (DOFS) for the inversion. The DOFS is given by the trace of  $\mathbf{A}$  [Rodgers, 2000]. Because  $\mathbf{A}$  is a real symmetric positive-semidefinite matrix, the DOFS are equivalent to the sum of the magnitudes of the singular vectors of  $\mathbf{A}$ . Dividing the retrieved altitude range by the DOFS over the same range gives an altitude resolution of 5.6 km, 7.3 km, 6.5 km, and 5.5 km for  $\text{O}_3$ ,  $\text{ClO}$ ,  $\text{N}_2\text{O}$ , and  $\text{HNO}_3$  respectively, which are comparable to the FWHM of the averaging kernels in Figure 4.3. The DOFS increased by 1 for a scenario with enhanced  $\text{ClO}$  ( $\text{ClO}^*$ ). The extra information is related to the lower half of the retrievable altitude range and can be seen in the increased vertical resolution for  $\text{ClO}^*$  compared to  $\text{ClO}$  in Figure 4.3.

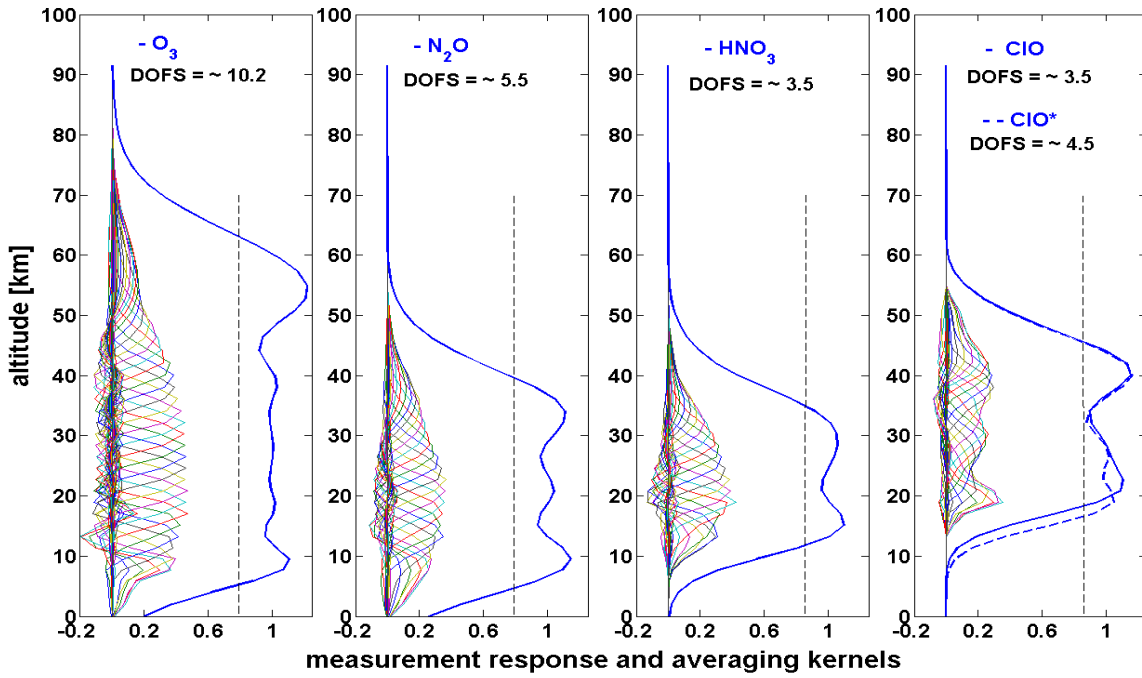


**Figure 4.4** The averaging kernels and measurement response (thick blue line) for each target species. The vertical dashed line at 0.8 marks the measurement response cut-off point for retrievable altitudes, as used in this work. The measurement response for an atmosphere with enhanced  $\text{ClO}$  ( $\text{ClO}^*$ ) is also shown. The degrees of freedom for signal (DOFS) for 0–90 km are listed for each species.

### 4.3.3 Instrument and model parameter uncertainties

The errors in the retrieved VMRs coming from instrumental uncertainties and from input to the forward model are shown in Figure 4.5. They were calculated using the OEM error definitions from Section 2.4.2 and the uncertainties in Section 4.2, except for the error due to the tropospheric correction, which was calculated explicitly by over- or under-correcting the balanced spectrum. Error due to uncertainties in the atmospheric temperature is < 3% at all altitudes for HNO<sub>3</sub> and N<sub>2</sub>O. This is similar for O<sub>3</sub> except in the troposphere where there is a peak in the error of ~4% at 8 km altitude. The error in retrieved ClO profiles shows a more complicated response to the uncertainties in atmospheric temperature, peaking at ~6% at 25 km altitude and 7% at 35 km. This peak decreases to < 3% for the ClO\* scenario but there is also an increase in the error below 20 km altitude. The error contribution from the pointing uncertainty, at a measurement angle of 25° elevation, is approximately 2% over all altitudes for all species except for ClO which has a peak of 5% at 20 km altitude. Simulations performed over a range of observation angles (for summer and winter conditions at Eureka) showed that 25° elevation gave the best SNR in the measured spectrum. While not contributing a large error to the retrieval itself, the uncertainty in pointing can have a large impact on the calibration of balanced measurements made at low elevation angles using tipping measurements [Han and Westwater, 2000]. This effect is not directly assessed here but it can be reduced by making the tipping measurements at the same elevation angles in opposite horizontal directions. The pointing mirror for SPÉIR has been designed to allow this technique to be used (Section 3.2.2).

The retrieval of low altitude O<sub>3</sub> is particularly sensitive to an uncertainty in the temperature of the calibration loads, with an error of ~10% at 10 km due to a 0.5 K uncertainty in the blackbody temperature. Temperature gradients on the surface of the blackbody targets caused by changes in the lab environment are anticipated to be the largest source of uncertainty and so keeping both the cold and hot targets thermally insulated from the environment is important for retrieving accurate information about tropospheric O<sub>3</sub> concentrations. The beam propagating from the calibration targets to the horn are such that they cover a small area of the targets (Section 3.2.3), for the same reason.

## 4. Observation system characterization and simulation experiments

---

All of the error contributions to the retrieval of ClO at the lowest retrievable altitudes decrease in the case of ClO\*. The measurement error in particular decreases by ~50% in the 18-25 km altitude range. This is due to the higher atmospheric concentrations over this altitude range producing a larger SNR for the spectrum. In contrast, the measurement error has slightly increased at higher altitudes because the enhanced concentration of ClO at ~19 km attenuates the emission signal from ClO situated higher in the atmosphere (as explained in Section 4.3.2). The errors due to uncertainty in the tropospheric correction factor for HNO<sub>3</sub> and ClO have a magnitude similar to that of the measurement noise error. Errors due to uncertainties in spectral parameters can be quite large, and differ greatly between each species and altitude. The error is predominantly due to uncertainties in the air broadening parameter, *agam*, and its temperature coefficient, *nair* (Section 2.2.2.2). Because these systematic errors are often larger than the statistical error, it is hoped that future laboratory measurements of the spectral parameters can improve measurements in this frequency range. Because it is difficult to distinguish between statistical and systematic errors, it is assumed here that the spectroscopic error is the only systematic error. The combined error (added in quadrature) from the other listed sources is shown in Figure 4.5 as the Total statistical error.

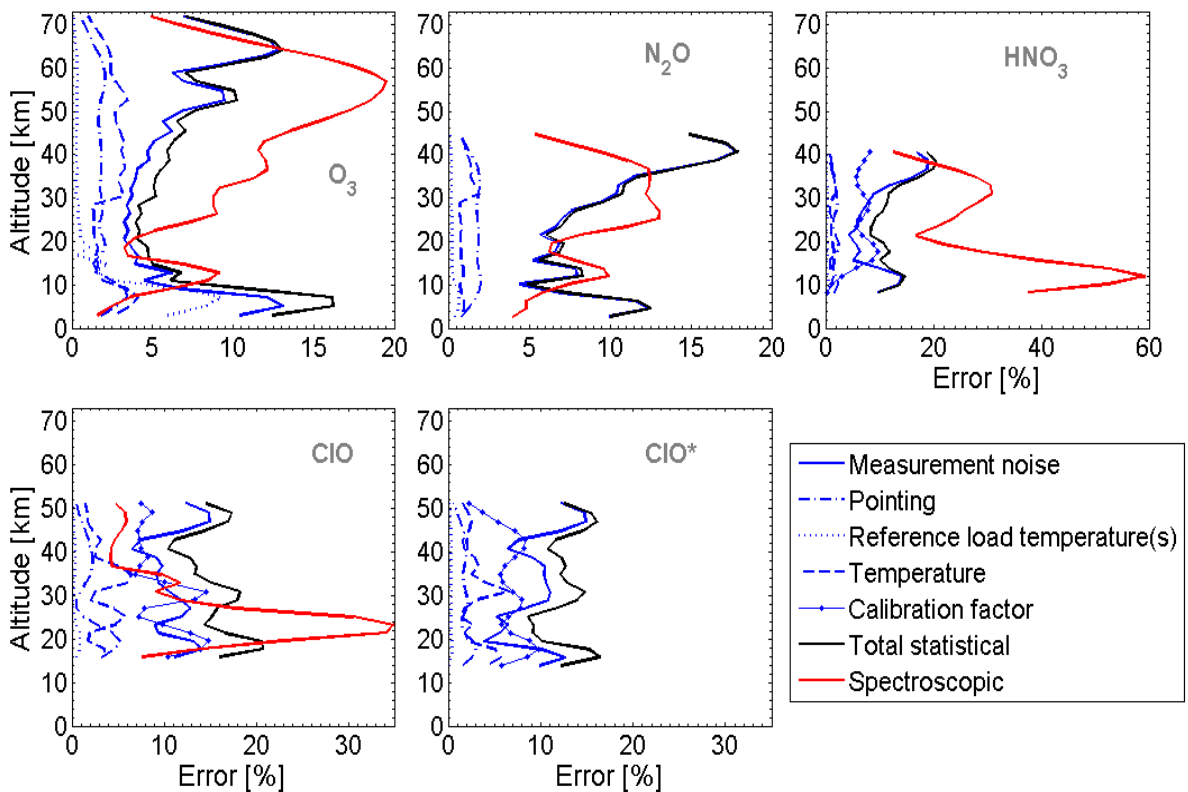


**Figure 4.5** The error contributions to the retrieval of each target species due to measurement noise and instrument and model uncertainties calculated using the linear optimal estimation method (OEM).  $ClO^*$  is a scenario for  $ClO$  when enhanced in polar spring. Error units are in percentage of the respective a priori.

### 4.3.4 Repeated simulation statistics (OSSEs)

To evaluate the performance of the observation system, multiple inversions were performed with simulated spectra for each target species. A similar method was used in [Eriksson et al., 2002] in characterizing the Sub Millimeter Radiometer (SMR) aboard the Odin satellite. Five hundred “true” atmospheric states were created for each target gas by allowing the a priori concentration profiles to vary randomly, constrained by the a priori error covariance,  $\mathbf{S}_a$ , and with a positive constraint, to give a log normal distribution at each altitude. Using the same constraint, atmospheric water vapour was also varied as well as any retrieved interfering species. For the  $HNO_3$  and  $ClO$  simulations, a reference beam spectrum was also constructed for each measurement in order to simulate the balanced measurement method. The reference beam spectrum, which was subtracted from an atmospheric spectrum, was generated using

## 4. Observation system characterization and simulation experiments

---

the Planck function for a blackbody in thermal equilibrium. Each reference spectrum was generated randomly so that its brightness temperature was within 2 K of the baseline of the atmospheric spectrum. Measurement noise was generated for each spectrum with a variance given by  $\mathbf{S}_e$ .

Simulated spectra were created from the true states using ARTS, including the instrument characteristics and noise contributions outlined in Section 4.2. The spectra were inverted and the differences between the retrieved and the true states were used to evaluate the performance of the inversion. The mean and standard deviation of the differences were compared to the OEM estimates. The OEM retrieval error,  $\mathbf{S}$  (smoothing error plus measurement error), agrees very well with the standard deviation of the difference between the retrieved and simulated profiles over the retrievable altitude range, as shown in Figure 4.6. Outside of this range, the OEM retrieval error tends to underestimate the standard deviation.

The bias for the set of 500 retrievals, defined here as the mean of the difference between the retrieved and true profiles, shows some structure for each of the gases, as shown in Figure 4.6. The bias is  $< |3\%|$  at most altitudes and tends to increase at the upper and lower limits of the retrieval altitude range i.e. altitudes over which the measurement response is decreasing from 1 to 0.8 (see Figure 4.4).  $O_3$  shows a negative bias in the troposphere below 10 km with a peak of  $\sim -5\%$  and  $HNO_3$  shows a bias with a maximum of  $+6\%$  in a peak at 35 km altitude.  $ClO$  shows a bias which oscillates about zero over the whole retrievable altitude range with a maximum absolute value of 3%. Normally, for a single retrieval, it is difficult to assess the difference between the retrieved and true state because there are many contributions to the error budget, both random and systematic. In this case there are no systematic errors included in the simulations and no added baseline. The biases are instead attributed to a combination of non-linear effects, which is discussed in Section 4.3.5.

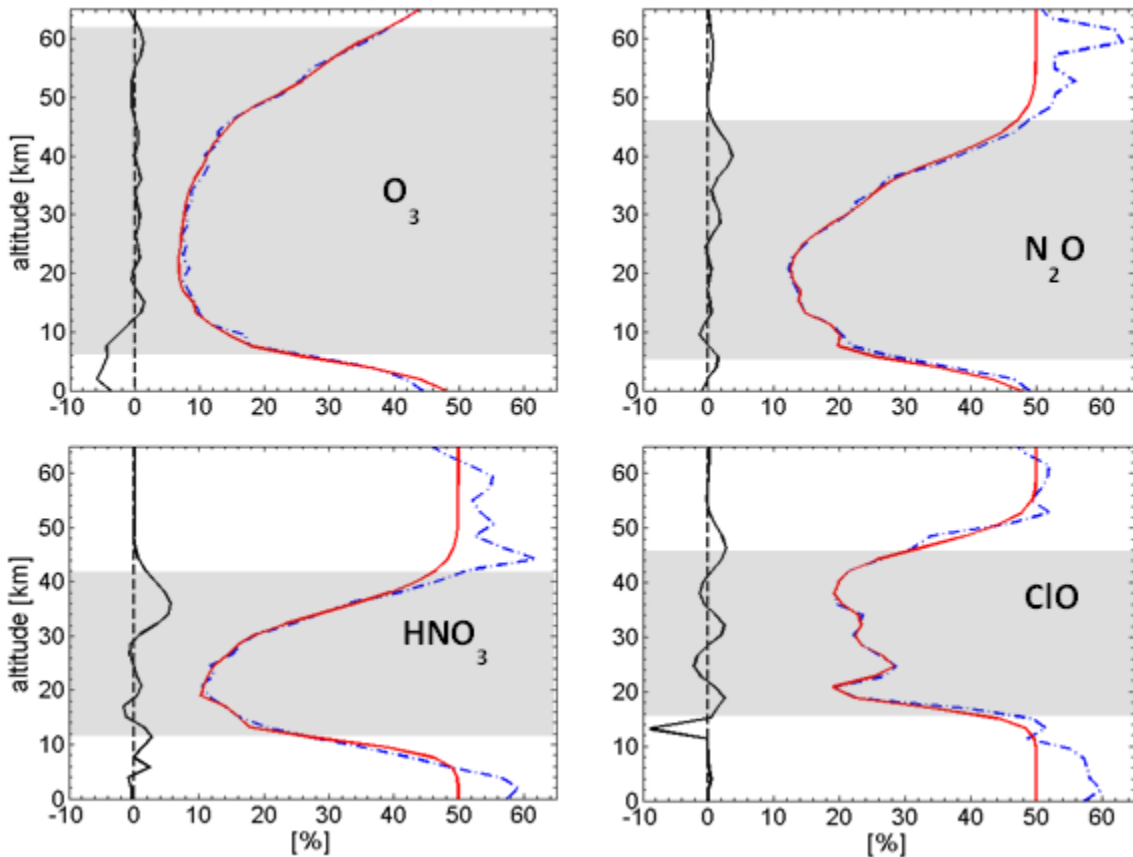


**Figure 4.6** A comparison of the OEM characterization and the errors in 500 nonlinear inversions of simulated spectra. The retrieval altitude range, without a polynomial fit to the baseline (see Figure 4.3), for each species is shaded. Red: OEM retrieval error (measurement and smoothing error). Dash/Dot Blue: standard deviation of differences between retrieved and generated true atmospheric states for 500 inversions. Black: mean of differences between retrieved and generated true atmospheric states (bias). Dashed black: optimal bias (zero mean). Note: the spike in the ClO bias at  $\sim 13$  km is caused by interpolation about a discontinuity in the ClO a priori VMR profile.

It should be noted that this study is based on the use of covariance matrices with Gaussian statistics but the behavior of gas concentrations in the atmosphere can deviate from this assumption. A ClO concentration in the polar vortex during spring, at a retrieval grid-point in the lower half of the retrieval altitude range can be expected to have a multiple-peaked probability density function and, while beyond the scope of the work presented here, a dedicated study would be needed to evaluate such situations.

### 4.3.5 Nonlinearity in the inversion

In a retrieved profile, some of the information will have come from the measurement noise on the spectrum. The VMR patterns from noise have an oscillatory structure and vary in magnitude and vertical scale; spectra with smaller SNRs will give rise to oscillations in a retrieved profile with larger magnitudes and with larger vertical scales [Hansen, 1992]. As a result, the dominant oscillations in a retrieved profile will have a scale similar to that of the altitude resolution of the profile. Because they are statistical in nature (as opposed to systematic), the appearance of these errors will be drastically reduced for an average of 500 profiles, and so the contribution to the biases in Figure 4.6 from oscillations in individual retrieved profiles is considered to be negligible.

The biases in Figure 4.6 (clearly seen for tropospheric O<sub>3</sub> and for HNO<sub>3</sub> around 35 km, for example) are attributed to nonlinear effects in the inversion. A simple test, outlined in Section 2.4.3, was carried out to assess the degree of nonlinearity of the inversion for each species. The theoretical,  $w_m$ , and practical,  $w_{pm}$ , measurement responses are plotted for each gas in Figure 4.7 when using both a linear and a nonlinear inversion scheme. Areas of nonlinearity for each species correspond to altitudes at which the practical measurement response differs from the theoretical measurement response. Areas found to have the highest degrees of nonlinearity are those near the limits of the retrieval range. This nonlinearity is the reason for the larger peaks in the biases at these altitudes in Figure 4.6. This is because, for some species, the inversion has a different measurement response for a true state concentration that is higher than the a priori than it does for a true state concentration that is lower than the a priori. These differences in the measurement response for a linear and a nonlinear inversion scheme indicate that a nonlinear scheme is needed to retrieve atmospheric concentrations using SPÉIR.

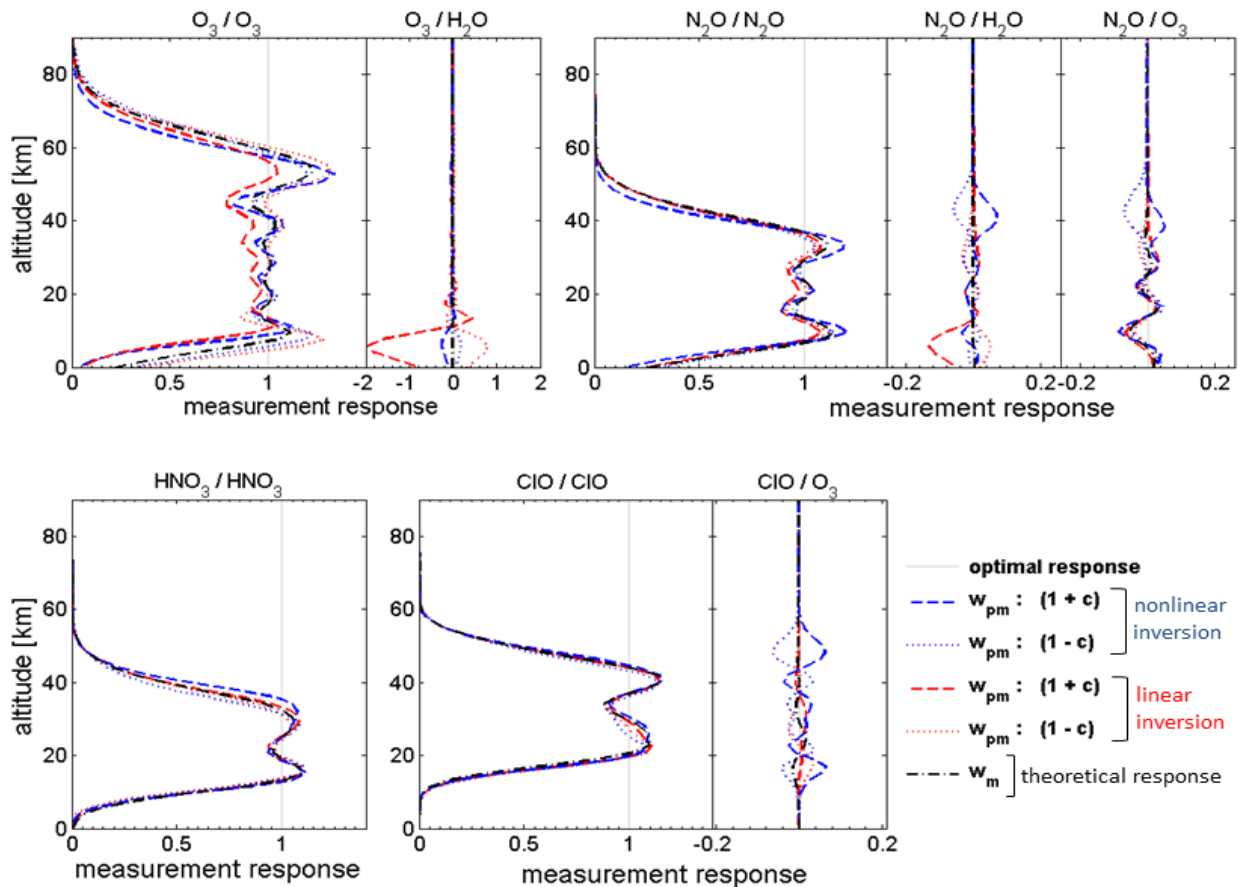


**Figure 4.7** The practical measurement responses ( $w_{pm}$ ) for all retrievable species (target and interfering) in each band, found using linear and nonlinear inversion schemes. The true state for each inversion is larger or smaller than the a priori by a factor of  $(1 \pm c)$ , where  $c = 0.3$ . The theoretical response ( $w_m$ ) and optimal response are also plotted. X/Y given in the title of each plot denotes the response of the retrieval of species X to a change in species Y. Refer to Section 2.4.3 for details.

The bias for  $HNO_3$  around 35 km (discussed in Section 4.3.4, Figure 4.6) corresponds to an area of nonlinearity shown in Figure 4.7. From the 500  $HNO_3$  true states used in Section 4.3.4, those with a true state greater than the a priori at 35 km have a bias of -10.7 %, compared to a value of +18 % for those with a true state that is less than the a priori. Therefore, a climatology calculated for  $HNO_3$  at 35 km, by simply averaging these retrieved profiles, would have a positive bias with respect to the true climatology at that altitude.

The bias found for tropospheric  $O_3$  is due to differences in its measurement response as well as the response to the interfering retrieved species,  $H_2O$ . The retrieved  $O_3$  profile is also depend-

ent on H<sub>2</sub>O concentrations in the troposphere, where H<sub>2</sub>O has a large vertical VMR gradient, and it responds differently depending on whether the concentration is larger or smaller than the a priori. Based on this, an O<sub>3</sub> climatology that averages retrievals from a group of true states with an equal number of increases and decreases in atmospheric gas concentrations relative to the a priori will have a negative bias of about 5% in the troposphere. In addition, if comparing tropospheric O<sub>3</sub> in the Arctic winter, when both O<sub>3</sub> and H<sub>2</sub>O concentrations are low, to later in the year when they have both increased, then the calculated difference in O<sub>3</sub> could have a bias of ~10%.

Ideally, O<sub>3</sub> (and all of the target species) would have a response of zero to other gases in the atmosphere. The measurement responses of N<sub>2</sub>O and ClO in Figure 4.7 show a similar relationship to the biases in Figure 4.6: namely the areas of nonlinearity (Figure 4.7) and bias (Figure 4.6) in the 40 km altitude region for N<sub>2</sub>O, and the oscillatory structure of the nonlinearities and biases for ClO.

The inversion problem here is considered moderately nonlinear: linearization is adequate for the error analysis, but not for finding a solution [Tarantola and Valette, 1982]. The weighting functions specific to a single nonlinear inversion should be used in interpreting a retrieved VMR, especially if using a large number of profiles to produce climatologies or to assess trends. It should be noted that since the probability density functions for the prior knowledge of the atmospheric concentrations used here are Gaussian, the nonlinearity depends predominantly on the forward model [Rodgers, 2000], and so in general, the results will apply similarly to another observation system operating in the same frequency range.

### 4.4 Conclusion

A characterization and simulation of a ground-based millimeter-wave observation system for Arctic research was performed. The goal was to assess the performance and error budget for SPÉIR, measuring emission spectra from O<sub>3</sub>, HNO<sub>3</sub>, N<sub>2</sub>O, and ClO, while housed at PEARL in Eureka, Nunavut, Canada (80.05°N, 86.42°W, 610 m a.s.l.).

Inversion studies using an optimal estimation method estimated the altitude ranges over which retrievals of concentrations can be made. The ranges varied over the stratosphere, the

## 4. Observation system characterization and simulation experiments

---

largest and smallest being for O<sub>3</sub> and HNO<sub>3</sub>, respectively. The predicted altitude resolution of these retrievals ranged between 5 and 15 km depending on the species and height. Error analysis with the OEM showed that uncertainties in model and instrument parameters contributed to statistical error between approximately 5% and 10% for the retrieval of O<sub>3</sub>, 5% and 15% for N<sub>2</sub>O, and 10% and 20% for ClO and HNO<sub>3</sub>. Tropospheric O<sub>3</sub> showed a strong sensitivity to uncertainties in the absolute temperature of the blackbody calibration targets, resulting in an error of ~10% at 9 km altitude. Errors for ClO were found to decrease for an atmosphere with a significantly enhanced ClO concentration, typical of Arctic spring. Errors due to uncertainties in spectroscopic parameters varied largely between species and altitude, and were often larger than the statistical error.

The mean and standard deviation of the difference between the true and retrieved state in 500 simulated inversions was calculated for each target species and compared to the analysis derived from OEM. The comparison showed good agreement, in the retrievable altitude ranges, between the OEM derived and the simulation errors but showed that biases, defined as the mean of the difference between the retrieved and true profiles, are present in the retrievals at some altitudes, in particular for HNO<sub>3</sub> and tropospheric O<sub>3</sub>. These biases are attributed to the effects of nonlinearities in the forward model in the 265 – 280 GHz frequency range. While a linear treatment of the inversion is adequate for error analysis, a nonlinear inversion scheme was found to be needed to retrieve concentration profiles for all species. It is important to use the final weighting functions to characterize each retrieved state because not doing so will incur errors on the order of 10% when averaging data for producing climatologies or when analyzing trends. These simulations show the promising capability of the designed millimeter-wave observation system operating in Arctic conditions.

# Chapter 5

---

## 5 The effect of spectroscopic parameters

This chapter is based on a sensitivity study that was performed to assess the impact that uncertainties in the spectroscopic parameters of molecules have on ground-based measurements of atmospheric gases in the 265 – 280 GHz frequency range. The work was performed specifically for SPÉIR, but the results are applicable to any of several other ground-based instruments operating in this frequency range. A secondary goal of the study was to identify the molecules and spectroscopic parameters which contribute the largest error to retrieved atmospheric concentration profiles in order to provide recommendations for new laboratory measurements.

### 5.1 Forward and inversion modelling

The errors in retrieved profiles were calculated with ARTS and Qpack (see Section 4.1) using OEM error analysis. Section 2.4.2 describes how the error covariance matrices (ECMs) are calculated for data that is part of the forward model parameters and so the reader is directed there for details. It is the forward model parameter ECM,  $\mathbf{S}_b$ , which contains the errors coming from uncertainties in the spectroscopic data, among others. The perturbations used for calculating the Jacobians for the spectral parameters (see Section 2.4.2) were the uncertainties that are taken from spectral line catalogues or literature, described below.

### 5.2 Spectroscopic parameter setup

The information on spectral line parameters which were used for this study is from the JPL database and the HITRAN 2008 database (herein HITRAN), between 250 – 300 GHz. The JPL catalogue carries a more extensive list of spectral lines in the millimeter-wave region of the spectrum but only contains uncertainty information on the line position and line intensity and no information on the broadening parameters or pressure shifts. The HITRAN catalogue contains

uncertainty information on all of the parameters mentioned in Section 2.2.2.2, where available, except for  $n_{self}$  and most of the  $p_{shift}$  values in the 250 – 300 GHz region. The information in both catalogues comes from a variety of sources, theoretical and experimental. The line position and line intensity information used in this work are taken from the JPL catalogue as it was found to be the same or more accurate than HITRAN. When not available from either catalogue, data for this study is taken or inferred from the referenced literature, as discussed below.

The air broadening,  $agam$ , and temperature dependence,  $nair$ , uncertainties were not listed in the HITRAN database for a number of ClO and HNO<sub>3</sub> lines. For ClO, the parameters for lines with upper rotational quantum numbers,  $J'' < 20.5$  are listed as an approximation from a linear fit to three good values measured at 204, 501, and 649 GHz [Oh and Cohen, 1994; Bauer et al., 2000]. From information listed in these references, the uncertainties for  $agam$  and  $nair$  for ClO used in the simulations were set to 5% and 10% respectively. The  $agam$  parameter for HNO<sub>3</sub> lines in the region of interest is referenced in HITRAN from [May and Webster, 1989]. From this and a study by [Zu et al., 2002], the  $agam$  and  $nair$  uncertainties for HNO<sub>3</sub> lines used in the simulations are chosen as 10% each. The chosen values are only approximations to the uncertainties, as indeed are the listed parameters themselves, because the broadening parameter and its temperature dependence rely on both the molecule and on the rotational quantum numbers, which means that they vary from line to line. A few of the  $nair$  uncertainties for O<sub>3</sub> lines in SPÉIR’s spectral range are not listed in HITRAN. For the lines which do have an  $nair$  uncertainty, it is listed at 10% in [Wagner et al., 2002], and so this value was used for the remaining lines which lacked an uncertainty value.

The uncertainties for the self-broadening parameter,  $sgam$ , were not listed between 250 – 300 GHz for the target gases in HITRAN in many cases and not at all for its temperature dependence,  $n_{self}$ . All of these values are assumed to have a negligible impact on retrievals due to the small concentrations of the trace gases in the atmosphere. When not available, an uncertainty of 200% was used for both parameters in the calculations in this study, and the above assumption of near-zero impact was found to be valid (see Section 5.4.1).

Since there is almost no data on the pressure shift uncertainty except for a few H<sub>2</sub>O lines, a single value for all lines of a particular species was used as in [Verdes et al., 2004]: 150 Hz/Pa for O<sub>3</sub> and N<sub>2</sub>O lines, 2250 Hz/Pa for H<sub>2</sub>O lines, and 7500.6 Hz/Pa (1MHz/Torr) for HNO<sub>3</sub> and ClO lines. This is most likely an overestimation, especially for HNO<sub>3</sub> for which a study in [Demaison et al., 2004] has shown relatively small values for the pressure shift. The few uncertainties quoted in HITRAN for the H<sub>2</sub>O pressure shift were small compared to the above value that was adopted from [Verdes et al., 2004], and where they were quoted the value was left unchanged. It should be noted that the pressure shift parameter for a given molecule may be positive or negative and depends on the temperature, the perturbing gas, the vibrational band, and the rotational transition [Demaison et al., 2004]. No correlation is assumed between the uncertainties in the different parameters and lines except for a 0.6 correlation between the same parameter of HNO<sub>3</sub>, as in [Verdes et al., 2004]. Considering the large number of spectral lines in clusters for HNO<sub>3</sub>, there is bound to be correlation in the parameter values, but the exact number used was for consistency in the method.

As spectral lines are most often identified according to the species and the position, it is important to note that JPL and HITRAN may in some cases specify a slightly different position when referring for the same line. For instance, as can be seen in the plots in Section 5.4.1, the O<sub>3</sub> spectral line defined by JPL at 278.521 GHz and by HITRAN at 278.522 GHz refers to the same rotational transition of O<sub>3</sub>.

### 5.3 Instrument and inversion setup

The parameters used for the instrument and inversion are the same as those used for the OS-SEs in Chapter 4. All of the information on the instrument and inversion parameters is contained in Section 4.2, and so is not repeated here. The line strengths of the dominant rotational transitions are shown in Figure 4.2, as well as an example of simulated spectral lines. The reader should keep in mind the retrieval altitude ranges determined in Section 4.3.2 (shown in Figure 4.3) when relating the results here to SPÉIR.

## 5.4 Effects on retrieved concentration profiles

This section assesses the error contribution, from uncertainties in spectroscopic data, to retrieved atmospheric concentration profiles of the target species of SPÉIR. The results for the four target species are shown and discussed in groups defined by the spectroscopic parameter. Where the errors are displayed as a percentage, it is the percentage of the a priori VMR concentration at that altitude point. The total error from a parameter is also calculated as the sum in quadrature of the errors from individual lines. The spectral lines and parameters that contribute most significantly to the error budget are identified and, of these, suggestions are made about for which it would be most beneficial to have a more accurate knowledge.

### 5.4.1 Results

Figure 5.1 shows the errors in the retrieved profiles of each of the SPÉIR target species due to uncertainties in the positions of spectral lines. The retrieval precision, taken as the sum of the measurement error and smoothing error in the retrieved state (see Section 2.4.2), is also plotted for reference. In general, the positions of the lines in the 265 – 280 GHz spectral region are sufficiently well known so that the uncertainties show little effect on the retrieved profile (< 1%). The exceptions are two O<sub>3</sub> lines: at 273.051 GHz and 278.521 GHz. The former is the primary line that will be used for the O<sub>3</sub> measurements by SPÉIR and the uncertainty in its position is 120 kHz; the errors in the O<sub>3</sub> profile from position uncertainties are dominated by this line, with a value of 20% at 10 km altitude and around 50% in the upper stratosphere. The latter, with a 90 kHz uncertainty, is the dominant error due to position in the ClO retrieval, more so than the target ClO lines themselves which contribute < 1%.

## 5. The effect of spectroscopic parameters

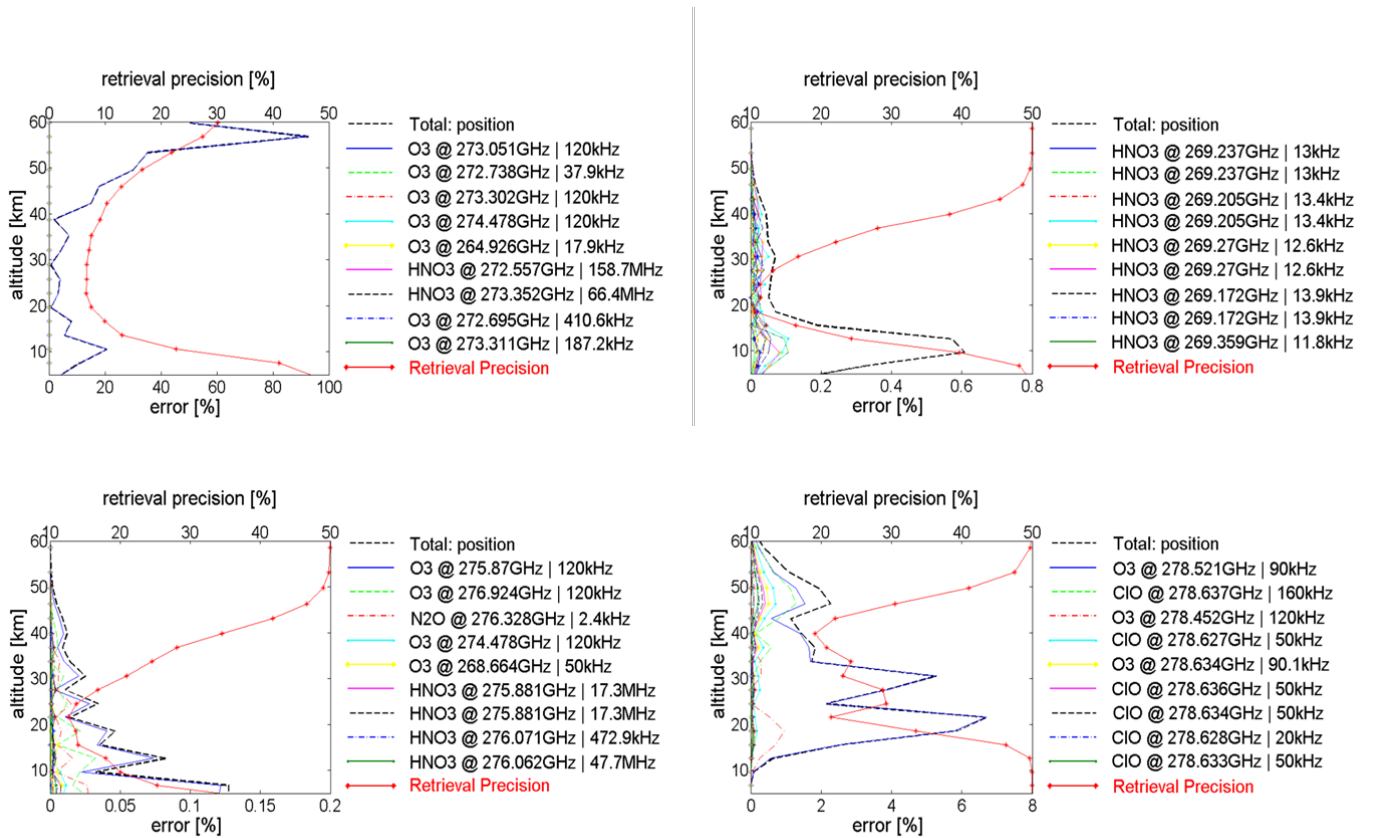


**Figure 5.1** Errors in the retrieved profiles of (moving clockwise from top left) O<sub>3</sub>, HNO<sub>3</sub>, ClO, and N<sub>2</sub>O from uncertainties in the positions of spectral lines (shown as a percentage of the a priori at each altitude). For clarity, only the nine lines which contribute most to the error are shown in the legend. The lines are listed in the legend in order of largest to smallest error contribution.

The format of the legend is: “species” @ “line position” | “uncertainty from catalogue”. The retrieval precision (see Section 2.4.2) is also displayed with its X-axis shown at the top of each plot.

The intensities of the lines in this spectral region, as listed in the spectral line catalogues, are well known: to within 2% for any of the lines that have an impact on the error budget. Shown in Figure 5.2, the error in the O<sub>3</sub> and N<sub>2</sub>O retrievals come predominantly from the strong 273.051 GHz O<sub>3</sub> line and 276.328 GHz N<sub>2</sub>O line respectively: the target lines for observation of the respective gases. The error in the O<sub>3</sub> retrieval shows a linear response to the uncertainty, with values of approximately 2% over most altitudes. This is similar for N<sub>2</sub>O, but with more oscillation over the altitude range and maxima up to 2.5%. The errors above 20 km altitude in the HNO<sub>3</sub> profile also show a linear response to the uncertainty but due to the large number of HNO<sub>3</sub> lines in close proximity, the total combined error in the profile is larger (about 3% - 4%).

## 5. The effect of spectroscopic parameters

Below 20 km the total error in the HNO<sub>3</sub> profile from intensity peaks at 15%, with a half-width of about 10 km. The error in the ClO retrieval is again almost completely due to uncertainties in adjacent, stronger O<sub>3</sub> lines, this time at 278.522 GHz and 278.453 GHz. The errors from these two lines combine to produce a peak in the total error with a maximum of 12% at 21 km, and a half-width of about 10 km.

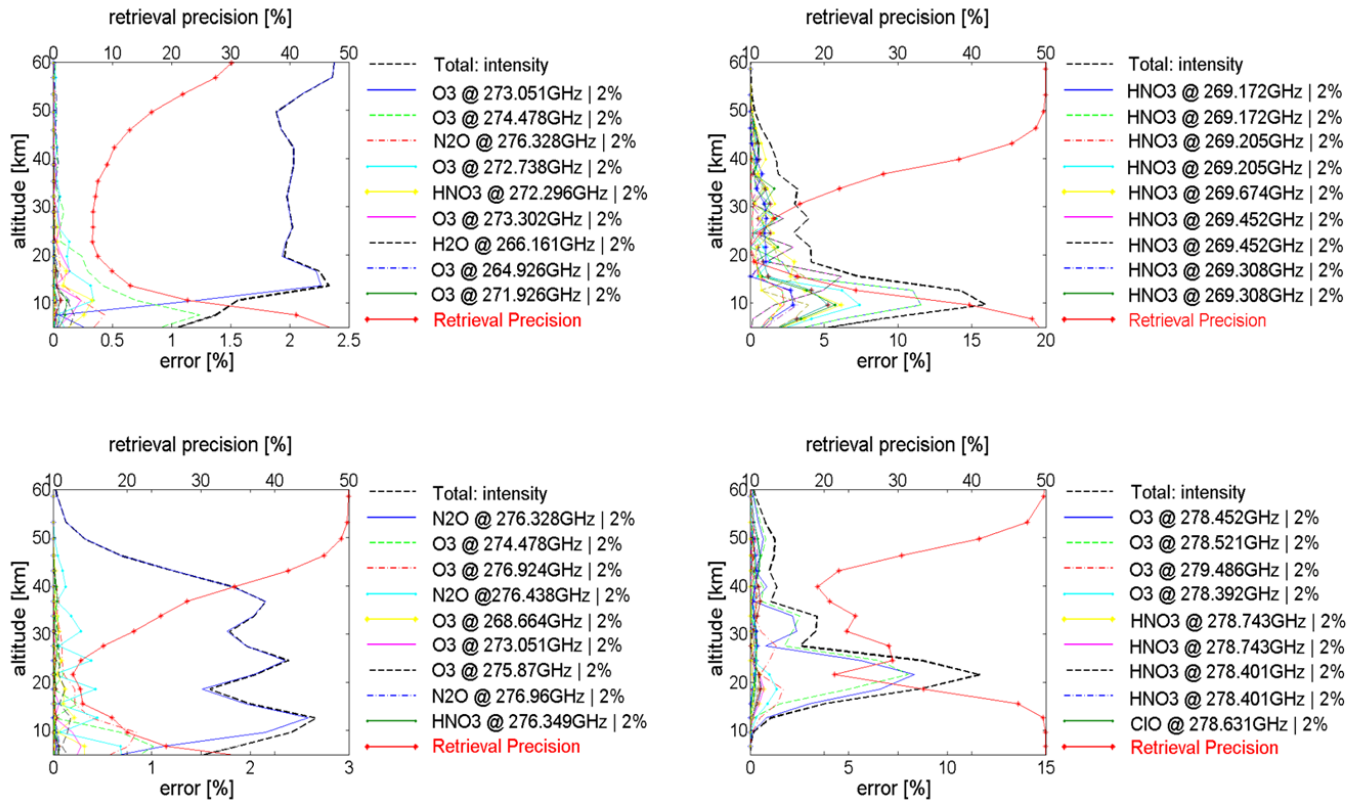


**Figure 5.2** The same as Figure 5.1, but for the uncertainties in the line intensity parameter.  
(Clockwise from top left: O<sub>3</sub>, HNO<sub>3</sub>, ClO, N<sub>2</sub>O)

The errors due to uncertainties in the air broadening parameter, *agam*, are found to be the largest contribution to the error budget from spectroscopic parameters. The errors in the profile generally have varying values throughout the altitude ranges, as shown in Figure 5.3. For the weaker spectral signatures, HNO<sub>3</sub> and ClO, the errors in the profile show a greater re-

## 5. The effect of spectroscopic parameters

spose to the agam uncertainty when compared to stronger spectral signatures of N<sub>2</sub>O and O<sub>3</sub>. 10% uncertainty in the agam the two HNO<sub>3</sub> lines at 269.172 GHz give rise to a maximum peak in error for the HNO<sub>3</sub> retrieval greater than 40% each. For ClO, a 10% uncertainty in a nearby O<sub>3</sub> line at 278.522 GHz causes a maximum peak in uncertainty of approximately 30%.

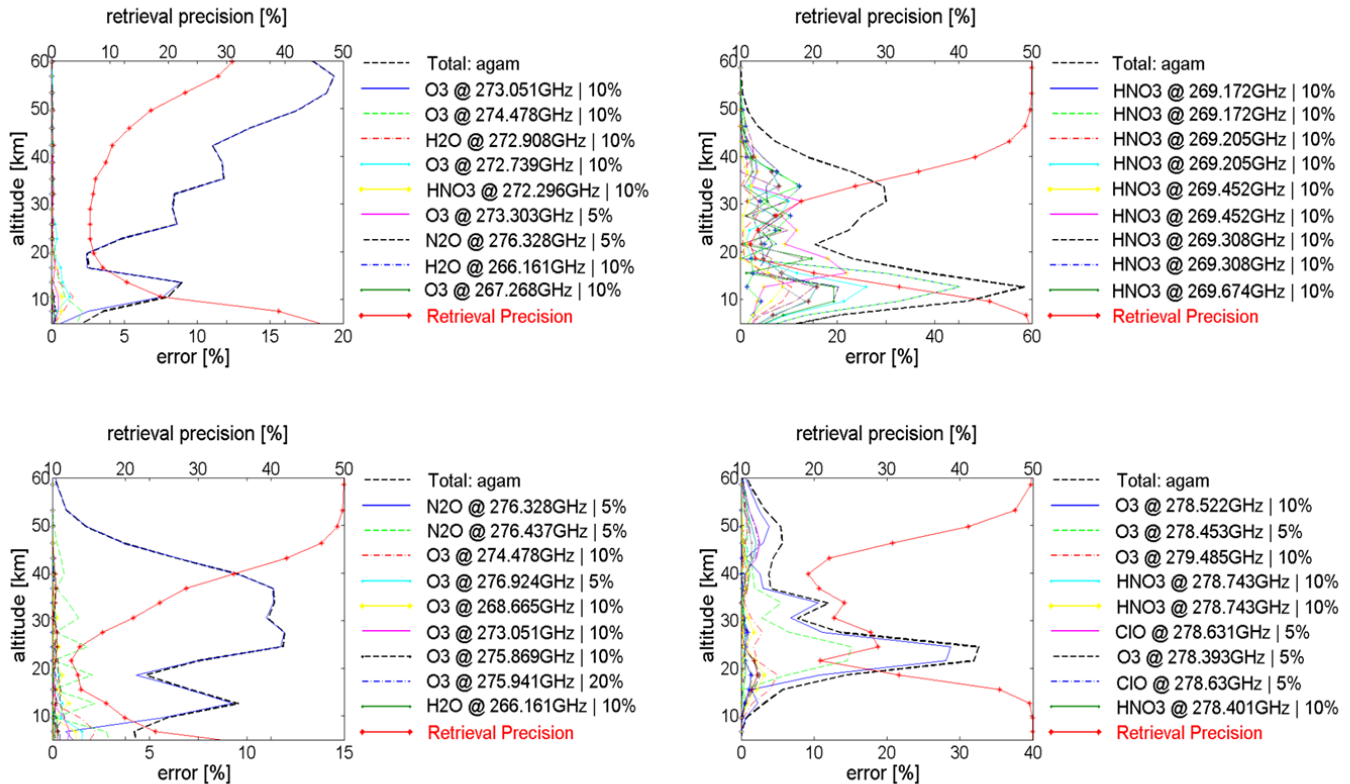


**Figure 5.3** The same as Figure 5.1, but for the uncertainties in the agam parameter.  
(Clockwise from top left: O<sub>3</sub>, HNO<sub>3</sub>, ClO, N<sub>2</sub>O)

## 5. The effect of spectroscopic parameters

The errors from uncertainties in the temperature coefficient of the air broadening parameter, nair, are shown in Figure 5.4 and have a similar altitude structure to the respective errors from agam but with lower absolute values. While the values of the uncertainties in nair are similar or exceed those of agam, the retrieval is not as sensitive to this parameter.

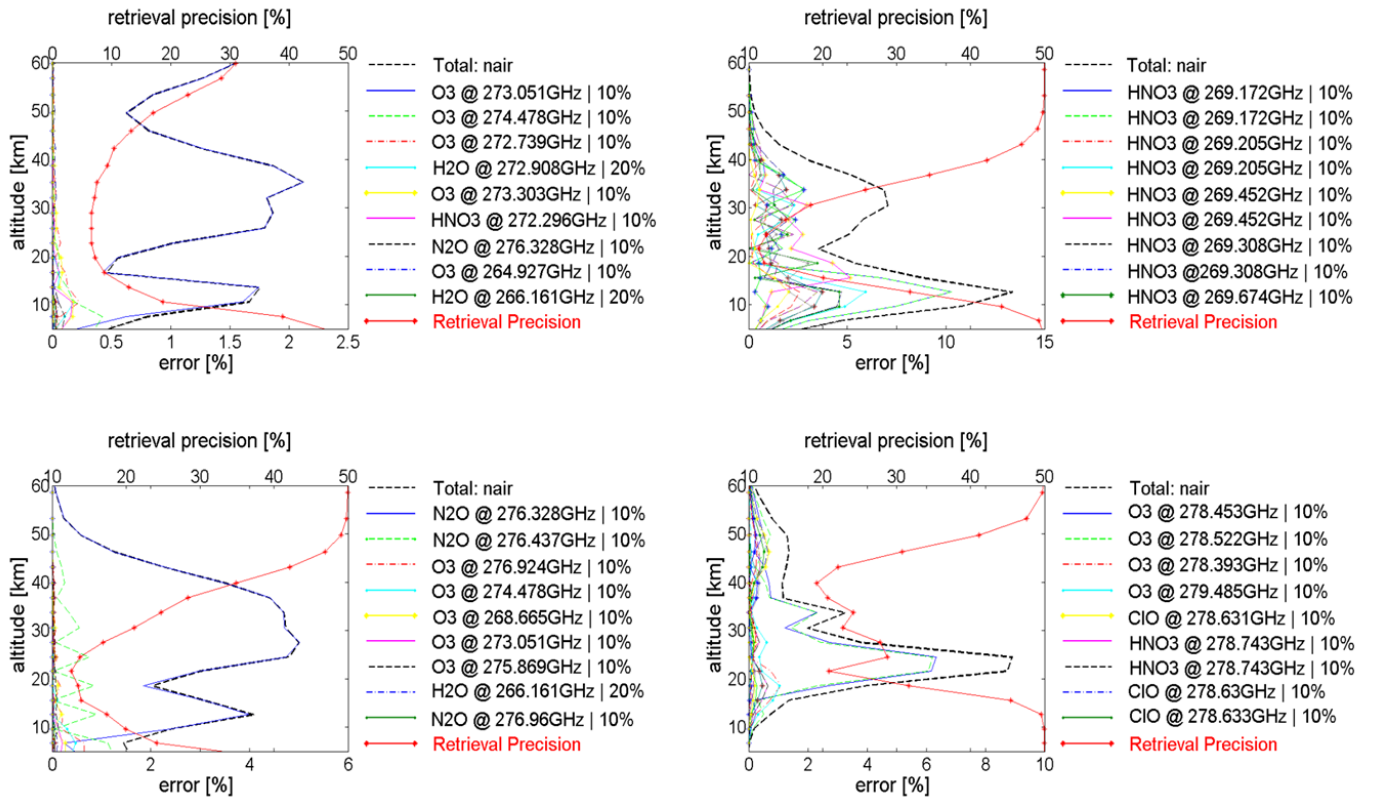


**Figure 5.4** The same as Figure 5.1, but for the uncertainties in the nair parameter.  
(Clockwise from top left: O<sub>3</sub>, HNO<sub>3</sub>, ClO, N<sub>2</sub>O)

Contributions to the error from uncertainties in the self broadening parameter and its temperature coefficient, sgam and nself respectively, were negligible in all cases due to the small concentrations of each target species in the atmosphere. Even when using an uncertainty of 200% the errors in the retrieved profiles were found to be fractions of a percent.

The errors due to the pressure shift, pshift, parameter are shown in Figure 5.5. The absolute values vary strongly over altitude and with species, with large errors present at low altitudes

## 5. The effect of spectroscopic parameters

where the atmospheric pressure is relatively high. The total error in the HNO<sub>3</sub> profile is as high as 1000% around 13 km but it must be noted that the estimate for the pshift uncertainty is a very conservative one at 7500 Hz/Pa. A study in [Demaison et al., 2004] has shown that the values are most likely a lot smaller (the values were not used here as they are for higher frequency lines). The largest errors in the ClO profile come from lines with the same uncertainty estimate of 7500 Hz/Pa but there is also a strong contribution from the O<sub>3</sub> line at 278.522 GHz (peaking at 20% at 21 km) which has a relatively small pshift uncertainty of 150 Hz/Pa. In the O<sub>3</sub> profile, the uncertainty of 150 Hz/Pa for the main observation line at 273.051 GHz causes a large error of 80% in the retrieved profile at 10 km altitude. The precision of the O<sub>3</sub> retrieval at that altitude is 20%.

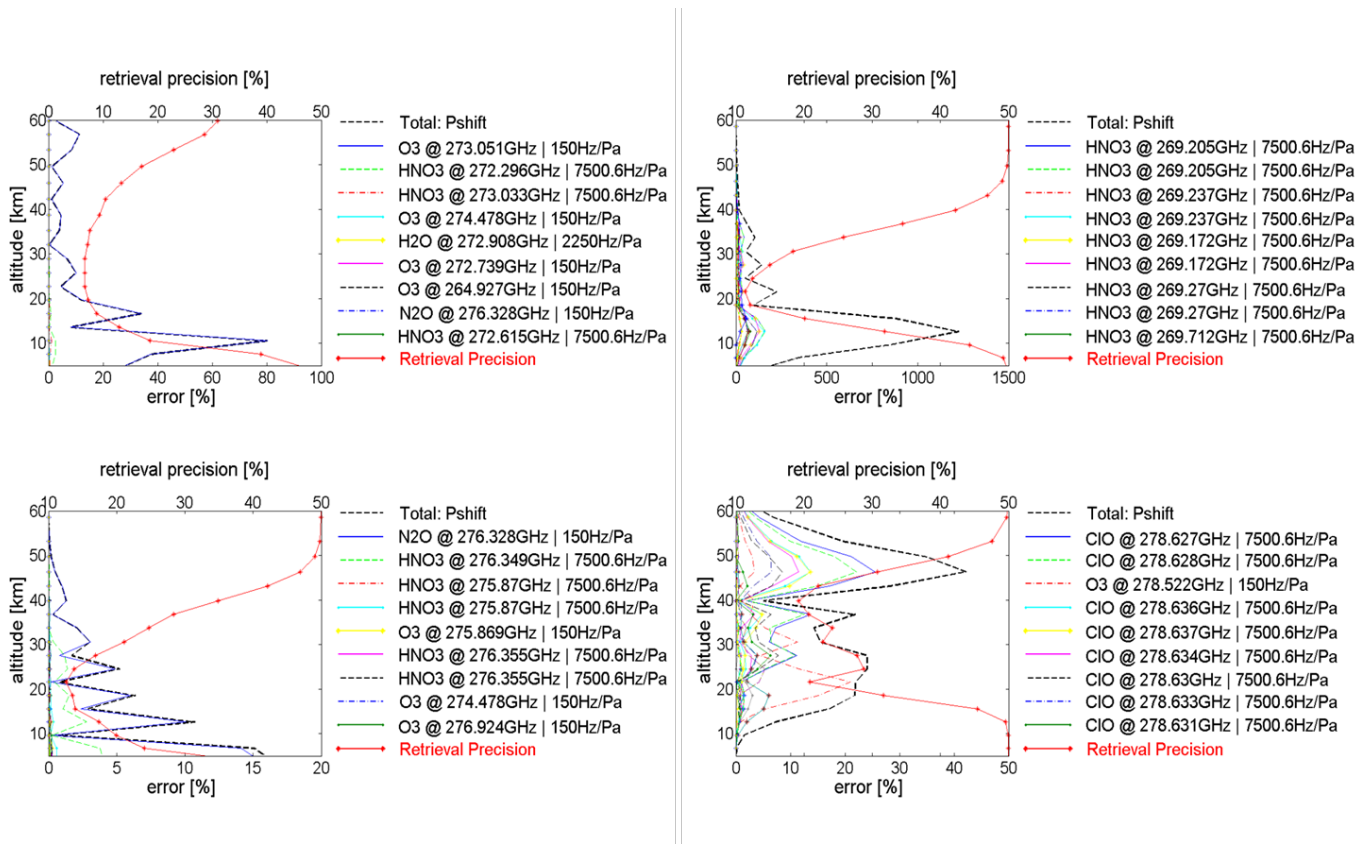


**Figure 5.5** The same as Figure 5.1, but for the uncertainties in the pshift parameter.  
(Clockwise from top left: O<sub>3</sub>, HNO<sub>3</sub>, ClO, N<sub>2</sub>O)

### 5.4.2 Discussion of the results

It is found that, for the gases with larger spectral signals ( $O_3$  and  $N_2O$ ), the errors in the retrieved profile are dominated by the uncertainties in the parameters of the main observation line, which is usually the strongest. For  $HNO_3$ , the uncertainties of a large number of lines in close proximity can contribute to a total error much larger than that of a single line. For  $ClO$ , a gas with a weak atmospheric signature, the error is dominated by uncertainties in parameters belonging to other gases with stronger signatures that lie nearby in frequency. In this case it is the nearby  $O_3$  lines which contribute the most to the spectroscopic error in the retrieval of  $ClO$  using the 278.6 GHz spectral line. The results showed that the parameter which consistently causes the largest errors in the retrieved concentration profiles of atmospheric gases is the air broadening parameter,  $agam$ . Generally the uncertainties of the  $agam$  parameter listed in HITRAN and JPL catalogues are 10% between 250 – 300 GHz.

With regards to uncertainties in the line position, the error introduced into the retrieved profile can be eliminated by simply changing the value of the line position to that which is observed in the measured spectrum. This is easiest to do in the case of lines that have little interference from other trace gases, such as  $O_3$  at 273 GHz, as one could find the centre of the line with a centre of mass calculation, for instance. This solution also assumes that there is no “stretching” of the frequency channels in the spectrometer that is causing the problem (if the problem was a constant shift in the frequency of all channels, this would also be solved by changing the value of the line position).

At about 21 km altitude, there is a local maxima in the Eureka climatological VMR profile of  $ClO$ . The concentrations at this altitude can increase by a factor of 10 during Arctic winter [Manney et al., 2011] and it is an interesting area to study in relation to stratospheric ozone chemistry and polar stratospheric clouds. It is at approximately 21 km where there is a peak in the error in the  $ClO$  profile for each spectroscopic parameter investigated here. This error arises predominantly from nearby  $O_3$  lines and is believed to peak consistently at this altitude for two reasons: The retrieval precision has a relatively low value at this altitude, and for the OEM inversion more information is coming from the measurement as opposed to the a priori profile (see Section 2.4.2); it is the information coming from the measurement that includes the data

in the spectroscopic catalogues. The second reason is that the nearby O<sub>3</sub> lines lie sufficiently far in frequency from the ClO lines that the part of the O<sub>3</sub> spectral signature which interferes with the ClO retrieval is the slowly varying (in frequency) feature caused by strong pressure broadening in the lower atmosphere. This signature, which originates from O<sub>3</sub> molecules in the lower stratosphere, will interfere with the retrieval of ClO in the lower stratosphere and not with the retrieval of ClO higher in the atmosphere where emissions from molecules give sharper spectral signals. Adding together in quadrature the error here, the retrieval of ClO at 21 km has a total error of ~42% coming solely from spectroscopic uncertainties. Because this error is systematic, observed trends in ClO concentrations will be unaffected but it is a problem if one wishes to use ground-based measurements from any of the instruments mentioned in Section 3.1 to assess the chlorine budget in the lower stratosphere, for example. The error in the pshift parameter was included in this calculation because at 21 km the error is dominated by an uncertainty of 150 kHz/Pa for an O<sub>3</sub> line at 278.55 GHz, and not from the conservative uncertainty of 7500 Hz/Pa for ClO lines.

In order to reduce the influence that the spectroscopic parameters of O<sub>3</sub> lines have on the retrieval of ClO, the retrieved state of O<sub>3</sub> using the target line at 273 GHz can be used as the a priori O<sub>3</sub> state for a retrieval of ClO. The lower uncertainty of this a priori O<sub>3</sub> state will mean that the ratio of information from the measurement to that from the a priori will lessen, and reduce the impact of the spectroscopic parameters from the O<sub>3</sub> lines closest to ClO. This new a priori state will, however, contain the systematic errors from the spectroscopic parameters of the O<sub>3</sub> target line at 273 GHz which will propagate through to the retrieved ClO state, but this resulting error is expected to be less.

## 5.5 Conclusion and recommendations

The sensitivity of ground-based millimeter-wave measurements of the atmosphere to inaccuracies spectroscopic parameter information was assessed. The study was based upon the SPÉIR design for measurements within 265-280 GHz, but the results are of relevance for a number of ground-based instruments that operate in this frequency range.

The uncertainties in the parameters of spectral lines which were found to cause the most significant errors in the retrieved profiles of O<sub>3</sub>, N<sub>2</sub>O, HNO<sub>3</sub>, and ClO, within 265 -280 GHz, are listed in Table 5.1. As mentioned in Section 5.4.2 , the position uncertainty can be accounted for in the inversion so this error is not considered as problematic as others. The pshift parameters listed in Table 5.1 do not include the HNO<sub>3</sub> and ClO pshift parameters as they are assumed to be largely overestimated. It is concluded that new measurements of the parameters in Table 5.1 would give the most benefit to retrievals of the target gases. New measurements made between 300 and 550 GHz, for the benefit of the proposed Millimeter-wave Acquisitions for Stratosphere/Troposphere Exchange Research (MASTER) satellite instrument, provided uncertainties in the agam parameter as low as 2% (down from 10%) for O<sub>3</sub>, and 5% (down from 30%) for N<sub>2</sub>O [Verdes et al., 2004]. For the O<sub>3</sub> nair parameter, the uncertainty was decreased from 10% to 2%. Similar measurements for the O<sub>3</sub> lines listed here would be of great benefit to ground-based remote sounding using the 265 – 280 GHz spectral region.

## 5. The effect of spectroscopic parameters

---

source of uncertainty	parameter   uncertainty	retrieved gas	error in SPÉIR profile
O <sub>3</sub> @ 273.051 GHz	position   120 kHz	O <sub>3</sub>	1% < $\sigma$ < 90%
O <sub>3</sub> @ 273.051 GHz	agam   10%	O <sub>3</sub>	2.5% < $\sigma$ < 19%
O <sub>3</sub> @ 273.051 GHz	pshift   150 Hz/Pa*	O <sub>3</sub>	1% < $\sigma$ < 33%
O <sub>3</sub> @ 278.521 GHz <sup>3</sup>	position   90 kHz	ClO	1% < $\sigma$ < 7%
O <sub>3</sub> @ 278.522 GHz <sup>3</sup>	agam   10%	ClO	2% < $\sigma$ < 28%
O <sub>3</sub> @ 278.522 GHz <sup>3</sup>	nair   10%	ClO	1% < $\sigma$ < 7%
O <sub>3</sub> @ 278.522 GHz <sup>3</sup>	pshift   150 kHz/Pa*	ClO	1% < $\sigma$ < 20%
O <sub>3</sub> @ 278.453 GHz	agam   5%	ClO	1% < $\sigma$ < 15%
N <sub>2</sub> O @ 276.328 GHz	agam   5%	N <sub>2</sub> O	1% < $\sigma$ < 12%
N <sub>2</sub> O @ 276.328 GHz	nair   10%	N <sub>2</sub> O	2% < $\sigma$ < 5%
N <sub>2</sub> O @ 276.328 GHz	pshift   150 Hz/Pa*	N <sub>2</sub> O	2% < $\sigma$ < 10%
HNO <sub>3</sub> cluster @ 269 GHz	intensity   2%	HNO <sub>3</sub>	2% < $\sigma$ < 13%
HNO <sub>3</sub> cluster @ 269 GHz	agam   10%*	HNO <sub>3</sub>	15% < $\sigma$ < 55%
HNO <sub>3</sub> cluster @ 269 GHz	nair   10%*	HNO <sub>3</sub>	4% < $\sigma$ < 13%

**Table 5.1** The uncertainties of the spectral lines and parameters identified as having the most significant effects on the retrieval of trace gas concentrations with SPÉIR. The “retrieved gas” column lists is the target gas whose retrieved profile is affected by the “source of uncertainty”. The error,  $\sigma$ , is one standard deviation. The errors listed are those which fall within the retrieval altitude range of SPÉIR. Uncertainties with a star denote those which were not listed in the spectral line catalogue, and were estimated from the literature.

---

<sup>3</sup> These lines are the same as each other, but have different positions listed in HITRAN 2008 and JPL catalogues. The position and intensity parameters are from JPL while the others are from HITRAN 2008 (see Section 4.2).

# Chapter 6

---

## 6 Ground-based observations of ozone above Kiruna

The basis of this chapter is a time series of measurements from two ground-based instruments, taken at the Swedish Institute for Space Physics (IRF), Kiruna, Sweden: the Kiruna Microwave Radiometer (KIMRA) and the Milimeter wave Radiometer 2 (MIRA 2). The installation of MIRA 2 at the same location as KIMRA provides a great opportunity for a comparison. The goal of the work was to develop operational inversion schemes that use the atmospheric spectra provided by KIMRA and MIRA 2 to retrieve O<sub>3</sub> concentrations above Kiruna, to assess the quality of these profiles through comparison with other O<sub>3</sub> measurements, and to use the O<sub>3</sub> profiles to assess the wintertime variability of O<sub>3</sub> above Kiruna. The inversion setup that was developed for this purpose can also be used for future measurements, as well as for older KIMRA data which has yet to be analysed.

The chapter is in three main parts: The first is the inversion of the KIMRA and MIRA 2 spectra, and the comparison of the respective retrieved O<sub>3</sub> profiles. The second is the comparison of each set of profiles to those from ozonesonde instruments launched from Sodankylä and from the satellite-borne instrument, the Microwave Limb Sounder (MLS). The third is a look at the variability of wintertime O<sub>3</sub> concentrations from 2008 to 2013 using KIMRA data.

The data used in the analyses presented in this chapter come from a variety of sources. Dr. Uwe Raffalski at IRF collected and provided access to the data from KIMRA and MIRA 2. Dr. Raffalski also maintains all of the observations made by KIMRA and MIRA 2 at IRF. Dr. Rigel Kivi of the Finnish Meteorological Institute, Sodankylä, provided the data from the ozonesondes which were used in the comparison with the instruments at IRF. The data from MLS were provided by the NASA Jet Propulsion Laboratory (JPL) and were accessed online through the Goddard Earth Sciences Data and Information Services Center.

## 6. Ground-based observations of ozone above Kiruna

---

The Derived Meteorological Products used for defining measurement locations with respect to the polar vortex were provided by Dr. Gloria Manney at Northwest Research Associates, and William Daffer at JPL.

### 6.1 Properties of O<sub>3</sub> Measurements

#### 6.1.1 Location

The O<sub>3</sub> measurements were made from, and maintained by IRF, Kiruna, Sweden (67.8°N, 20.4°E, 425 m elevation. See Figure 6.1). The middle atmosphere here is mostly under the conditions within the polar vortex during winter but, as Kiruna lies just inside the Arctic Circle, the vortex edge passes over from time to time. This makes the interpretation or comparison of retrieved profiles more complicated because of the high gradients in gas concentrations across the vortex edge.

#### 6.1.2 KIMRA instrument

KIMRA was developed by the Institute for Meteorology and Climate Research (IMK) at the Karlsruhe Institute of Technology (KIT) [Raffalski et al., 2002]. It has been operated in Kiruna by the Swedish Institute of Space Physics since 2002. KIMRA operates in the frequency range between 195 GHz and 233 GHz. The instrument has the capability to measure many species in this frequency range but, due to baseline issues, has only been used to measure O<sub>3</sub> and, more recently, carbon monoxide (CO). These earlier O<sub>3</sub> measurements were used for investigation of the 2002/2003 winter [Raffalski et al. 2005] and for validation of the satellite instruments: Global Ozone Monitoring by Occultation of Stars (GOMOS) [Meijer et al., 2004] and the Michelson Interferometer for Passive Remote Sounding (MIPAS) [Steck et al., 2007] on board the Envisat satellite..

The detector in KIMRA is a Schottky diode mixer cooled to ~35 K within a cryostat. It has a single sideband (SSB) noise temperature of ~1800 K. The sideband filter is a Martin Pupplott interferometer. A PLM lies in the beam path to suppress standing waves. There are two black-bodies for calibration: at ~125 K and ~293 K for the cold and hot targets, respectively. The

## 6. Ground-based observations of ozone above Kiruna

cold target is inside the cryostat. KIMRA has an acousto-optical spectrometer (AOS) with a practical bandwidth of 1.27 GHz and 1801 channels giving a resolution of  $\sim 0.7$  MHz. Problems with the outer frequency channels of the AOS prevent the use of all 2048 channels, reducing the useable bandwidth. KIMRA also has a narrowband FFTS at the back-end, operating alongside the AOS, which is centered on a nearby CO line and has been used in retrieving CO between 40 – 80 km [Hoffmann et al., 2008]. A periscope-like mirror system, with the sky mirror located in a dome on the roof of IRF, allows KIMRA to view in any direction on the sky. The elevation angle for each measurement is chosen automatically to give the highest SNR according to the tropospheric transmissivity. O<sub>3</sub> measurements are made in total power mode and the durations range from 15 min to 360 min, depending on the atmospheric conditions. A summary of the KIMRA instrument is given in Table 5.1. First technical descriptions of the instrument are given in [Raffalski et al., 2002].

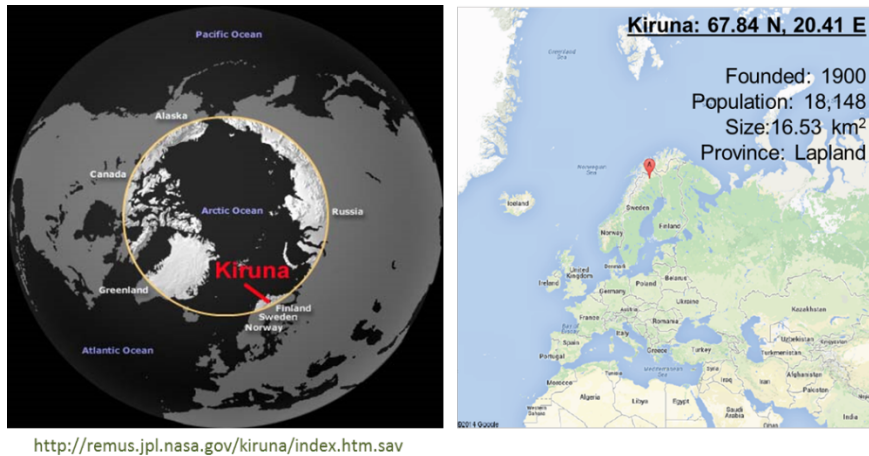


**Figure 6.1** Maps showing the location of Kiruna

### 6.1.3 KIMRA dataset

The KIMRA dataset presented here spans the time from 2008 to 2013, with some gaps in operation. The data used for intercomparison of the retrieved profiles is from 20<sup>th</sup> November 2012 to 31<sup>st</sup> May 2013, and consist of 1152 retrieved profiles. The data used in looking at the winter-time O<sub>3</sub> variability above Kiruna are from January to March over the years: 2008, 2009, 2010, 2011, and 2013. Data from January – May, 2012, were not available. Measurement data from IRF exists, with interruptions, as far back as 2002. KIMRA data used here from winter/spring 2012/2013 were chosen to overlap with MIRA 2. The January – March data for the other years

## 6. Ground-based observations of ozone above Kiruna

---

were chosen because O<sub>3</sub> above Kiruna is expected to have the most variation over this time due to chemistry and dynamics: Scientifically, this makes it a more interesting dataset to study.

KIMRA looks only directly north or south for all of these measurements. The elevation angle changes for each measurement, which prevents the averaging of spectra, so each measured spectrum is inverted and any averaging of the retrieved profiles can be applied afterwards. As a result, the SNR changes for each spectrum due to atmospheric conditions and the measurement duration. The LO is adjusted frequently (often every other measurement) in KIMRA, which gives two differing spectra to be inverted. In one case, the LO is such that the CO line at 230.535 GHz is in the spectrum (KIMRA\_O3CO measurement). In the other case, the centre frequency is shifted up by 34 MHz. This spectrum in this case is centred on the O<sub>3</sub> line and does not contain the CO line (KIMRA\_O3O3 measurement). The reason for changing the LO was to see if incorporating more of the O<sub>3</sub> line in the spectrum would cause the inversion to improve/differ. Slightly different inversion setups were needed to account for the different cases.

### 6.1.4 MIRA 2 instrument

MIRA 2 was developed at the Forschungszentrum Karlsruhe to measure O<sub>3</sub>, ClO, HNO<sub>3</sub>, and N<sub>2</sub>O between 268 and 280 GHz [Berg et al., 1998]. MIRA 2 can be considered a campaign instrument and has been housed at IRF in the past. It has recently been reinstalled in November 2012. The detector is a Shottky diode mixer cooled to ~35 K within a cryostat. The SSB noise temperature is ~800 K. The cold and hot targets are at ~80 K and ~293 K respectively. The cold target is located inside the cryostat. The sideband filter is a Martin-Pupplett interferometer. The sky mirror is contained within a removable periscope which, at IRF, sticks out through a north-facing window. MIRA 2 currently has two spectrometers at the back-end of the instrument: an AOS and an FFTS. The FFTS has a bandwidth of 0.8 GHz, and 4401 channels giving a resolution of approximately 0.18 MHz. The AOS has a bandwidth of 1.4 GHz, and 2048 channels giving a resolution of approximately 0.7 MHz. The spectra are centered on the O<sub>3</sub> line at 273.051 GHz in both cases. A PLM lies in the beam path to reduce the effect of standing waves. A more detailed description of the instrument can be found in [Berg et al., 1998]. MIRA 2 measurements have previously been used for studying the evolution of ozone-related species over Kiruna during the SOLVE/THESEO 2000 campaign [Kopp et al., 2003], and for validation

## 6. Ground-based observations of ozone above Kiruna

---

of SMR aboard the Odin satellite [Kopp et al., 2007]. A summary of the MIRA 2 instrument is given in Table 6.1.

### 6.1.5 MIRA 2 dataset

Data from the AOS were analysed because the spectrometer is the same model as the KIMRA AOS and possible differences in the spectrometers are assumed to be negligible. The dataset from MIRA 2 presented here spans 1<sup>st</sup> December 2012 to 25<sup>th</sup> April, 2013, and consists of 979 retrieved profiles. Inversions of measurements from May were originally included in the dataset but were removed because of problems with the spectra and the accompanying descriptions of the measurements: The wings of the spectra contained brightness temperature values that were orders of magnitude greater than the normal range, and the description of the data indicated south-facing measurements which would mean that instrument pointing back into the laboratory (while it is interesting to find out the O<sub>3</sub> concentration of the lab, it's not very useful for comparing to stratospheric concentrations). MIRA 2 continuously points north for all of the measurements presented here. As with KIMRA, the elevation angle of each measurement is automatically chosen to give the best SNR according to the atmospheric conditions (see Section 6.1.2).

	KIMRA	MIRA 2
<b>operation frequency</b>	231 GHz	273 GHz
<b>measurement type</b>	total power	total power
<b>detector</b>	cooled (35 K) Schottky diode	cooled (35 K) Shottky diode
<b>noise temperature</b>	1800 K	750 K
<b>sideband filter</b>	Martin-Pupplett	Martin-Pupplett
<b>standing wave suppression</b>	path length modulator	path length modulator
<b>spectrometer</b>	AOS bandwidth: 1.27 GHz resolution: 0.7 MHz	AOS bandwidth: 1.4 GHz resolution: 0.7 MHz

**Table 6.1** Summary of the KIMRA and MIRA 2 instruments when measuring O<sub>3</sub>

### 6.2 Inversion inputs and characteristics

#### 6.2.1 Forward and inverse model parameters

The forward model used for these inversions is the second release of the Atmospheric Radiative Transfer Simulator (Section 4.1): ARTS 2 [Eriksson et al., 2011]. The accompanying inversion tool is called Qpack 2, the successor to Qpack (see Section 4.1). There is some added functionality and usability to the upgraded version of the models, but there is no change in the theory that should give a difference in the following results, if one were using the earlier versions. The a priori VMR profiles used for the inversion of the KIMRA and MIRA 2 data are the Fast Atmospheric Signature Code (FASCOD) sub-Arctic winter scenario profiles [Anderson et al., 1986]. An uncertainty of 50% in the VMR profile was assumed to calculate  $\mathbf{S}_a$  (see Section 4.1). The temperature and pressure information ( $z p T_s$ ) up to 50 km is from daily NCEP profiles, and above that is the U.S. Standard atmosphere. The forward model pressure grid is 200 layers, evenly spaced in altitude between ground level and approximately 100 km. The retrieval pressure grid is 45 layers, evenly spaced in altitude between ground level and approximately 90 km. The retrieved quantity is the fractional VMR, the VMR of the target gas as a fraction of the a priori for that gas. A polynomial of order three is included in the inversion and is fitted to each spectrum to account for some of the standing wave signal in the baseline. The inversions are nonlinear and a Marquardt-Levenberg iterative root-finding method is used with Qpack 2. The convergence criteria are the same for inversions of KIMRA and MIRA 2 data.

Attenuation of the signal due to the troposphere is accounted for by including the MPM93 [Liebe et al., 1993] H<sub>2</sub>O continuum in the inversion (see Section 2.4.2). The spectroscopic parameters are taken from the HITRAN 2008 catalogue. Estimates for the thermal measurement noise on each spectrum are obtained by fitting a second order polynomial to a relatively flat part of the spectrum (covering 400 channels), and calculating the error on the fit. This value is used to calculate the measurement noise covariance matrix,  $\mathbf{S}_e$  (Section 2.4.2). Error contributions from other instrumental and model parameters have previously been assessed for KIMRA and MIRA 2 using OEM and so they have not been repeated here. For KIMRA, the uncertainty in the retrieved profiles due to standing waves and systematic errors amounts to at least 1 ppmv [Kopp, 2001]. For MIRA 2, an uncertainty of at least 1 ppmv is caused by errors due to

standing waves, systematic errors, and thermal noise [Kopp, 2000]. ARTS 2 has the capability to store the calculated absorption coefficients in a lookup table. The advantage of this is that the forward model does not have to recalculate the coefficients for each iteration of the inversion process. Details on the implementation of the absorption coefficient lookup table in ARTS 2 can be found in [Buehler et al., 2011]. Values for interpolation orders used for the lookup table are those recommended (default values) in this reference. An absorption lookup table is calculated once for each day of measurements as the zpT files are daily. They are calculated separately for each instrument as the operating frequencies differ.

### 6.2.2 Example fits and properties of the retrieved states

Examples of fits to the data for a KIMRA\_O3CO measurement and a MIRA 2 measurement are shown in Figure 6.2. It is clear that there are substantial standing wave features in the spectra and the residua (KIMRA\_O3O3 spectra show the same feature). There are some relatively short-length standing wave signals in both the KIMRA and MIRA 2 data which would require the inclusion of a large order polynomial in the spectrum. Polynomial orders up to nine were tried but no appreciable difference was found in the results. Since some oscillations were apparent in the retrieved profiles, it was decided to increase the estimate of the noise on the spectrum by a fixed amount, different for each instrument. The offset was estimated based on the amplitude of the standing waves but the final value was found by adjusting the offset until oscillations were not clearly visible in the retrieved O<sub>3</sub> profiles. These oscillations are assumed to be due to the inversion fitting the short-scale standing wave features in the spectra, and while not clearly visible in a single profile, the results of the following sections show that effect of the standing waves is still present in the retrieved profiles.

The mean averaging kernels, measurement response, and altitude resolution (see Section 4.3.2) for the retrieved profiles for each instrument are shown in Figure 6.3. The actual averaging kernels, and quantities derived from them, will vary for each measurement depending mainly on the SNR of the spectrum. The retrieval altitude range is chosen as altitudes that have a measurement response higher than 0.8, giving a range of approximately 16 – 54 km. The altitude resolution is at best 8 km, and begins to degrade quickly above 40 km altitude. The values

## 6. Ground-based observations of ozone above Kiruna

---

found here are very similar to previously shown values for these instruments. The DOFS over the retrievable altitude range for the retrieved states are approximately 4 for each instrument.

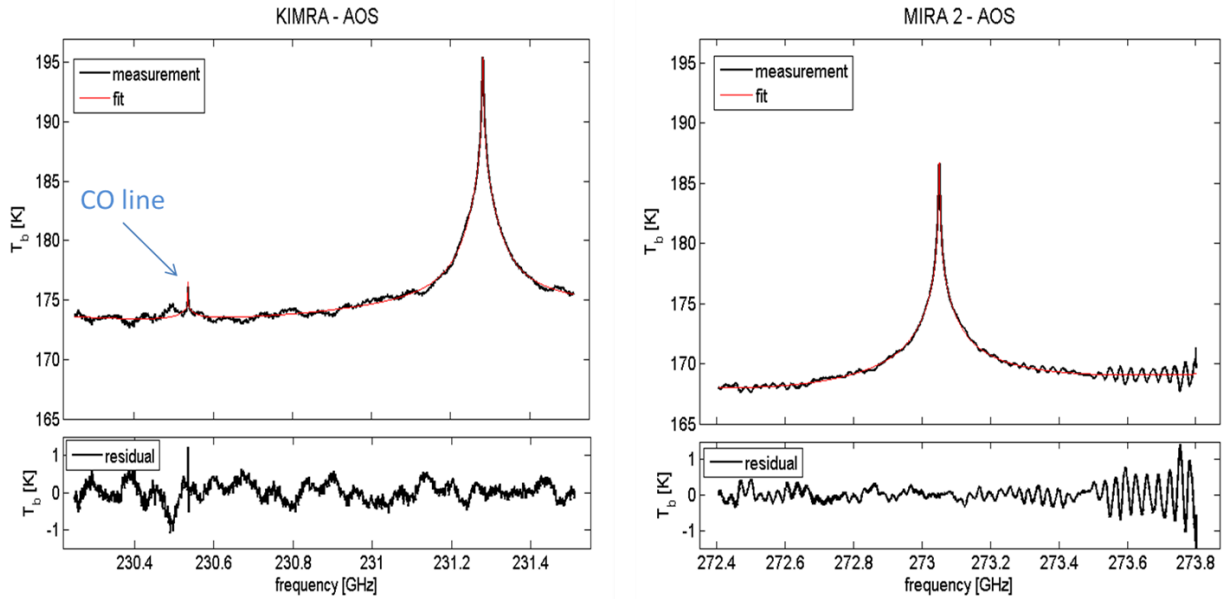


**Figure 6.2** Example spectra and fits for a KIMRA\_O3CO measurement and a MIRA 2 measurement.

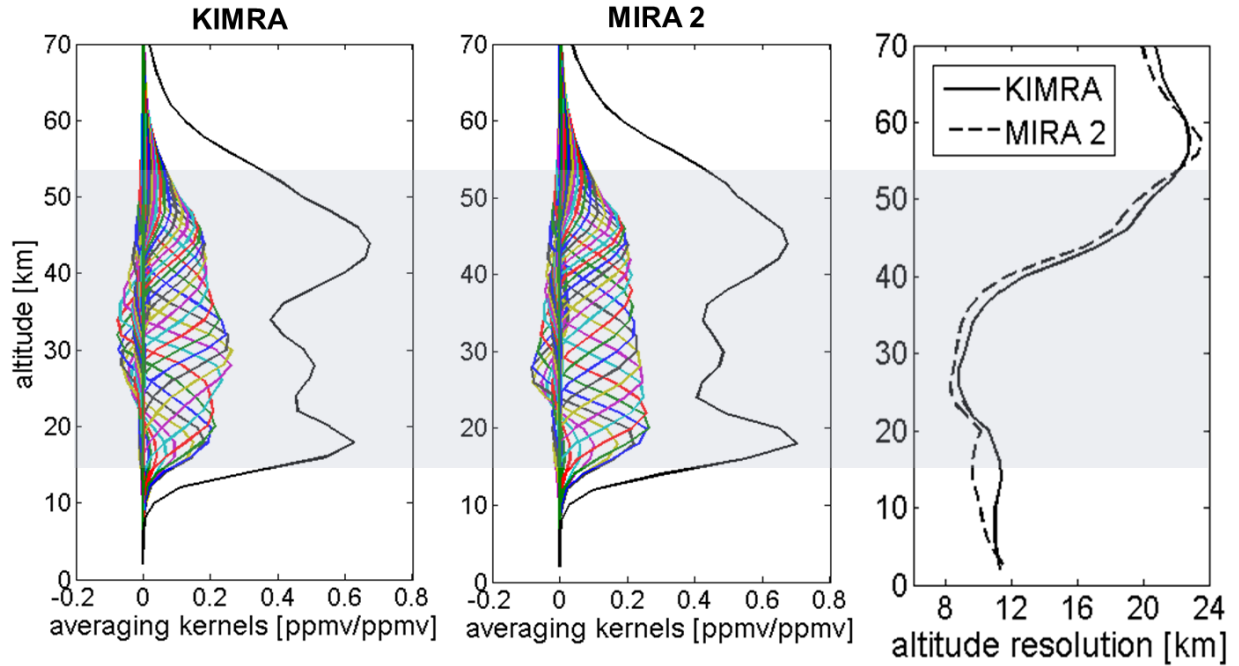


**Figure 6.3** Left and middle: mean averaging kernels for KIMRA and MIRA 2 O<sub>3</sub> retrieved profiles used for the comparison. The measurement response divided by 2 is also shown as the solid black line. Right: the altitude resolution of the profiles, given by the FWHM of the averaging kernels. The shaded area represents altitudes with a measurement response greater than 0.8.

### 6.3 Comparison of KIMRA and MIRA 2

#### 6.3.1 Coincidence criteria

Since MIRA 2 always points north (when not looking back into the lab), only north-facing KIMRA measurements were used for this comparison. The elevation angle of the measurement does not matter with regards to comparison as the instruments are located in the same place and the atmosphere is assumed to be one-dimensional for an inversion. The measurement time and duration were used as follows to determine which profiles to compare to each other: For a given KIMRA measurement, it was determined whether there are any MIRA 2 measurements whose midpoint in measurement time lies within the duration of KIMRA's measurement. If so, it was determined which measurement has a longer duration (say it was MIRA 2). Then it was checked whether there were any more KIMRA measurements that also had a midpoint that lay within the duration of the MIRA 2 measurement. If so, the KIMRA profiles from all of these measurements were averaged to produce a single profile that was considered coincident with the corresponding MIRA 2 profile. If not, the two single profiles were considered coincident. This method compares profiles from measurements that overlap in time, and avoids using any measurement twice. 177 coincident sets were identified for the following comparison. A histogram of the time differences between the midpoints of coincident measurements is shown in Figure 6.4. The majority of the differences are less than 1 hour. Measurement times for the instruments range from 15 minutes to 4 hours, with a mean time of approximately 1 hour.

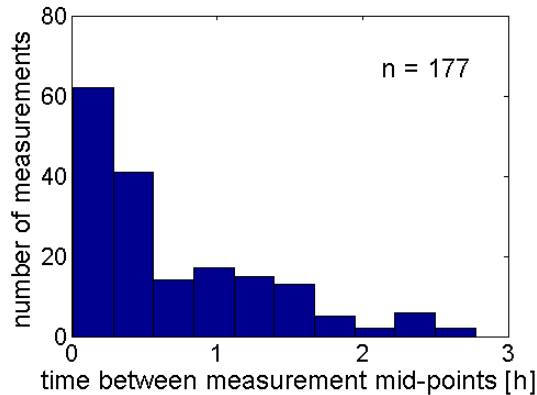


**Figure 6.4** Histogram of the time difference between coincident measurements of KIMRA and MIRA 2 between December 2012 and April 2013.

### 6.3.2 Results of KIMRA and MIRA 2 comparison

The O<sub>3</sub> profiles are retrieved on a fixed pressure grid and so the corresponding altitudes for each grid-point differ a little from day to day. For comparisons, all profiles are interpolated onto a fixed altitude grid: 2 – 90 km with 2 km spacing between layers. Figure 6.5 shows the comparison of coincident KIMRA and MIRA 2 O<sub>3</sub> profiles for December 2012 to April 2013. Both average profiles are essentially lower than the a priori VMR except for values below about 18 km. The mean difference (KIMRA – MIRA 2) in the profiles shows an oscillatory structure that is largely within the limits of the measurement error (summed measurement error from KIMRA and MIRA 2). The largest difference, which falls outside the measurement error range, is a negative value peaking at –1.1 ppm at 22.5 km. The standard deviation of the differences is largest between 26 km and 34 km. There is a strong correlation of the VMR values (>0.95) above 35 km. This drops to about 0.85 at 30 km and then drops rapidly to a peak below 0.5 at 26 km. Within 17 – 24 km the correlation is above 0.70 before dropping to ~0.50 at the lower retrieval limit.

Since there are approximately 4 DOFS for each measurement, the O<sub>3</sub> profiles were split into four altitude regions and the total O<sub>3</sub> concentration (in molecules per cm<sup>2</sup>) calculated for each region corresponding to four O<sub>3</sub> partial columns. The column densities were calculated using the temperature profiles from the zpTs and the ideal gas law. The altitude ranges of the four partial columns are: 16 – 26 km, 26 – 36 km, 36 – 46 km, and 46 – 56 km (the numbers are the centres of the retrieval grid layers). Each region corresponds to approximately 1 DOFS. The correlations of the O<sub>3</sub> partial column concentrations were calculated and a line of best fit was determined for each column. The fit was determined using a linear regression for data with errors in both the X and Y variables, following [York et al., 2004]. The results are plotted in Figure 6.6. The poorest correlation/fit is for the lowest partial column: the fit has a slope of 0.81 and an offset on the order of the average partial column concentration, and the correlation is 0.87. The best correlation/fit is for the 36 – 46 km partial column: the fit has a slope of 1.0 and an offset one magnitude lower than the average partial column concentration, and the correlation is 0.97. The most variability in the differences is seen for the lowest altitude partial column. This corresponds to the altitude region where KIMRA has a relatively large low bias with respect to MIRA 2.

## 6. Ground-based observations of ozone above Kiruna

---

With just the data from these two instruments, it is very difficult to diagnose the reason for the bias, however, the oscillatory structure in the mean difference is present in all of the individual difference profiles: see Figure 6.7. This suggests a systematic error. It is reasonable to assume that this error is arising from the clear standing wave signals present in the spectra (see Figure 5.2). Basic studies on the effects of standing wave signatures on O<sub>3</sub> spectra have been performed for SPÉIR, and the result is an oscillatory structure in the retrieved VMR profile. Standing wave signals in the baseline that have a scale similar to that of the lineshape are the most difficult to separate from the sky signal, especially if the standing wave is symmetric about the line centre. For this reason, it is assumed that the standing wave signal in the KIMRA measurements will have more of an impact on the retrieved O<sub>3</sub> state than the standing wave signals in the MIRA 2 spectra, which have a shorter scale in frequency space. Part of the variation in the differences in Figure 6.7 would also be explained by standing waves as the cause. The reasoning is as follows: The retrieved ozone state is affected by the opacity of the atmosphere. If some of the standing wave in the spectrum is incorrectly attributed to a concentration of ozone at some altitude in the atmosphere, then that contribution to the retrieved state will also vary depending on the atmospheric opacity. A higher opacity will mean that the inversion attributes a greater atmospheric concentration to the standing wave signal in the spectrum. Another possible source of the oscillatory bias could be an error in the air broadening parameter (see Section 2.2.2.2) for the O<sub>3</sub> line at 231 GHz, but it was not checked how changing this parameter would affect the retrieved profile.

## 6. Ground-based observations of ozone above Kiruna

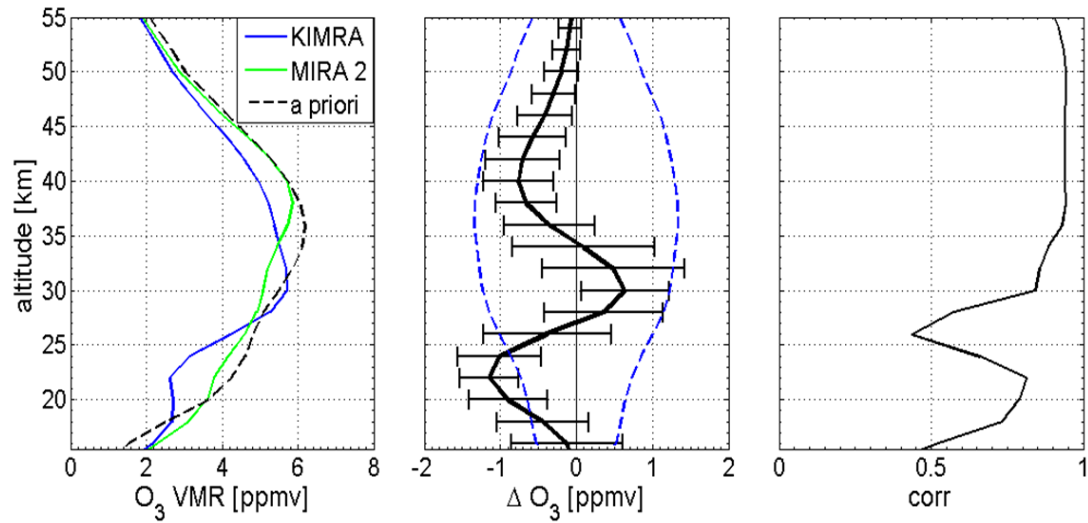


**Figure 6.5** Left: the average of the 177 coincident  $O_3$  profiles for KIMRA and MIRA 2 and the a priori for the inversions. Middle: the mean of the difference (KIMRA – MIRA 2) in coincident profiles (black) with  $\pm$  the standard deviation as the error bar. Also shown is the sum of the average KIMRA and MIRA 2 measurement error (dashed blue). Right: the correlation of the coincident pairs at each altitude.

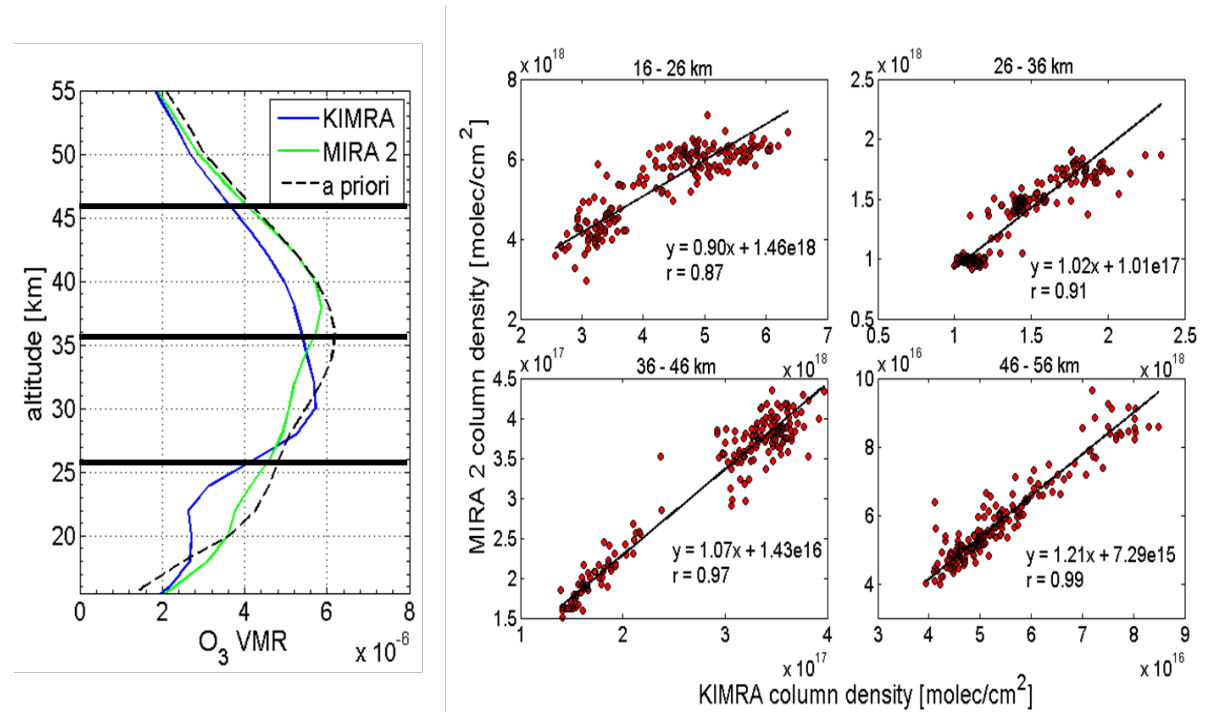


**Figure 6.6** Left: same as left plot in Figure 6.5 but with markers showing the altitude separation of the partial columns. Right: scatter plot of the partial columns of coincident KIMRA and MIRA 2 data, including a line of best fit. The correlation for each of the sets of partial columns is also shown.

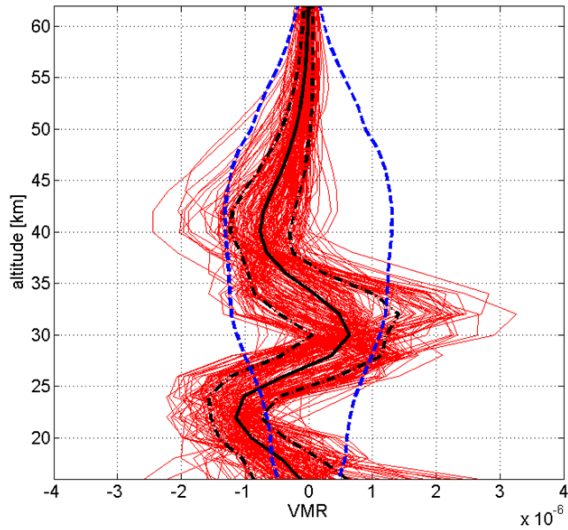


**Figure 6.7** Difference of individual  $O_3$  VMR profiles (KIMRA – MIRA 2, red) showing the persistent oscillatory structure. The mean is also shown in black with  $\pm$  the standard deviation in dashed black. The sum of the average measurement errors for each instrument is shown in dashed blue.

## 6.4 Comparison with ozonesondes and MLS

### 6.4.1 Ozonesondes at Sodankylä

KIMRA and MIRA 2  $O_3$  profiles were compared to profiles from ozonesondes launched by the Finnish Meteorological Institute at Sodankylä, Finland ( $67.37^\circ N$ ,  $26.63^\circ E$ ). The location of the launches is a good site for a comparison as it has a similar latitude to IRF, at  $67.84^\circ N$  (see Figure 6.8), and the meridional gradient of  $O_3$  tends to be greater than the zonal gradient. 31 ozonesonde measurements were provided for this study. The data are from between 31<sup>st</sup> October 2012 and the 29<sup>th</sup> May 2013, and the sondes were launched approximately once per week. The instruments are electrochemical concentration cell (ECC) sondes, using a potassium iodide (KI) solution, and the sounding software is DigiCORA III, from Vaisala. The partial pressure of  $O_3$  is calculated according to an electrical current produced by the reaction between  $O_3$  and  $I^-$ . The pressure and temperature reading of the sondes are corrected for ground level values before they are launched [Calisesi et al., 2003]. More details on the ozonesonde instrument can be found in [Kivi et al., 2007]. The sondes used in this work have a range of maximum measurement altitudes from 18 km to 34 km.



**Figure 6.8** Map showing the location of Sodankylä ( $67.4^{\circ}$  N,  $26.6^{\circ}$  E) with respect to Kiruna ( $67.8^{\circ}$  N,  $20.4^{\circ}$  E): ~19 hours by bike.

### 6.4.2 Aura Microwave Limb Sounder

The Microwave Limb Sounder (MLS) is one of four instruments aboard the Aura satellite. The satellite is part of the National Aeronautics and Space Administration's (NASA) Earth Observing System. Aura was launched on July 15<sup>th</sup> 2004 and is in a near-polar orbit at 705 km with measurements being made 24 hours a day. Aura stays fixed relative to the Sun and orbits the planet approximately 14.5 times per day, giving 240 scans per orbit and nearly 3500 profiles per day from MLS. The MLS scans are synchronised to the orbit and measurements are at approximately the same time at the same latitude each day, spaced in distance by roughly 165 km on the suborbital track. The instrument views across the limb of the planet, which is beneficial for vertical resolution of the retrieved profiles. Measurements are made of the thermal emission in relatively broad frequency bands centred near 118, 190, 240, 640, and 2500 GHz, and are calibrated after every 25 s scan. The O<sub>3</sub> measurements are made using the spectral lines in the 240 GHz band. More details on the instrument and observation technique are found in [Waters et al., 2006]. The most recent version of the level 2 data, v3.3/v3.4, was used in the work here [Livesey et al., 2013]. Gas concentrations are retrieved on a 55-layer pressure grid. The ozone profiles have a vertical resolution of ~3 km from 261 – 0.2 hPa, and 4 – 5.5 km from 0.1 to 0.02 hPa. These levels cover the “useful range” of the data quoted by the MLS team [Livesey et al., 2013]. The precision of the measurements is ~0.04 ppmv from 215 – 46 hPa,

## 6. Ground-based observations of ozone above Kiruna

---

0.1 – 0.5 ppmv from 22 – 0.1 hPa, 1.4 ppmv from 0.05 – 0.02 hPa. The validation of v2.2 data has been documented in [Jiang et al., 2007; Froidevaux et al., 2008; Livesey et al., 2008].

### 6.4.3 Coincidence criteria

Time, distance, and position relative to the polar vortex were the criteria used in determining which individual profiles to compare, and are described here for each instrument. The location of a measurement with respect to the polar vortex was determined using scaled potential vorticity values (see Section 2.1.3) provided by Dr. Gloria Manney at NorthWest Research Associates and William Daffer at JPL. Both the north and south pointing measurements from KIMRA are used in the following comparisons.

The general procedure for ozonesondes vs. KIMRA/MIRA 2 and MLS vs. KIMRA/MIRA 2 was as follows: For a given ozonesonde/MLS measurement, a maximum limit on the difference in time between measurements was used to choose a group of possible KIMRA/MIRA 2 measurements with which to compare. This group was reduced to those measurements which were in the same location as the ozonesonde/MLS measurement, relative to the polar vortex (inside vortex/outside vortex/in vortex edge). From this new group, the closest measurement in space, using distance along a great circle, was chosen as the measurement for comparison. Each KIMRA/MIRA 2 measurement was only used once in a comparison with another instrument.

For MLS, a maximum time difference of  $\pm 4$  hours between measurements was used. A small time limit was preferred, and it was decided that less than 4 hours produced too few coincidences, while more than 4 hours did not make a significant difference to the number of coincidences. Either way, the choice of time criterion did not have a substantial effect on the presented results (there was a slight increase in standard deviation). For the distance criterion, the closest measurement in space had to lie within a given latitude and longitude box:  $\pm 2^\circ$  latitude and  $\pm 10^\circ$  longitude.  $\pm 5^\circ$  was also tried for the longitude criterion but it halved the number of coincidences and made no significant difference to the results. The altitude at which the distance between measurements was calculated was 34 km. The reason for the choice is that this altitude coincides approximately with the peak in the O<sub>3</sub> VMR profile above Kiruna, and it is

## 6. Ground-based observations of ozone above Kiruna

---

also approximately the middle of the retrievable altitude range for the ground-based instruments.

For the ozonesondes, no criterion was placed on the measurements with respect to their distance from KIMRA/MIRA 2 measurements. It is assumed that the location of the measured O<sub>3</sub> profiles is directly above the launch station in Sodankylä. For the time criterion, the closest KIMRA/MIRA 2 measurement within 24 hours was used to compare to the ozonesonde profile. As the sonde profiles have differing maximum altitudes, the resulting comparisons have different numbers of coincident points for different altitudes.

For the ozonesonde comparison, the criterion for sPV was applied at an altitude of 18 km, for the following reasons: 18 km is the lowest maximum altitude of the used sondes, so it is the only altitude which is common to every sonde. Also, the choice of sPV altitude was found to have little effect on the results of the VMR comparison. More of an effect was seen for the partial column density comparison, but the quality of the VMR profile is of most interest here. The altitude used for the sPV criterion for the MLS comparisons was 34 km, the same as that used for the distance criterion, explained above.

Both the ozonesonde and MLS profiles were smoothed with the averaging kernels of the coincident KIMRA/MIRA 2 measurements before they were compared so that the profiles would have similar resolution. The effect of excluding O<sub>3</sub> measurements in the edge of the vortex was looked at for each comparison and discussed in the following section.

### 6.4.4 Results of comparison with ozonesondes and MLS

#### 6.4.4.1 Ozonesondes

Figure 6.9 shows the results of the comparison of O<sub>3</sub> profiles from ozonesondes and KIMRA and MIRA 2. The measurement error for the ozonesondes is neglected and the profiles are assumed to be the true O<sub>3</sub> concentrations above Sodankylä. MIRA 2 shows a closer match to the ozonesondes than KIMRA. KIMRA shows a negative bias with respect to the ozonesondes in general. The mean of the difference in the profiles has an oscillatory structure with altitude. The largest bias for KIMRA, larger than the measurement error, is at ~17 – 25 km, and peaks at -1.8 ppmv. The standard deviation of the differences is also large: ~1 ppmv at some altitudes.

## 6. Ground-based observations of ozone above Kiruna

There is less variability in the differences between the ozonesondes and MIRA 2 and the bias is less than 1 ppmv except at the highest altitude. Figure 6.10 and Figure 6.11 show the partial column densities of the ozonesondes and the respective coincident measurements for KIMRA and MIRA 2. The densities for KIMRA and MIRA 2 data were calculated as in Section 6.3.2, but the column heights were chosen to match the maximum heights of the coincident ozonesondes. The densities for the ozonesonde data were calculated using the smoothed O<sub>3</sub> profiles and the temperature measurements made by the sondes during their flight. The KIMRA column densities are consistently less than those for the ozonesondes, as expected from the low bias in the profiles. A linear regression was performed assuming that the sonde data is true. The line of best fit to a scatter plot of the KIMRA and sonde data gives a relatively small slope of 0.44, and a correlation coefficient of 0.85. For MIRA 2, the slope of the line of best fit is 0.75 and there is a high correlation coefficient of 0.98.

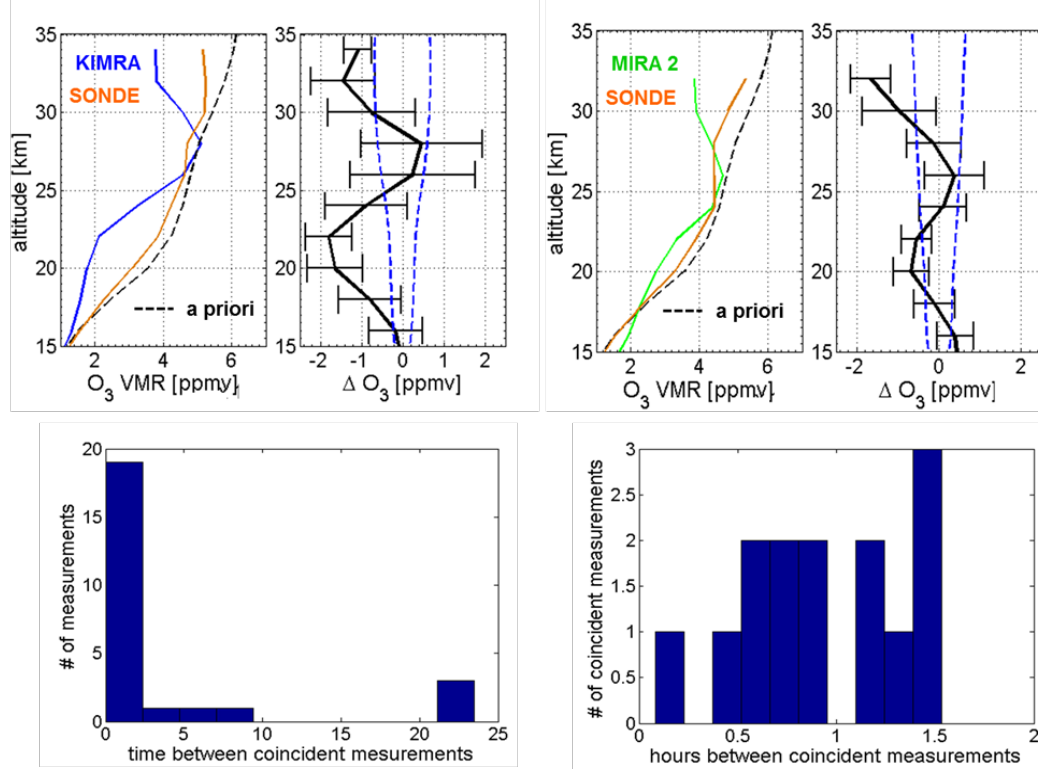


**Figure 6.9** Upper left: the mean O<sub>3</sub> profiles for 25 coincident KIMRA and smoothed Sodankylä ozonesonde measurements. The mean of the difference (KIMRA - sonde) in the profiles is shown on the right (solid black) with the standard deviation as the error bars. The average measurement error for KIMRA is also plotted (dashed blue). Lower left: a histogram of the time difference between coincident measurements. Upper/Lower right: the same but for MIRA 2 and Sodankylä ozonesondes (14 coincident profiles).

## 6. Ground-based observations of ozone above Kiruna

---

Figure 6.12 shows the sPV value for measurements of each instrument at altitudes of 18, 24, and 30 km. The similarity of the sPV for the ground-based instruments and the ozonesondes confirms Sodankylä as a good comparison site for Kiruna. Most likely due to the location of Kiruna and Sodankylä, the variability of sPV between altitudes shows that the measurements are sometimes simultaneously detecting O<sub>3</sub> concentrations from inside, outside, and within the edge of the polar vortex, depending on the respective altitudes. This makes life more difficult for comparing measurements. Since the largest concentration gradients lie within the vortex edge, the results were examined to see whether it made a difference if all O<sub>3</sub> profiles which lie in this region ( $1.2 \times 10^{-4} \text{ s}^{-1} < \text{sPV} < 1.6 \times 10^{-4} \text{ s}^{-1}$ ) were excluded. Little difference was found in the bias for the VMR profiles but the standard deviation of the difference was decreased for a few altitudes, while the agreement in the partial columns improved in both cases. The number of coincidences dropped from 25 to 17 for KIMRA. The partial column correlation increased from 0.85 to 0.86, and there was no change to the slope of the line of best fit. The change for MIRA 2 was more dramatic: the number of coincidences dropped from 14 to 7. The partial column correlation increased from 0.98 to 0.99, and the slope of the line of best fit changed from 0.75 to 0.89. Although there are only 7 coincidences, these numbers indicate excellent agreement in the MIRA 2 and ozonesonde partial columns.

## 6. Ground-based observations of ozone above Kiruna

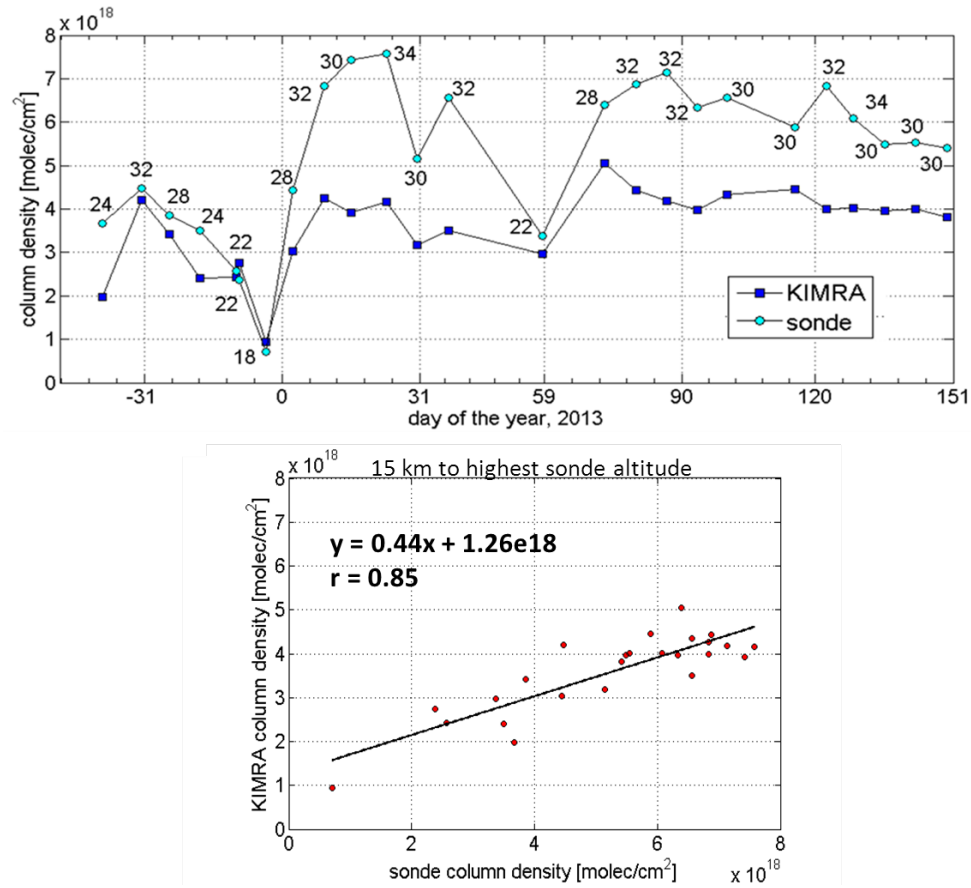


**Figure 6.10** Upper: partial column densities of O<sub>3</sub> from KIMRA and from smoothed Sodankylä ozonesonde measurements, from November 2012 to May 2013. The numbers beside the points show the maximum altitude (in km) of each partial column, determined from the maximum altitude of the ozonesonde measurements. The minimum altitude is 15 km. Lower: scatter plot of the KIMRA columns against the ozonesonde columns. The line of best fit is shown with the accompanying equation and correlation coefficient. The data has not been filtered by position relative to the polar vortex.

## 6. Ground-based observations of ozone above Kiruna

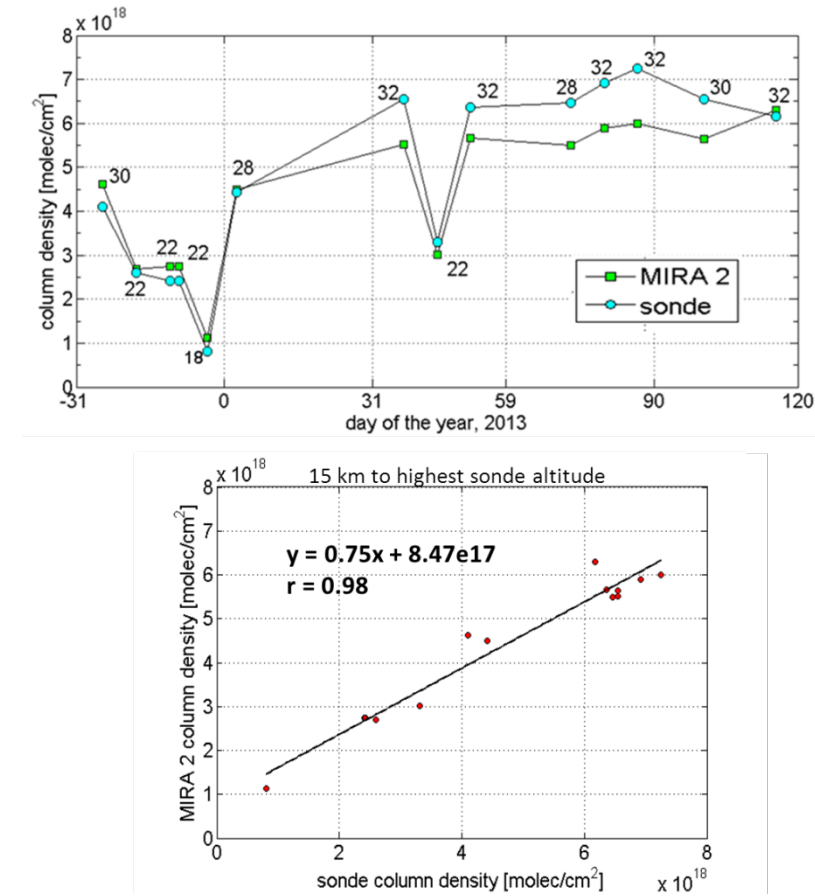


**Figure 6.11** The same as Figure 5.9, but for MIRA 2 and Sodankylä ozonesonde measurements.

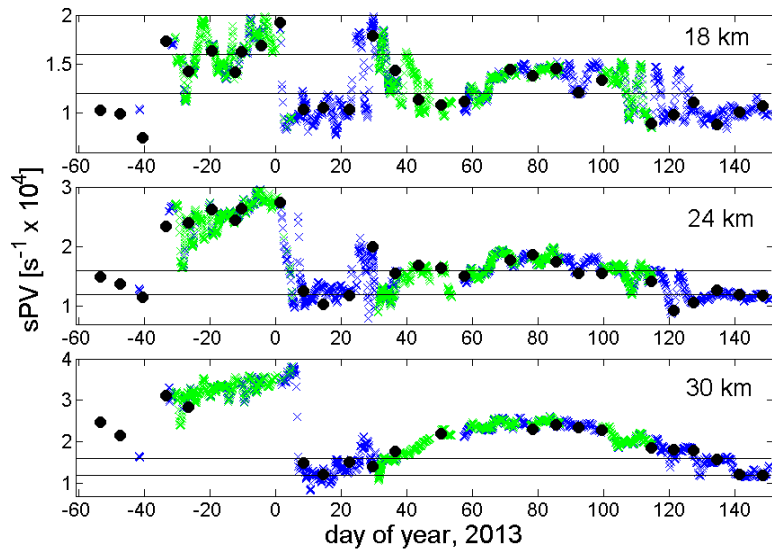


**Figure 6.12** The sPV value corresponding to the measurement locations of KIMRA (blue cross), MIRA 2 (green cross), and Sodankylä ozonesondes (black dot), at altitudes of 18, 24, and 30 km. Lines of sPV values of  $1.2$  and  $1.6 \times 10^{-4}$  s<sup>-1</sup>, respectively defining the outer and inner edge of the polar vortex, are also shown.

### 6.4.4.2 MLS

Results of the comparison with MLS are shown in Figure 6.13 for KIMRA and in Figure 6.14 for MIRA 2 for the period of December 2012 to May 2013. There are 359 coincident measurements for KIMRA and 361 coincident measurements with MIRA 2. Above 35 km, KIMRA has a good agreement with MLS with a consistent low bias of 0.3 ppmv. Below that, the oscillatory bias seen in the other comparisons (e.g., Figure 6.5 and Figure 6.9) is present, with max./min. of approximately +/- 1 ppmv. The steep drop in the correlation for KIMRA is also seen again (Figure 6.5) at approximately 26 km. MIRA 2 shows better agreement with MLS. There is a general high bias with an oscillatory structure peaking at approximately 0.6 ppmv at the lowest retrievable altitude for MIRA 2. The bias  $\pm$  the standard deviation of the differences is almost completely within the range of the sum of the measurement errors from MLS and MIRA 2. The correlation is above 0.9 for altitudes above 35 km and drops to about 0.7 at the lowest retrieval altitude range of MIRA 2.

In the time series comparisons in Figure 6.15 and Figure 6.16, the profiles are split into four partial columns corresponding to the same altitude ranges as in Figure 6.6. The partial columns for MLS were calculated using the MLS temperature measurements that are coincident with the MLS O<sub>3</sub> measurements. There is a clear increase in the column densities at the beginning of January for the KIMRA and MLS columns (although not as clear for the lowest column: 16-26 km). Lines of best fit were calculated accounting for errors in X and Y; again, a better correlation, fit, and variance are found for the MIRA 2 comparison than for the KIMRA comparison. The highest variance in the KIMRA measurements is seen in the lowest altitude partial column. Figure 6.17 shows the sPV values at 34 km for all KIMRA and MIRA 2 measurements, and all coincident MLS data. One can see that most of the KIMRA and MIRA 2 measurements that lie within the edge of the polar vortex were removed from the comparison by the vortex criterion (see Section 6.4.3) because MLS was not measuring inside the vortex at this altitude, and removing the remaining data that lay in the edge of the polar vortex made no significant difference to the results.

## 6. Ground-based observations of ozone above Kiruna

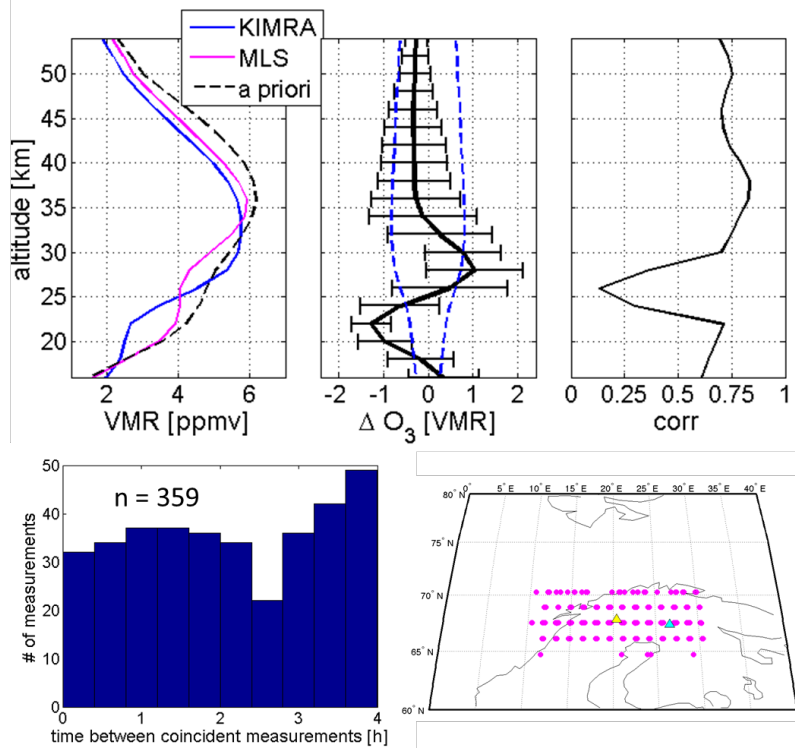


**Figure 6.13** Upper row: the same as for Figure 6.5, but for KIMRA minus MLS. Lower left: histogram of the time difference between coincident measurements. Lower right: map showing the locations of the coincident MLS measurements (magenta circles), Kiruna (yellow triangle), and Sodankylä (cyan triangle).

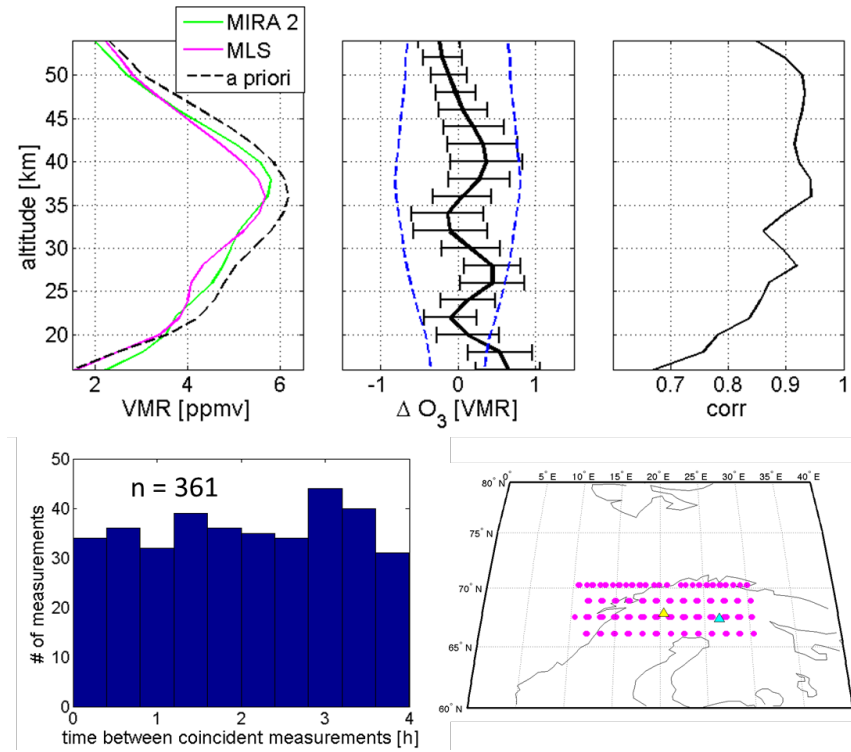


**Figure 6.14** The same as Figure 6.13, but for MIRA 2 minusMLS.

## 6. Ground-based observations of ozone above Kiruna

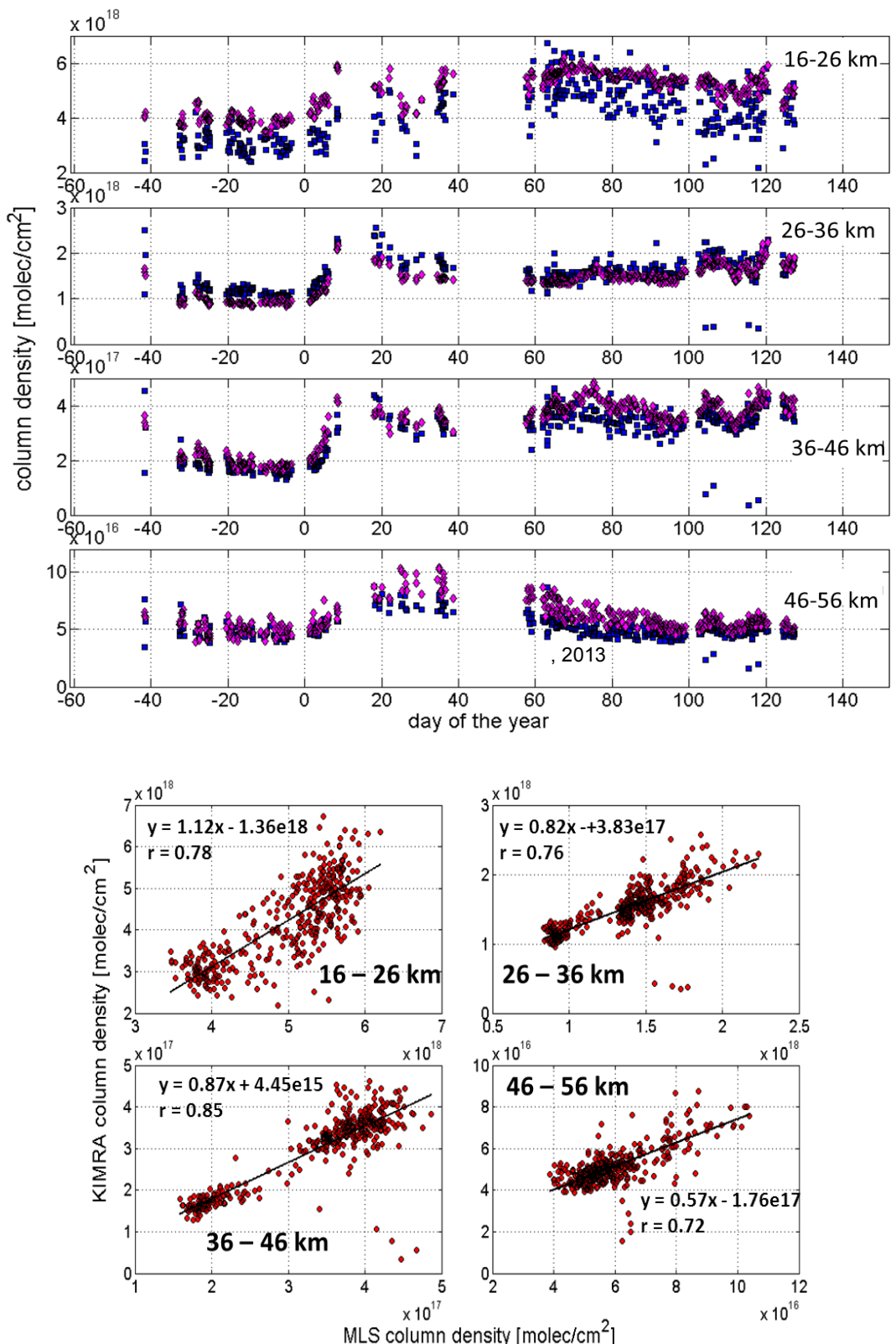


**Figure 6.15** Upper: the O<sub>3</sub> partial column densities from KIMRA (blue squares) and MLS (magenta diamonds) measurements plotted against time. Lower: scatter plots of the corresponding coincident data. Lines of best fit and correlation coefficients are shown.

## 6. Ground-based observations of ozone above Kiruna

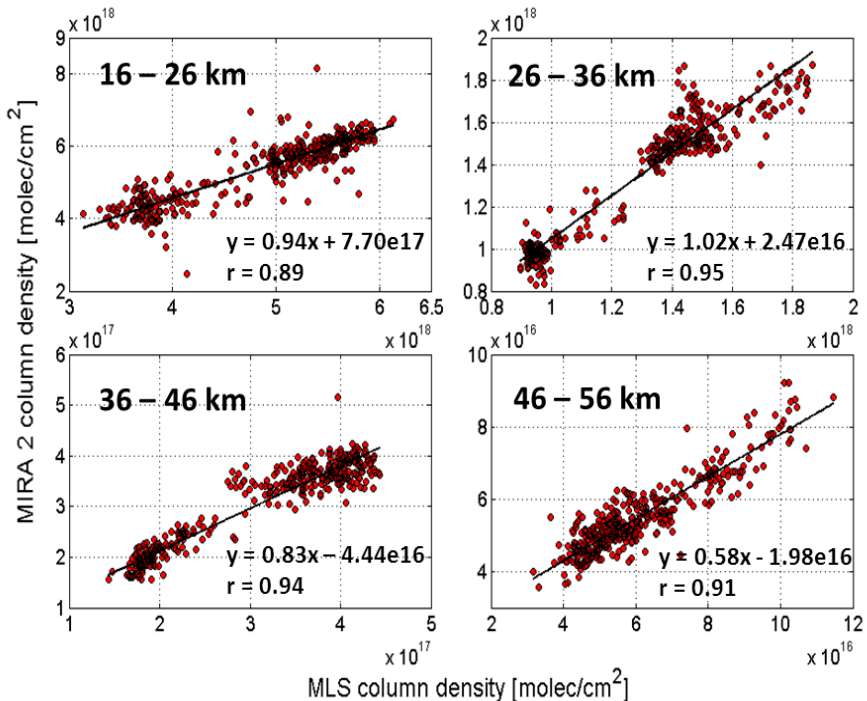
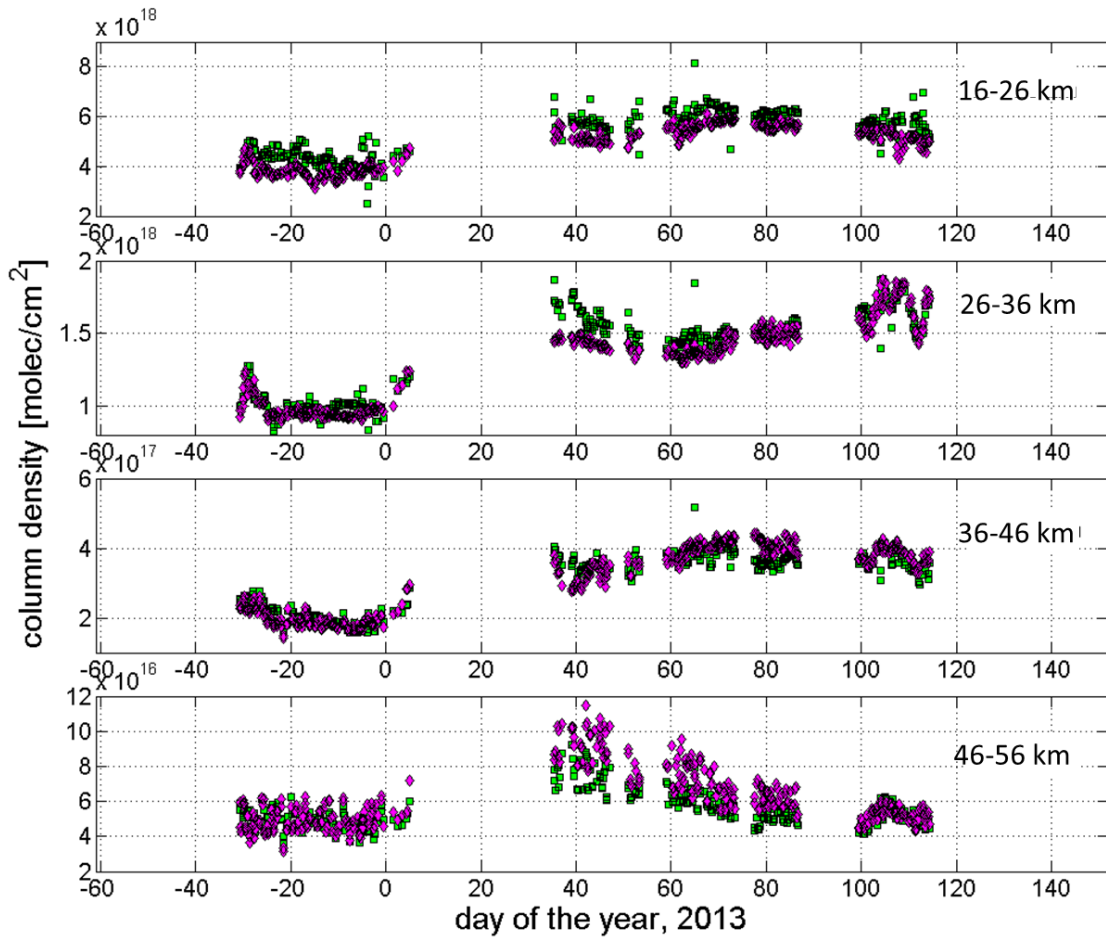


**Figure 6.16** Same as Figure 6.15, but for MIRA 2 (green squares) and MLS (magenta diamonds).

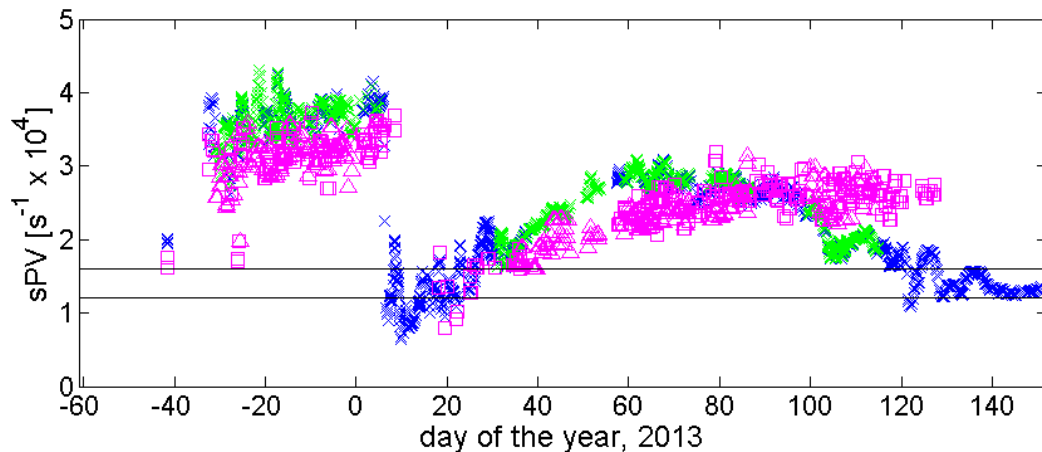


**Figure 6.17** sPV values at 34 km at the location and time of all KIMRA measurements (blue cross), and coincident MLS measurements (magenta square). The same is shown for all MIRA 2 measurements (green cross) and coincident MLS measurements (magenta triangle).

### 6.5 Daily variability in winter-time ozone above Kiruna

This section moves on from the comparisons into a look at the local variability of O<sub>3</sub> above Kiruna using data from KIMRA. Only KIMRA data is used because of the longer data record length at Kiruna. Section 6.5.1 uses data from KIMRA and MIRA 2 to make the point of differentiating between the clear oscillatory bias that was found in the KIMRA O<sub>3</sub> profiles with respect to other instruments (seen in the previous sections of Chapter 5), and what will be referred to as an “O<sub>3</sub> dip”. The O<sub>3</sub> dip is a local minimum in the winter-time stratospheric O<sub>3</sub> profile that is shown in Section 6.5.2 to be a consistent feature in multiple years of data. It will be assumed from this point on that the KIMRA O<sub>3</sub> data has a low bias of 1 ppm at ~22 km and a high bias of 1 ppm at ~28 km, each maximum with a half-width of ~5 km.

Altitude was so far used as the primary coordinate in the chapter, because data from the ozonesondes and from MLS were interpolated onto the KIMRA/MIRA 2 retrieval grid and it was found to be easier to use altitude ranges when illustrating differences between the profiles. The KIMRA data here is presented primarily on a pressure scale with approximate altitudes provided. Daily averages of the data are used to look at the day-to-day variability of O<sub>3</sub> above Kiruna.

### 6.5.1 2012/2013 data

The O<sub>3</sub> profiles from all the KIMRA and MIRA 2 measurements between November 2012 and May 2013 were averaged by day (MIRA 2 data from May was excluded: see Section 6.1.5). The daily averages are plotted against time in Figure 6.18. Both datasets show a similar evolution of O<sub>3</sub> over the winter: the generally low stratospheric O<sub>3</sub> concentration in December, a rapid increase in early January, and a movement of high O<sub>3</sub> concentration air, by about 10 km down in altitude, through March and April. The differences in the profiles, found in Section 6.3.2, can also be seen: The low bias in KIMRA O<sub>3</sub> at ~22 km (50 hPa) is apparent, and also the high bias at ~ 28 km (14 hPa), most easily noticeable in December. The difference in the profile values around 40 km is attributed to a high bias of ~ 0.5 ppm in the MIRA 2 data at this altitude: This conclusion is reached by comparing the differences in the KIMRA and MIRA 2 data (Figure 6.5) as well as their respective differences with MLS (Figure 6.13 and Figure 6.14).

It is important for the following section to see that the apparent “dip” in the O<sub>3</sub> profile, which one can see in January and February between approximately 28 and 38 km, is present in each dataset and is not a result of the oscillatory structure in the KIMRA dataset. The high bias in KIMRA O<sub>3</sub> at ~28 km may make this dip more pronounced, but the low bias in KIMRA O<sub>3</sub> occurs at a lower altitude: ~ 22 km.

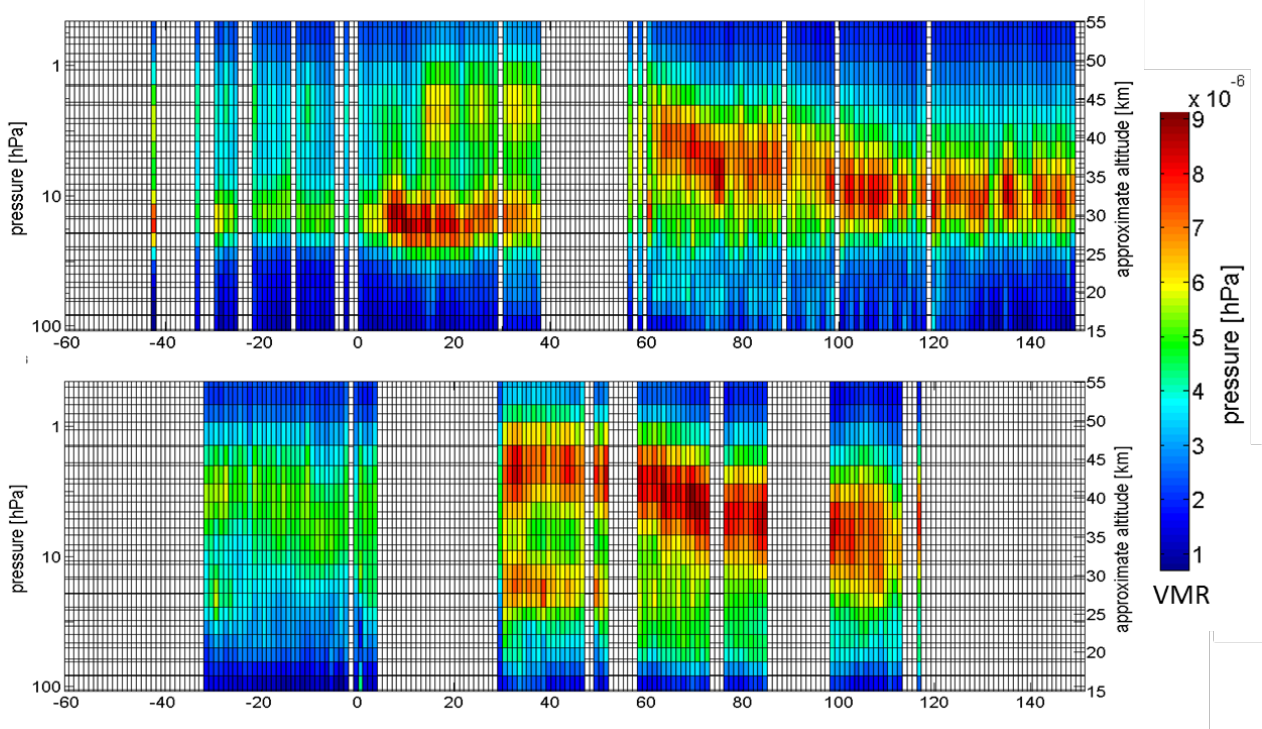


**Figure 6.18** Time series of the daily average  $O_3$  profiles for KIMRA (top), MIRA 2 (bottom) measurements. Pressure is plotted on a log scale on the Y-axis.

### 6.5.2 January to March, 5-year $O_3$ time series

$O_3$  profiles have been retrieved from KIMRA measurements for January, February, and March, beginning in 2008. Data were not available from 2012. Daily averages were made and the resulting time series for each year are shown in Figure 6.19. January predominantly shows the lowest  $O_3$  concentrations, except for in one region at around 10 hPa (32 km) (particularly for 2009 and 2013) which has a sharp maximum. The most interesting feature is the aforementioned dip in the profile. The  $O_3$  dip is present for some period of time in each year and disappears in late February or March. It is persistent right up until the end of March in 2009. It is a possible indication of chemical ozone depletion, although one would expect the depletion to be most pronounced at a lower altitude than that of the  $O_3$  dip. The disappearance of the feature in February/March may have something do with the breaking up of the polar vortex. Also, the two peaks in the profile, because of the  $O_3$  dip, appear to merge together in 2010 and 2011. A strong  $O_3$  dip (most similar to 2010 presented here) has been observed previously with KIMRA in the winter of 2002/2003 [Raffalski et al., 2005], and coincided with ozone mini-holes be-

## 6. Ground-based observations of ozone above Kiruna

---

tween the 4<sup>th</sup> and 11<sup>th</sup> December 2002, as reported by the European Ozone Research Coordinating Unit (EORCU) [EORCU, 2013]. This mini-hole was attributed mainly to dynamical effects: a raise in the tropopause height, coinciding with a strong vortex and ascending motion at higher altitudes. The persistence of the feature above Kiruna is not consistent with an ozone mini-hole as these features typically last about a week before local recovery of the ozone [Peters et al., 1995]. The KIMRA measurements for winter 2002/2003 [Raffalski, 2003] still show the structure of the O<sub>3</sub> dip throughout most of December, with a reduced magnitude compared to the instance of the ozone-mini holes. A possible explanation, since the occurrence in Figure 6.18 seems to be most pronounced in January when Kiruna lies within and around the vortex edge (Figure 6.17), is that the vertical shape of the vortex is such that the beam from KIMRA follows a path that encounters an atmospheric layer of extra-vortex air in between two layers of vortex air. The polar vortex has been shown to have variation in its latitudinal extent with altitude [Harvey et al., 2002] but the altitudes at which this possible feature occurs would have to remain stable for long periods to account for the observations.

## 6. Ground-based observations of ozone above Kiruna

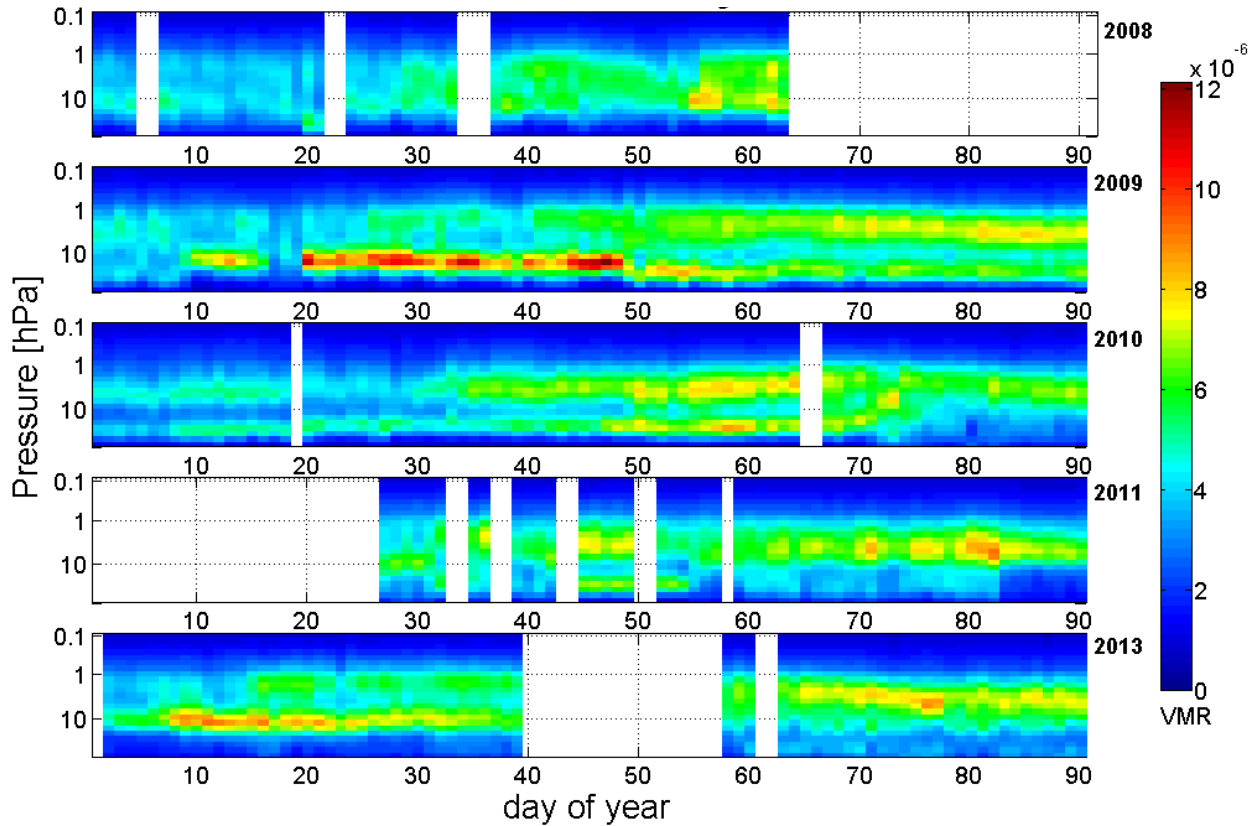


**Figure 6.19** Retrieved  $O_3$  concentrations above Kiruna from KIMRA, for January to March for the years 2008, 2009, 2010, 2011, and 2013. Pressure is plotted on a log scale on the Y-axis.

The monthly mean  $O_3$  profile for each year is shown in Figure 6.20, as well as the overall monthly mean and standard deviation. For each month,  $O_3$  shows the most variability in the lower stratosphere, between approximately 10 and 30 hPa. Some of the variation may be due to the fact that KIMRA switches its observation direction between north and south, but the daily averaging of the profiles should remove much of it. Additionally, as discussed in Section 6.3.2, the standing wave signals in the  $O_3$  spectra will cause systematic biases that vary as a function of atmospheric opacity, and add to the natural variance in the profile. This standing wave signal has been attributed to the higher variance found in the comparison of KIMRA lower stratospheric partial columns (see Section 6.4.4), with respect to the same comparisons with MIRA 2. The peak in  $O_3$  at about 3 - 4 hPa ( $\sim 35\text{-}40$  km) (can be seen in the a priori) is, on average, lowest in January and increases through March. The lower altitude peak at about 20 hPa ( $\sim 25$  km) decreases in March relative to January and February. This change in the altitude of

## 6. Ground-based observations of ozone above Kiruna

---

the global maximum of O<sub>3</sub> can be expected if the polar vortex weakens and breaks up toward the end of winter and as the Sun moves to higher elevation angles.

In the left panel of Figure 6.20, for January and February, every year shows an O<sub>3</sub> dip to some degree (most pronounced in 2010 and least in 2008), and at varying altitudes. These features tend to decrease in magnitude in March, except for 2009, which maintains an O<sub>3</sub> dip greater than 1 ppm. While it is emphasised here that this feature is not a result of the described biases in KIMRA O<sub>3</sub>, it will be difficult to quantitatively separate the two.

## 6. Ground-based observations of ozone above Kiruna

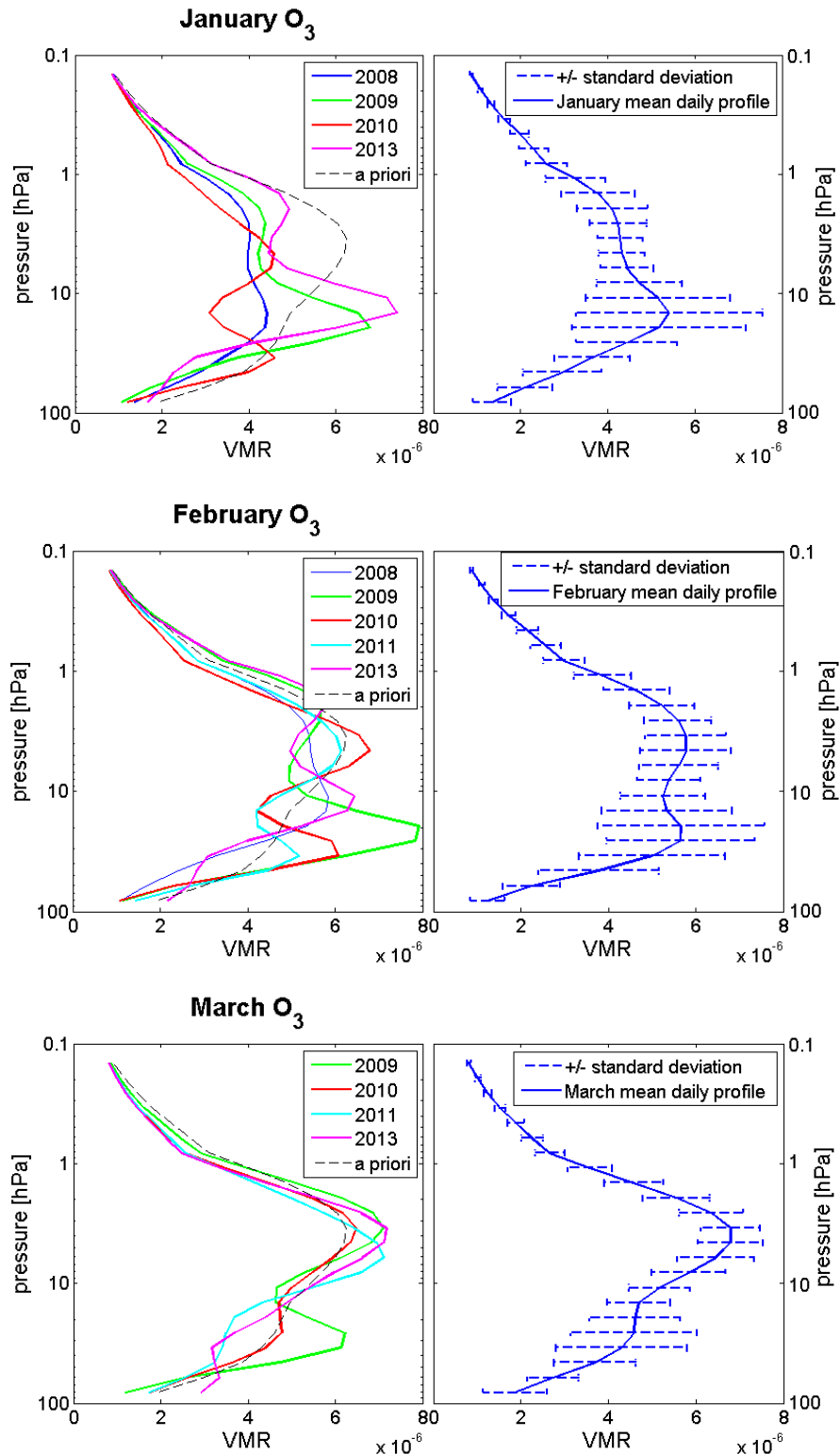


**Figure 6.20** Left: monthly averages of daily Kiruna O<sub>3</sub> profiles from KIMRA measurements for January, February, and March by year. A missing year means that there were not enough measurements during the month to produce a representative average. Right: mean and standard deviations of the monthly profiles.

### 6.1 Conclusion

The aim of this work was to develop an inversion scheme for the KIMRA and MIRA 2 instruments at IRF, Kiruna, and to characterize the retrieved O<sub>3</sub> profiles, through comparison with each other and with O<sub>3</sub> profiles from other instruments. KIMRA and MIRA 2 O<sub>3</sub> profiles ranging from November 2012 to May 2013 were used in the comparison. The retrieval altitude range for the O<sub>3</sub> profiles is approximately 16 – 54 km, with a resolution of at best 8 km, derived from the FWHM of the averaging kernels. KIMRA and MIRA 2 profiles show generally good agreement with each other. The mean of the difference in their profiles (bias) lies within the range of the measurement errors except for 18–24 km. An oscillatory bias was identified in the KIMRA data, present in the comparison with all three other instruments. There is a low bias of ~ 1 ppm at 22 km, and a high bias of ~ 1 ppm at 28 km, both with a halfwidth of ~ 5 km. MIRA 2 shows a similar oscillatory bias, but with smaller amplitude (< 0.5 ppm) and finer altitude structure that covers the whole retrieval altitude range. As the oscillatory biases with respect to other instruments were calculated using many profiles, they are not expected to be due to oscillations coming from random noise on the spectra. Instead, the relatively stable oscillatory structures present in the profiles are assumed to be caused by standing wave signals that are clearly present in the spectra. Both KIMRA and MIRA 2 otherwise show generally good agreement with MLS O<sub>3</sub> profiles, and both show a general low bias with respect to the ozonesondes. MIRA 2 shows overall better agreement with MLS and the ozonesondes, compared to KIMRA.

Retrieved KIMRA O<sub>3</sub> profiles from January to March, 2008, 2009, 2010, 2011, and 2013, were used to assess the local day-to-day variability of O<sub>3</sub> above Kiruna. A time series for each year was presented and averages and standard deviation of the daily O<sub>3</sub> were calculated for each month. The lower stratosphere between approximately 30 and 10 hPa (~20 – 33 km) shows the most variability, but some of this can be attributed to the fact that the oscillatory bias in the profiles due to standing wave features will vary with the opacity of the atmosphere. The lowest O<sub>3</sub> concentrations here are found in January, and tend to increase through March. The location of the maximum in the O<sub>3</sub> profile shifts from ~15 hPa in January to ~3 hPa (the location of the maximum in the a priori profile) in March. The most interesting feature that the results show is a local minimum in the O<sub>3</sub> profile. The feature is present in all years and is persistent for time

## 6. Ground-based observations of ozone above Kiruna

---

scales as long as two months, at least. The feature may be difficult to quantitatively assess because it tends to partially overlap in altitude with the oscillatory bias in the KIMRA data. Previous measurements with KIMRA during winter 2002/2003 showed a similar local minimum in the O<sub>3</sub> profile throughout most of December 2002. Very low O<sub>3</sub> values in early December 2002 coincided with ozone mini-holes but these features lasted only a few days, while the O<sub>3</sub> dip appears persistent over monthly timescales. Because Kiruna generally lies close to the location of the edge of the polar vortex, a consistent variation in altitude of the latitudinal extent of the vortex may explain the O<sub>3</sub> local minimum. The sPV data from 2013 shows consistency with this idea, but an analysis over more years of observation is needed.

# Chapter 7

---

## 7 Summary and outlook

### 7.1 Summary

**A new ground-based millimeter-wave instrument was designed for Arctic atmospheric research.** The instrument, SPÉIR, is designed to measure ozone related trace gases in the Arctic stratosphere and will be the first instrument in the Canadian Arctic capable of making continuous measurements of ClO. SPÉIR will measure emission from rotational transitions of O<sub>3</sub>, N<sub>2</sub>O, HNO<sub>3</sub>, and ClO in the atmosphere, and will be housed at the Polar Environment Atmospheric Research Laboratory in Eureka, Nunavut, Canada. It was designed for optimal operation in the frequency range 265 – 280 GHz. SPÉIR was designed with a highly sensitive Superconductor-Insulator-Superconductor mixer to enable measurements of the weak spectral line of ClO on a timescale of hours. Stronger signals (e.g., from O<sub>3</sub>) can be measured on shorter timescales. The quasioptical setup results in a high-gain system that provides good horizontal resolution in the atmosphere and minimal deformation of the atmospheric signal. An In-phase Quadrature Correlator spectrometer is combined with a sideband-separating mixer to improve the sideband separation, and can be made autonomous. Ultra-Gaussian horns, high emissivity conical-shaped blackbody calibration loads, a path length modulator, and angled windows on the cryostat are used in an effort to minimize potential standing wave signatures that can obscure the atmospheric ClO signal. The instrument is currently in post-design phase.

**A characterization and simulation of SPÉIR was performed, with results that are applicable in general to remote sounding in the 265 – 280 GHz region.** The SPÉIR observation system includes the instrument, the Atmospheric Radiative Transfer Simulator, and the inversion tool, Qpack. Altitude ranges over which retrievals of concentrations can be made, and the altitude resolution of the retrieved profiles over those ranges, were found using an Optimal Estimation Method. The ranges varied over the stratosphere, the largest and smallest being for O<sub>3</sub>

and HNO<sub>3</sub>, respectively. The predicted altitude resolution of these retrievals ranged between 5 and 15 km depending on the species and height. Error analysis with the OEM showed that uncertainties in model and instrument parameters contributed to statistical error between approximately 5% and 10% for the retrieval of O<sub>3</sub>, 5% and 15% for N<sub>2</sub>O, and 10% and 20% for ClO and HNO<sub>3</sub>. The results from OEM compared well to repeated simulation of the observation system. Nonlinearities in the forward model were identified as causing biases in the average difference between retrieved and true atmospheric states. The varying weighting functions for different inversions can give rise to errors in a climatology or trend analysis, made using profiles retrieved from spectra in the 265 - 280 GHz region, on the order of 5 - 10 %.

**An assessment was made of the impact that the uncertainties in spectroscopic parameters have on remote sounding in the 265 – 280 GHz region.** The study was made specifically for SPÉIR but the results apply to any ground-based remote sounder using the available spectroscopic parameters in this frequency range. The errors on the retrieval of the target species, due to uncertainties in position, intensity, air broadening and pressure shift parameters of individual spectral lines from all species, were investigated. The parameters contributing to the largest errors were identified and recommendations were made for new lab measurements which would be most beneficial to ground-based remote sounding. The errors due to uncertainties in spectroscopic parameters varied between species and altitude and were often larger than the statistical error determined in the previous study.

**A new atmospheric O<sub>3</sub> dataset was created using measurements from two ground-based millimeter wave instruments, KIMRA and MIRA 2, housed at the Institute for Space Physics (IRF), Kiruna, Sweden.** The retrieval altitude range for the O<sub>3</sub> profiles is approximately 16 – 54 km, with a resolution of at best 8 km. The profiles from November 2012 to May 2013 were compared with each other, to the Aura Microwave Limb Sounder (MLS), and to ozonesondes launched from Sodankylä, Finland, in an effort to characterize the retrieved information. Both instruments showed a general low bias with respect to the ozonesondes, and the agreement with MLS was good, but it is clear from both comparisons that there are oscillatory biases present with KIMRA and MIRA 2. MIRA 2 shows generally better agreement than KIMRA in both cases, but this is considered to be mainly due to the oscillatory bias present in the lower stratosphere for KIMRA. The biases in the profiles are thought to be due to the stand-

ing wave signals present in the measured spectra, whose impact will vary with the atmospheric opacity.

Winter-time series for O<sub>3</sub> above Kiruna were created using KIMRA data from 2008 to 2013. The most interesting feature identified using this data, is a mid-stratospheric local minimum in the O<sub>3</sub> profile. This O<sub>3</sub> dip (as it has been referred to here) is seen to be persistent for up to at least 3 months (seen for 2009 data). Quantitatively investigating the O<sub>3</sub> dip may be problematic as it can overlap in altitude with the identified oscillatory bias in the KIMRA O<sub>3</sub> profile.

## 7.2 Outlook

The future continuation and expansion of the research presented here is most easily considered in two parts: The work in Chapters 3, 4, and 5, relating to SPÉIR, and the work in Chapter 6, relating to O<sub>3</sub> measurements in Kiruna.

The next step with SPÉIR is, of course, to build, test, and install it at Eureka. An extension of the size of the 4 K stage in the cryostat is a recommended change to the current design. This change will not directly affect the operation of the SPÉIR but will make the construction, maintenance, and troubleshooting much easier as the 4 K chamber is somewhat crowded as is. The extension should ideally provide a simple (circular etc.) 4 K stage that encompasses the two horns. Particular care should be taken in the construction of the cold calibration system to ensure that no oxygen is being condensed into the conical blackbody target. Changes to the design must be carefully made, as the components and their sources were chosen considering the scientific goals discussed in this thesis. A preference for operation of SPÉIR would be to be able to fully exploit the sideband separation available from the SIS mixer. If, for example, future advancements in IQ-correlator spectrometers allow phase errors to be corrected for both sidebands at a time, then it would be possible to measure more than one target species at a time.

A study on the effect of varying the a priori for ClO would be beneficial for case studies based on winter-time chlorine activation and ozone depletion. Tests could be done that assess the impact of using a non-Gaussian, double peaked, probability density function, although implementing a change in the a priori profile over winter-time compared to other seasons may not be desirable if one is interested in a year-long time series. Because the data from SPÉIR will be

used for analyses of monthly/yearly averages and time series etc., it would be beneficial to somehow account for the nonlinearities in the forward model that give rise to varying weighting functions. New measurements of spectroscopic parameters would have a large impact on the accuracy of retrievals in the 265-280 GHz range, particularly for retrievals of ClO and HNO<sub>3</sub>. The impact would also have a wide reach since this frequency range is used by other ground-based instruments.

There are many possible routes to take with regards to using the data from KIMRA and MIRA 2. Firstly, all of the KIMRA measurements since its installation can be inverted using the inversion scheme that was set up here (possibly with some minor alterations for any changes to operation). It has been tried previously, but to no avail, to find the source of the standing wave feature in the KIMRA spectra [personal communication with Uwe Raffalski, May 2013]. The standing wave features in the MIRA 2 data appeared recently after the installation of the instrument in November 2012. Eliminating the standing wave feature from the spectra would improve the accuracy of the retrieved O<sub>3</sub> profiles and possibly remove the oscillatory biases, but it appears to be quite difficult to find and eliminate the source of the standing waves, in KIMRA at least. Nonetheless, the utility of the newly retrieved datasets has been shown and they are available for scientific studies.

With regards to comparison, the KIMRA dataset should be used to compare with all available satellite datasets. With the very likely upcoming gap in profiling satellite instruments, calibration with respect to ground-based instruments is needed in order to combine datasets from current and new satellites. KIMRA presents an excellent tool to achieve this as it has almost continuous measurements at Kiruna from 2002 onwards. It should be investigated whether nonlinearities in the forward modelling around 230 GHz can affect the use of these O<sub>3</sub> profiles for trend studies. The presence of the O<sub>3</sub> dip above Kiruna is quite interesting and warrants further investigation to determine its origin. The KIMRA measurements can be used to determine whether the feature was present in other winters (as it was in 2002/2003), or at other times of the year. Determination of the cause of the O<sub>3</sub> dip will most likely require the use and/or reference of a chemical transport model to find the underlying processes. The KIMRA and MIRA 2 profiles were used here to investigate the daily variability in O<sub>3</sub>, but as the instru-

ments make O<sub>3</sub> measurements as often as every 15 minutes during the winter, the spectra can also be used to investigate variability on shorter time scales.

## Bibliography

Anderson GP, Clough SA, Kneizys FX, Chetwynd JH, Shettle EP. AFGL atmospheric constituent profiles (0–120 km), Tech. Rep. TR-86-0110, AFGL, 1986.

Andrews DG. An Introduction to Atmospheric Physics. Cambridge University Press; 2005.

Batchelor RL, Strong K, Lindenmaier R. A New Bruker IFS 125HR FTIR Spectrometer for the Polar Environment Atmospheric Research Laboratory at Eureka, Nunavut, Canada: Measurements and Comparison with the Existing Bomem DA8 Spectrometer. *J Atmos Ocean Tech.* 2009;26:1328-40.

Berg H, Krupa R, Hochschild G, Kopp G, Kuntz M. Millimeter wave radiometer with adjustable internal calibration load for high resolution measurements of stratospheric constituents. Proceedings of 2nd ESA Workshop on Millimetre Wave Technology and Applications: Antennas, Circuits and Systems; May 1998; Espoo: 1998. pp. 372-77.

Bernath PF. Spectra of Atoms and Molecules, 2<sup>nd</sup> Edition. Oxford University Press; 2005.

Bodeker GE, Scott JC, Kreher K, McKenzie RL. Global ozone trends in potential vorticity coordinates using TOMS and GOME intercompared against the Dobson network: 1978–1998, *J Geophys Res*, 2001;106(23):29-42.

Buehler SA, Eriksson P, Lemke O. Absorption lookup tables in the radiative transfer model ARTS. *JQSRT*. 2011;112:1559-67.

Buehler SA, Eriksson P, Kuhn T, von Engeln A, Verdes C. ARTS, the Atmospheric Radiative Transfer Simulator. *JQSRT*. 2005;91(1):65-93.

Böhler SA (Institute of Remote Sensing, University of Bremen, Germany). The Impact of Continuum Emissions in the mm and Sub-mm Spectral Range. Final Report. European Space Research and Technology Centre (ESTEC); 2002 Jun 13. Contract No.: 10998/94/NL/CN.

Buehler SA. Microwave limb sounding of the stratosphere and upper troposphere [PhD thesis]. University of Bremen; 1999.

Bauer A, Birk M, Wagner G, Colmont J-M, Priem D, Wlodarczak G, et al. Study on a spectroscopic database for millimeter and submillimeter wavelength. Final report. ESA; 2000. Report No: 11581/95/NL/CN.

Clarricoats PJB, Oliver AD. Corrugated horns for microwave antennas. IEEE electromagnetic waves series 18; Peter Peregrinus Ltd; 1983.

Cruckshank PAS, Bolton DR, Robertson DA, Wyld RJ, Smith GM. Reducing Standing waves in Quasi-Optical Systems by Optimal Feedhorn Design. Proceedings of the 15th International Conference on Terahertz Electronics, IRMMW Joint 32nd International Conference, June 2-9, 2007; pp. 941-942; Cardiff 2007.

Crutzen PJ. The influence of nitrogen oxides on the atmospheric ozone content. Quart J R Met Soc. 1970;96:320-5.

Demaison J, Buehler S, Cazzoli G, Flaud J-M, Bakri B, et al. Characterisation of Millimetre-Wave Spectroscopic Signatures. Final report. ESTEC; 2004 Mar. Report No: 16377/02/NL/FF.

de Zafra RL, Jaramillo M, Parrish A, Solomon P, Connor B, Barrett J. High concentrations of chlorine monoxide at low altitudes in the Antarctic spring stratosphere: Diurnal variation. Nature. 1987;328:408-11.

Ediss GA, Carter M, Cheng J, Effland JE, Grammer W, Horner N Jr., Kerr AR, et al., ALMA Band 6 Prototype Cartridge: Design and Performance. ALMA Memo 502. 21 June 2004. Available from <http://www.alma.nrao.edu/memos/>.

EORCU, <http://www.ozone-sec.ch.cam.ac.uk/EORCU/Reports/wr0203.pdf>, European Ozone Research Coordinating Unit, 14 Union Road, Cambridge, CB2 1HE, UK, 2003.

Eriksson P, Buehler SA, Davis CP, Emde C., Lemke O. ARTS, the atmospheric radiative transfer simulator, Version 2. JQSRT. 2011;112:1551-58.

Eriksson P, Jimenez C, Buehler SA. Qpack, a general tool for instrument simulation and retrieval work. JQSRT. 2005;91(1):47-64.

Eriksson P, Merino F, Murtagh D, Baron P, Ricaud P, de la Nöe J. Studies for the Odin sub-millimetre radiometer: I. Radiative transfer and instrument simulation. *Can J Phys.* 2002;80:321-40.

Eriksson P. *Microwave Radiometric Observations of the Middle Atmosphere: Simulations and Inversions* [PhD thesis]. Chalmers University of Technology: 1999.

Eriksson P, Jiménez C. Non-linear profile retrievals for observations in the lower stratosphere with the Odin sub-mm radiometer. *Proceedings of 1998 IEEE International Geoscience and Remote Sensing Symposium*; 1998 Jul 6-10; Seattle, USA. 1998. p. 1420-3.

Flentje HA, Doernbrack A, Fix A, Meister A, Schmid H, Fueglistaler S, Luo B, et al. Denitrification inside the stratospheric vortex in the winter of 1999-2000 by sedimentation of large nitric acid trihydrate particles. *J Geophys Res.* 2002;107(D16):4314.

Fogal PF, LeBlanc LM, Drummond JR. The Polar Environment Research Laboratory (PEARL): Sounding the Atmosphere at 80° North. *Arctic.* 2013;66(3):377-86.

Froidevaux L, Jiang YB, Lambert A, Livesey NJ, Read NG, Waters JW, Browell EV et al., Validation of Aura Microwave Limb Sounder stratospheric ozone measurements. *J Geophys Res.* 2008;113:D15S11.

Golchert SHW, Buschmann N, Kleindienst A, Palm M, Schneider N, Jønch-Sørensen H, et al., Starting long-term stratospheric observations with RAMAS at Summit, Greenland. *IEEE Trans Geosci Remote Sens.* 2005;43(5):1022-27.

Goldsmith PF. *Quasioptical Systems, Gaussian Beam Quasioptical Propagation and Applications*. New York: IEEE; 1998.

Han Y, Westwater ER. Analysis and improvement of tipping calibration for ground-based microwave radiometers. *IEEE Trans Geosci Remote Sens.* 2000;38(3):1260-76.

Hansen PC. Numerical tools for analysis and solution of Fredholm integral equations of the first kind. *Inverse Probl.* 1992;8(6):849-72.

Harald ER, Polvani LM. Are recent ozone losses caused by increasing greenhouse gases? *Geophys Res Lett.* 2013;40(16):4437-41.

Harvey LV, Pierce BR, Fairlie DT, Hitchman MH. A climatology of stratospheric polar vortices and anticyclones. *J Geophys Res.* 2002;107:D20.

IGOS 2004. Report of the Integrated Global Atmospheric Chemistry Observation Theme Team. September 2004.

IPCC 2013. Climate Change 2013: Working group contribution to the Fifth Assessment Report of the Intergovernmental Panel on Climate Change. 2013.

Jacob DJ. Introduction to Atmospheric Chemistry. Princeton University Press; 1999

Janssen MA. An Introduction to the Passive Microwave Remote Sensing of Atmospheres. In: Janssen, editor. Atmospheric remote sensing by microwave radiometry. New York: Wiley; 1993. p. 1-33.

Jiang YB, Froidevaux L, Lambert A, Livesey NJ, Read WG, Waters JW, Bojkov B, et al. Validation of the Aura Microwave Limb Sounder Ozone by Ozonesonde and Lidar Measurements. *J Geophys Res.* 2007;112:D24S34.

Kerr AR, Pan SK, Lauria EF, Lichtenberger AW, Zhang J, Pospieszalski MW, Horner N, et al. The ALMA Band 6 (211-275 GHz) Sideband-Separating SIS Mixer-Preamplifier. ALMA Memo 498. 14 May, 2004. Available from <http://www.alma.nrao.edu/memos/>

Kivi R, Kyrö E, Turunen T, Harris NRP, von der Gathen P, Rex M, Anderson SB, Wohltmann I. Ozonesonde observations in the Arctic during 1989—2003: Ozone variability and trends in the lower stratosphere and free troposphere. *J Geophys Res.* 2007;112:D08306.

Kopp G, Belova A, Diez y Riega V E, Gross J, Hochschild G, Hoffmann P, Murtagh D et al.. Inter-comparison of Odin-SMR ozone profiles with ground-based observations in the Arctic, the mid-latitudes, and the tropics. *Can J Phys.* 2007;85:1097-110.

Kopp G, Berg H, Blumenstock T, Fischer H, Hase F, Hochschild G, Hoepfner M, et al.. Evolution of ozone and ozone-related species over Kiruna during the SOLVE/THESEO 2000 campaign retrieved from ground-based millimeter-wave and infrared observations. *J Geophys Res.* 2003;108:51(1)-51(12).

Kopp G. (Karlsruhe Institute of Technology, Karlsruhe, Germany). Inversion arktischer stratosphärischer Spurengasprofile für die Ozonforschung aus Messungen eines bodengebundenen Millimeterwellenradiometers. Final Report; Forschungszentrum Karlsruhe; 2002. Report No.: 6563.

Kopp G. The Karlsruhe Millimeterwave Forward Model, Proceedings of the second International Workshop on Millimeter and Sub-Millimeter Wave Radiative Transfer Modeling, Osterholz-Scharmbeck, Germany, June 19–22, 2000; Logos Verlag Berlin: 2001.Kraus JD. *Antennas*, 2<sup>nd</sup> Edition. New York: Wiley; 1988.

Krauss JD. *Radio Astronomy*, 2<sup>nd</sup> Edition. Cygnus-Quasar Books; 1986.

Krupa R, Hochschild G, Fischer H, Wiesbeck W. Balanced Calibration Technique with an Internal Reference Load for Ground Based Millimeter Wave Radiometry, 1998 IEEE International Geoscience and Remote Sensing Symposium Proceedings; Vol. I; pp. 387–389; Seattle, July 1998.

Kuhn T. Atmospheric absorption models for the millimeter wave range [PhD thesis]. University of Bremen; 2003.

Liebe HJ, Hufford GA, Cotton MG. Propagation modeling of moist air and suspended water/ice particles at frequencies below 1000 GHz. AGARD 52nd Specialists' Meeting of the Electromagnetic Wave Propagation Panel; 1993 May 17-21; Palma De Mallorca, Spain: 1993.

Lindenmaier R. Studies of Arctic middle atmosphere chemistry using infrared absorption spectroscopy [PhD thesis]. University of Toronto: 2012.

Livesey NJ, Read WG, Froidevaux L, Lambert A, Manney GL, Pumphrey HC, Santee ML, et al. Version 3.3 and 3.4 Level 2 data quality and description document. JPL California Institute of Technology; May 14: 2013.

Livesey NJ, Filipiak MJ, Froidevaux L, Read WG, Lambert A, Santee ML, Jiang JH, et al., Validation of Aura Microwave Limb Sounder O<sub>3</sub> and CO observations in the upper troposphere and lower stratosphere. *J Geophys Res.* 2008;113:D15S02.

Luers JK. Temperature Error of the Vaisala RS90 Radiosonde. *J Atmos Ocean Tech.* 1997;14:1520-32.

Manney GL, Santee ML, Rex M, Livesey NJ, Pitts MC, Veefkind P, et al. Unprecedented Arctic ozone loss in 2011. *Nature.* 2011;478:469-75.

Manney GL, Daffer WH, Zawodny JM, Bernath PF, Hoppel KW, Walker KA, Knosp W, et al., Solar occultation satellite data and derived meteorological products: Sampling issues and comparisons with Aura Microwave Limb Sounder. *J Geophys Res.* 2007;112:D24.

Marquardt D. An Algorithm for Least Squares Estimation on Nonlinear Parameters. *J Soc Indust Appl Math.* 1963;11:431-41.

May RD, Webster CR. Measurements of Line Positions, Intensities, and Collisional Air-Broadening Coefficients in the HN<sub>0</sub><sub>3</sub> 75-μm Band Using a Computer-Controlled Tunable Diode Laser Spectrometer. *J Mol Spectrosc* 1989;138:383-97.

McConnell JC and Jin JJ. Stratospheric Ozone Chemistry. *Atmos Ocean.* 2008;46(1):69-92.

Minoli D. Satellite Systems Engineering in an IPv6 Environment. CRC Press. USA: 2009.

Murk A, Treuttel J, Rea S, Matheson D. Characterization of a 340 GHz Sub-Harmonic IQ Mixer with Digital Sideband Separating Backend. 5<sup>th</sup> ESA Workshop on Millimeter Wave Technology and Applications & 31<sup>st</sup> ESA Antenna Workshop, 18-20 May 2009. ESTEC, Noordwijk; 2009.

Murk A, Duric A, and Patt F. Characterization of ALMA calibration targets. 19th International Symposium on Space Terahertz Technology; 2008 Apr 28-30; Groningen, Netherlands. 2008.p. 530-33.

Murphy JA. Distortion of a simple Gaussian beam on reflection from off-axis ellipsoidal mirrors. *Int J Infrared Millimeter Waves.* 1987;8:1165-87.

Oh JJ, Cohen EA. Pressure broadening of ClO by N<sub>2</sub> and O<sub>2</sub> near 204 and 649 GHz and new frequency measurements between 632 and 725 GHz. JQSRT 1994;52(2):151-6.

Parrish A. Millimeter-wave remote sensing of ozone and trace constituents in the stratosphere. Proc IEEE. 1994;82(12):1915-29.

Parrish A, De Zafra RL, Solomon PM, Barrett JW. A ground-based technique for millimeter wave spectroscopic observations of stratospheric trace constituents. Radio Sci. 1988;23(8):106-18.

Peter T. Microphysics and heterogeneous chemistry of polar stratospheric clouds. Ann Rev Phys Chem. 1997;48:785-22.

Pickett HM, Poynter RL, Cohen EA. Submillimeter, Millimeter, and Microwave Spectral Line Catalog. Tech rep. California Institute of Technology Jet Propulsion Laboratory, Pasadena; California: 2001.

Raffalski U, Berg H, Hochschild G, Kopp G. Continuous ozone measurements over Kiruna during winter/spring 2002: A new millimeter wave radiometer operated at the Swedish Institute of Space Physics, Kiruna, Sweden, Proceedings of the Sixth European Symposium on Stratospheric Ozone Research, Gothenberg, pp. 369–372, 2002.

Raffalski U, Hochschild G, Kopp G, Urban J. Evolution of stratospheric ozone during winter 2002/2003 as observed by a ground-based millimetre wave radiometer at Kiruna, Sweden. Atmos Chem Phys. 2005;5:1399-1407.

Randal WJ, Wu JF, Stolarski R. Changes in column ozone correlated with stratospheric EP flux. J Meteorol Soc Jpn. 2002;80:849-62.

Ravishankara AR, Daniel JS, Portmann RW. Nitrous Oxide (N<sub>2</sub>O): The dominant ozone-depleting substance emitted in the 21st century. Science. 2009;326(5949):123-5.

Rex M, Salawitch RJ, von der Gothen P, Harris NRP, Chipperfield MP, Naujokat B. Arctic ozone loss and climate change. Geophys Res Lett. 2004;31(4).

Rex M, Salawitch RJ, Harris NRP, von der Gothen P, Braathen GO, Schulz A, Deckelmann H, et al. Chemical depletion of Arctic ozone in winter 1999/2000. *J Geophys Res.* 2002;107:D20.

Rodgers CD. Inverse methods for atmospheric remote sounding: Theory and practice. Vol 2. Series on atmospheric and ocean physics. Singapore: World Scientific; 2000.

Rodgers CD. Characterization and error analysis of profiles retrieved from remote sounding measurements. *J Geophys Res.* 1990;95(D5):5587-95.

Rosenkranz PW. Absorption of microwaves by atmospheric gases. In: Janssen, editor. Atmospheric remote sensing by microwave radiometry. New York: Wiley; 1993. p. 37-90.

Rothman LS, Gordon IE, Barbe A, Chris Benner D, Bernath PF, Birk M, et al. The HITRAN 2008 molecular spectroscopic database. *JQSRT.* 2009;110(9-10):533-72.

Salby M, Titova E, and Deschamps Lilia. Rebound of Antarctic ozone. *Geophys Res Lett.* 2011;38(9).

Solomon S. Stratospheric ozone depletion: A review of concepts and history. *Rev Geophys.* 1999;37(3):275-316.

Solomon PM, Connor B, de Zafra RL, Parrish A, Barrett J, M. Jaramillo. High concentrations of chlorine monoxide at low altitudes in the Antarctic spring stratosphere: Secular variation. *Nature.* 1987;328:411-3.

Solomon PM, de Zafra R, Parrish A, Barrett JW. Diurnal Variation of Stratospheric Chlorine Monoxide: A critical test of chlorine chemistry in the ozone layer. *Science.* 1984;224(4654):1210-1214.

Straub C, Murk A, Kämpfer N. MIAWARA-C, a new ground based water vapour radiometer for measurement campaigns. *Atmos. Meas. Tech.* 2010;3:1271-85.

Tarantola A, Valette B. Generalized nonlinear inverse problems solved using the least squares criterion. *Rev Geophys Space Phys.* 1982;20(2):219-32.

Verdes CL, Buehler SA, Perrin A, Flaud J-M, Demaison J, Wlodarczak G, et al. A sensitivity study on spectroscopic parameter accuracies for a mm/sub-mm limb sounder instrument. *J Mol Spectrosc* 2005;229:266-275.

Wagner G, Birk M, Schreier F, Flaud J-M. Spectroscopic database for ozone in the fundamental spectral regions. *J Geophys Res* 2002;107(D22):4626.

Wengler MJ. Submillimeter-wave detection with superconducting tunnel diodes. *Proc IEEE*. 1992;80(11):1810-26.

WMO (World Meteorological Organization). Scientific assessment of ozone depletion: 2010, Global Ozone Research and Monitoring Project-Report No. 52. Geneva, Switzerland: 2011.

WMO (World Meteorological Organization). Scientific assessment of ozone depletion: 2002, Global Ozone Research and Monitoring Project-Report No. 47. Geneva, Switzerland: 2003.

York D, Evensen NM, Martinez ML, Delgado JDB. Unified equations for the slope, intercept, and standard errors of the best straight line. *Am J Phys* 2004;72(3):367-375.